Supplementary Information

for

Extension of Nature's NIR-I Chromophore into the NIR-II Region

Kittipan Siwawannapong,[a] James R. Diers,[b] Nikki Cecil M. Magdaong,[c] Phattananawee Nalaoh,[d]

Christine Kirmaier,[c] Jonathan S. Lindsey,*[a] Dewey Holten,*[c] and David F. Bocian*[b]

[a] Department of Chemistry, North Carolina State University, Raleigh, NC, 27695-8204, USA

E-mail: jlindsey@ncsu.edu

[b] Department of Chemistry, University of California, Riverside, CA, 92521-0403, USA

E-mail: david.bocian@ucr.edu

[c] Department of Chemistry, Washington University, St. Louis, MO, 63130-4889, USA

E-mail: holten@wustl.edu

[d] Department of Chemistry, University of Tennessee, Knoxville, TN 37996, USA

Table of Contents

Section S1

Exploratory Synthesis

The Eastern-Western route was pursued as an alternative method rather than the Northern-Southern route,[22] which was previously employed to access bacteriochlorin **II**. With this strategy, dibromobacteriochlorin **II** could be obtained beginning with Michael acceptor **VII** and bromopyrrole **S2** (Scheme S1A). Access to the latter started from commercially available pyrrole **S2**, employing a series of five reactions,[29] encompassing (1) TIPS protection, (2) β-bromination, (3) CAN oxidation of the α-methylpyrrole, (4) Henry reaction, and (5) reduction (Scheme S2B, route 1).
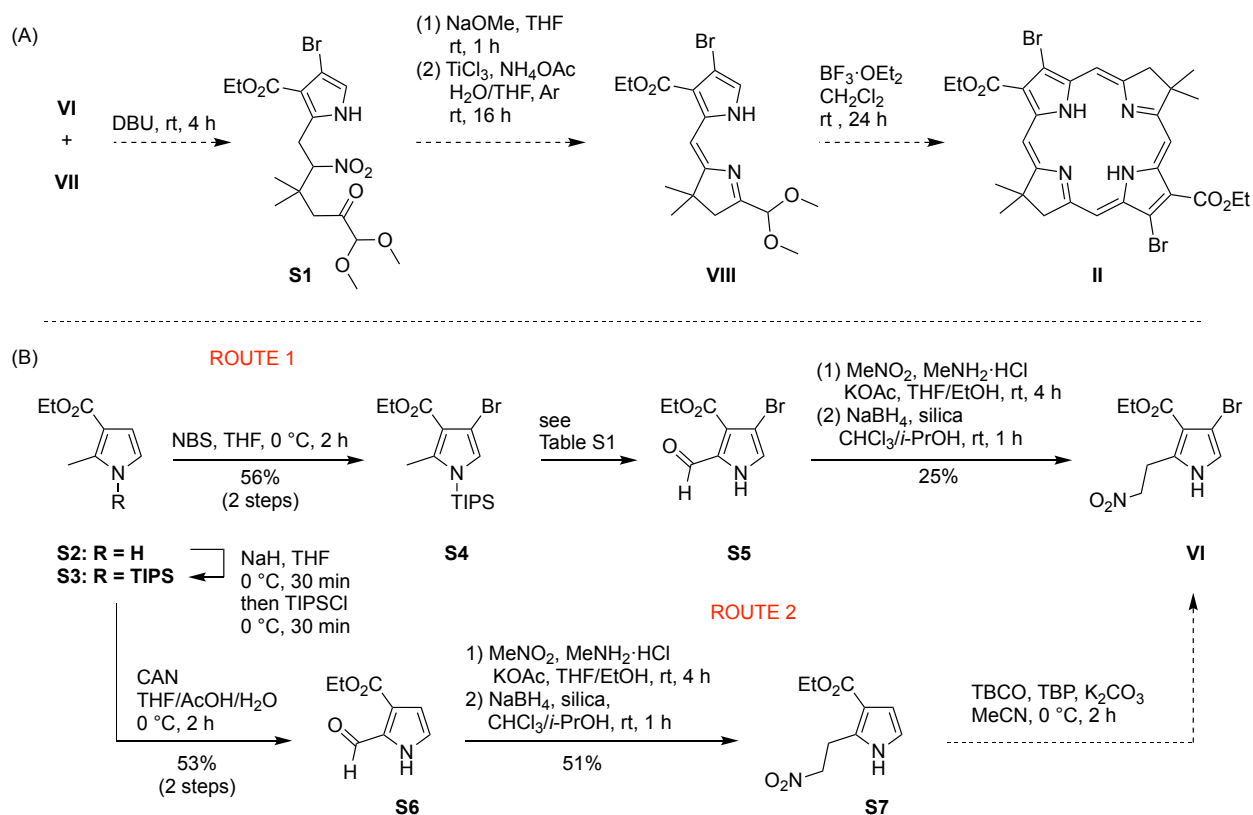
Scheme S1. (A) Planned synthesis of dibromobacteriochlorin (**II**) via Eastern-Western route (B) Synthesis of **VI** via Eastern-Western route with standard reactions.

Pyrrole **S2** was protected by reaction with triisopropylsilyl (TIPS) chloride to give the *N*-TIPS derivative **S3**. The latter was then subjected to selective β-bromination to afford 2-bromo-4-carboethoxy-5-methylpyrrole **S4**. The methyl group of **S4** was oxidized[30] to give 4-bromo-2-formylpyrrole **S5**, which lost the TIPS group during the oxidation. Various conditions were examined to improve the yield of the oxidation; however, no improvement was achieved (Table S1). Henry reaction of **S5** followed by subsequent dehydration afforded a nitroalkene intermediate (not shown), which was then reduced with NaBH$_4$ to give 2-(2-nitroethyl)pyrrole **VI** in 25% yield. Nevertheless, the low yield of CAN oxidation was found to be a significant bottleneck in route 1.

Table S1. Cerium ammonium nitrate oxidation of α-methylpyrrole **S4**.

Entry	CAN (equiv)	Reaction time (min)	Product **S5** (%)[a]
1[b]	3	10	6
2[b]	3	30	15
3[b]	4	40	20
4[b]	4	40	6[c]

[a] Isolated yield. [b] The reaction was carried out at 0.1 M in THF/AcOH/H$_2$O (1:1:1) at 0 °C. [c] The reaction was set up in the same conditions as entry 1 but the yield was poorer.

In pursuit of acquiring the target, ~10 mmol of **VI** is desired for the next five reactions. Hence, the synthetic sequence was rearranged as follows: (1) TIPS protection, (2) oxidation of α-methylpyrrole, (3) Henry reaction, (4) reduction, and (5) β-bromination (Scheme S1B, route 2). To our surprise, formylpyrrole **S6** was obtained in a moderate yield of 52%, which comprised a significant improvement from the result observed in the reaction affording the analogous pyrrole substrate **S5**.[29]   Analogous results were observed in the Henry reaction and reduction, where pyrrole **S7** was obtained in 51% yield. Compound **S7** underwent bromination using the established regioselective β-bromination conditions using 2,4,4,6-tetrabromo-2,5-cyclohexadien-1-one (TBCO).[21]   The major product was dibrominated derivative of **S7** (not depicted), primarily attributed to a lack of electronic (and steric) control, unlike for the reported substrate.[21]

The iron(III)-catalyzed reaction of **1** and **2** to form pyrrole **3** was carried out under various conditions[25,26] as shown in Table S2. Reaction in toluene at 0.1 M gave low yield (entry 1) and poorer yield at 0.2 M (entry 2). Homogeneous reactions were carried out and set up in acetonitrile and acetic acid[28] to uniformly distribute the catalyst in the system, but yield improvements were not observed (entries 3 and 4). Screening the catalytic amount from 15 to 30% surprisingly showed enhanced yield (entries 5–7), with 47% obtained at 20 mol% FeCl$_3$ (entry 6).

Table S2. Iron (III)-catalyzed formation of 1-bromonaphthylpyrrole **3**.

Entry	Concentration (M)	Solvent	FeCl$_3$ (%)	Product (%)[a]
1[b]	0.1	Toluene	10	26
2[b]	0.2	Toluene	10	19
3[b]	0.1	MeCN	10	22
4[b]	0.1	AcOH	10	22
5[b]	0.1	Toluene	15	37
6[b]	0.1	Toluene	20	47
7[b]	0.1	Toluene	30	43

[a] Isolated yield. [b] The reaction was carried out overnight at refluxing temperature.

Experimental section

The known compounds **S6**[29] and **S7**[29] were prepared as described in the literature.

4-Bromo-3-ethoxycarbonyl-2-methyl-1-(triisopropylsilyl)pyrrole (S4).

Following a standard procedure,[29] NaH 60% dispersion in mineral oil (4.32 g, 108 mmol) was introduced to a solution of ethyl 2-methyl-1*H*-pyrrole-3-carboxylate **S2** (9.22 g, 60 mmol) in THF (100 mL) at 0 °C. The resulting mixture was stirred at 0 °C for 30 min. TIPSCl (12.7 g, 66 mmol) was added dropwise. The reaction mixture was stirred at 0 °C for 1 h. The reaction mixture was diluted with water (100 mL) and extracted with ethyl acetate (3 x 100 mL). The combined organic extract was washed with brine (300 mL), dried over anhydrous Na_2SO_4, and then concentrated under reduced pressure to give a light-yellow oil crude. NBS (5.23 g, 29.4 mmol) was transferred portion wise into the crude solution of **S3** (6.97 g, 22.6 mmol) in THF (38.0 mL) at 0 °C over the course of 1 h. The reaction mixture was stirred at 0 °C for 3 h. The reaction mixture was diluted with ethyl acetate (60.0 mL), washed with water (60.0 mL) and brine (60.0 mL). Each aqueous solution was extracted with ethyl acetate (2 x 60.0 mL). The combined organic extract was dried over anhydrous Na_2SO_4 and then concentrated under reduced pressure. Column chromatography [silica, neat dichloromethane] afforded a yellow oil (4.87 g, 56%). ^1H NMR (500 MHz, $CDCl_3$) δ 6.68 (s, 1H), 4.31 (q, $J = 7.2$ Hz, 2H), 2.57 (s, 1H), 1.52 (sept, $J = 7.6$ Hz, 3H), 1.38 (t, $J = 7.1$ Hz, 2H), 1.12 (s, 9H), 1.13 (s, 9H); $^{13}C\{^1H\}$ NMR (150 MHz, $CDCl_3$) δ 164.6, 141.5, 124.6, 114.3, 98.3, 59.8, 18.1, 15.2, 14.4, 13.0; ESI-MS obsd 388.1304, calcd 388.1302 [$(M + H)^+$, M = $C_{17}H_{30}BrNO_2Si$].

4-Bromo-3-ethoxycarbonyl-2-formylpyrrole (S5).

Following an established procedure,[29] a sample of CAN (5.56 g, 10.1 mmol) was added to a solution of **S4** (0.99 g, 2.54 mmol) in THF/glacial acetic acid/water (1:1:1, 26.0 mL) at 0 °C. The resulting mixture was stirred at 0 °C for 40 min. The reaction mixture was poured into the ice and extracted with ethyl acetate (50.0 mL). The organic extract was washed with saturated aqueous $NaHCO_3$ (150 mL) and with brine (150 mL). Each aqueous solution was extracted with ethyl acetate (2 x 150 mL). The combined organic extract was dried over anhydrous Na_2SO_4 and then concentrated under reduced pressure. Column chromatography [silica, hexanes/ethyl acetate (9:1 to 7:3)] afforded an orange solid (124 mg, 20%): mp 117–118 °C; ^1H NMR (600 MHz, $CDCl_3$) δ 10.15 (d, $J = 0.74$, 1H), 9.79 (br, 1H), 7.10 (dd, $J = 3.0$, 0.76 Hz, 1H), 4.42 (q, $J = 7.2$ Hz, 2H), 1.42 (t, $J = 7.2$ Hz, 2H); $^{13}C\{^1H\}$ NMR (125 MHz, $CDCl_3$) δ 181.6, 162.3, 133.1, 125.5, 120.7, 61.2, 14.3; ESI-MS obsd 245.9761, calcd 245.9760 [$(M + H)^+$, M = $C_8H_8BrNO_3$].

4-Bromo-3-ethoxycarbonyl-2-(2-nitroethyl)pyrrole (VI) via route 1.

Following an established procedure,[29] a mixture of **S5** (124 mg, 0.50 mmol), potassium acetate (49.1 mg, 0.50 mmol), and methylamine hydrochloride (32.0 mg, 0.47 mmol) in THF/ethanol (4:1, 2.5 mL) was sonicated and stirred at room temperature for 10 min. Nitromethane (264 μL, 4.50 mmol) was added. The resulting mixture was stirred at room temperature for 4 h. The mixture was diluted with water (3.0 mL) and extracted with ethyl acetate (3 x 8.0 mL). The organic extract was washed with brine (30.0 mL), dried over anhydrous Na_2SO_4, and concentrated under reduced pressure to dryness. A mixture of chloroform and isopropanol (3:1, 7.0 mL) and silica (0.98 g) were then added to the residue. The resulting mixture was stirred at room temperature for 10 min. $NaBH_4$ was added in one portion. The reaction mixture was stirred at room temperature for 1 h. The mixture was filtered under reduced pressure. The filtrate was concentrated to dryness under reduced pressure. The crude solid was dissolved in dichloromethane (10.0

mL), washed with water (10.0 mL), and washed with brine (10.0 mL). Each aqueous solution was extracted with ethyl acetate (2 x 10.0 mL). The combined organic extract was dried over anhydrous Na_2SO_4 and then concentrated under reduced pressure. Column chromatography [silica, hexanes/ethyl acetate (9:1 to 7:3)] afforded a yellow solid (36.5 mg, 25%): mp 112–113 °C; ^{1}H NMR (500 MHz, CDCl$_3$) δ 8.65 (br, 1H), 6.73 (d, J = 2.6 Hz, 1H), 4.67–4.73 (m, 2H), 4.32 (q, J = 7.1 Hz, 2H), 3.53–3.58 (m, 2H), 1.39 (t, J = 7.1 Hz, 3H); ^{13}C{^{1}H} NMR (150 MHz, CDCl$_3$) δ 163.9, 134.0, 118.9, 111.8, 97.9, 74.4, 60.3, 25.8, 14.3; ESI-MS obsd 290.9977, calcd 290.9975 [(M + H)$^+$, M = $C_9H_{11}BrN_2O_4$].

Attempted bromination of S7.

Following an established procedure,[21] a mixture of **S7** (770 mg, 3.63 mmol), 2,4,6-tribromophenol (2.40 g, 7.25 mmol), and K_2CO_3 (1.81 g, 13.1 mmol) in acetonitrile (36.0 mL) was cooled to 0 °C and stirred for 15 min. TBCO (2.45 g, 6.00 mmol) was added portionwise at 0 °C over the course of 1 h. The reaction mixture was further stirred at 0 °C for 1 h. The reaction mixture was diluted with ethyl acetate (40.0 mL) and then washed with 10% NaHSO$_3$ (80.0 mL), saturated NaHCO$_3$ (80.0 mL), and brine (80.0 mL). Each aqueous solution was extracted with ethyl acetate (2 x 80.0 mL). The combined organic extract was dried over anhydrous Na_2SO_4 and then concentrated under reduced pressure. Column chromatography [silica, hexanes/ethyl acetate (9:1 to 7:3)] afforded a dark-brown solid. The ^{1}H NMR analysis indicated the absence of two pyrrole hydrogen atoms, consistent with dibromination: ^{1}H NMR (600 MHz, CDCl$_3$) δ 8.74 (br, 1H), 4.67–4.72 (m, 2H), 4.29–4.36 (q, 2H), 3.51–3.57 (m, 2H), 1.39 (t, J = 7.1 Hz, 2H).

Section S2

Single-Crystal
# X-ray Data

Table S3. Summary of single-crystal X-ray data for compound **3**.

3
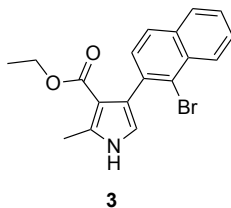
CCDC registry	2327783
Formula	$C_{18}H_{16}BrNO_2$
Formula Weight (g/mol)	358.23
Crystal Dimensions (mm)	$0.21 \times 0.18 \times 0.11$
Crystal System	Monoclinic
Space Group	P 1 21/c 1
Temperature (K)	100
a (Å)	17.6763(5)
b (Å)	11.7042(3)
c (Å)	7.5524(2)
α (°)	90
β (°)	94.840(1)
γ (°)	90
V (Å^3)	1556.92(7)
Number of reflections for cell measurement	9320
θ range (°) for cell measurement	2.3-27.0
Z	4
F(000)	728.0
ρ (g/cm^3)	1.528
λ (Å, Mo Kα)	0.71073
μ (mm^{-1})	2.647
Max 2θ for data collection (°)	53.9
Measured fraction of data	0.999
Number of reflections measured	3304
Number of parameters in least-squares	195
R1	0.0309
wR$_2$	0.0817
R1 (all data)	0.0327

Table S4. Summary of single-crystal X-ray data for compound **5**.
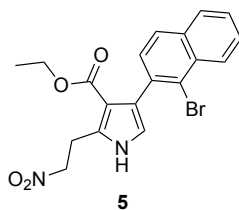
CCDC registry	2327784
Formula	$C_{19}H_{17}BrN_2O_4$
Formula Weight (g/mol)	417.25
Crystal Dimensions (mm)	$0.60 \times 0.10 \times 0.07$
Crystal System	Monoclinic
Space Group	P 1 21/c 1
Temperature (K)	100
a (Å)	12.445(3)
b (Å)	12.529(3)
c (Å)	11.461(2)
α (°)	90
β (°)	93.804(5)
γ (°)	90
V (Å^3)	1783.1(6)
Number of reflections for cell measurement	9898
θ range (°) for cell measurement	2.4–26.7
Z	4
$F(000)$	848.0
ρ (g/cm^3)	1.554
λ (Å, Mo Kα)	0.71073
μ (mm^{-1})	2.333
Max 2θ for data collection (°)	52.772
Measured fraction of data	0.999
Number of reflections measured	3650
Number of parameters in least-squares	260
R1	0.0353
wR$_2$	0.0909
R1 (all data)	0.0417

Table S5. Summary of single-crystal X-ray data for compound **7**.
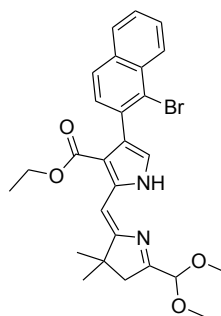
7

|	
CCDC registry	2327785
Formula	$C_{27}H_{29}BrN_2O_4$
Formula Weight (g/mol)	525.43
Crystal Dimensions (mm)	$0.72 \times 0.57 \times 0.33$
Crystal System	Monoclinic
Space Group	P 1 21/c 1
Temperature (K)	100
a (Å)	14.7636(4
b (Å)	11.7049(3)
c (Å)	15.5223(5)
α (°)	90
β (°)	113.075(1)
γ (°)	90
V (Å^3)	2467.74(12)
Number of reflections for cell measurement	9449
θ range (°) for cell measurement	2.4–27.1
Z	4
F(000)	1088.0
ρ (g/cm^3)	1.414
λ (Å, Mo Kα)	0.71073
μ (mm^{-1})	1.702
Max 2θ for data collection (°)	53.256
Number of reflections measured	5441
Number of parameters in least-squares	374
R1	0.0349
wR$_2$	0.0820
R1 (all data)	0.0384

Section S3

Absorption Spectra
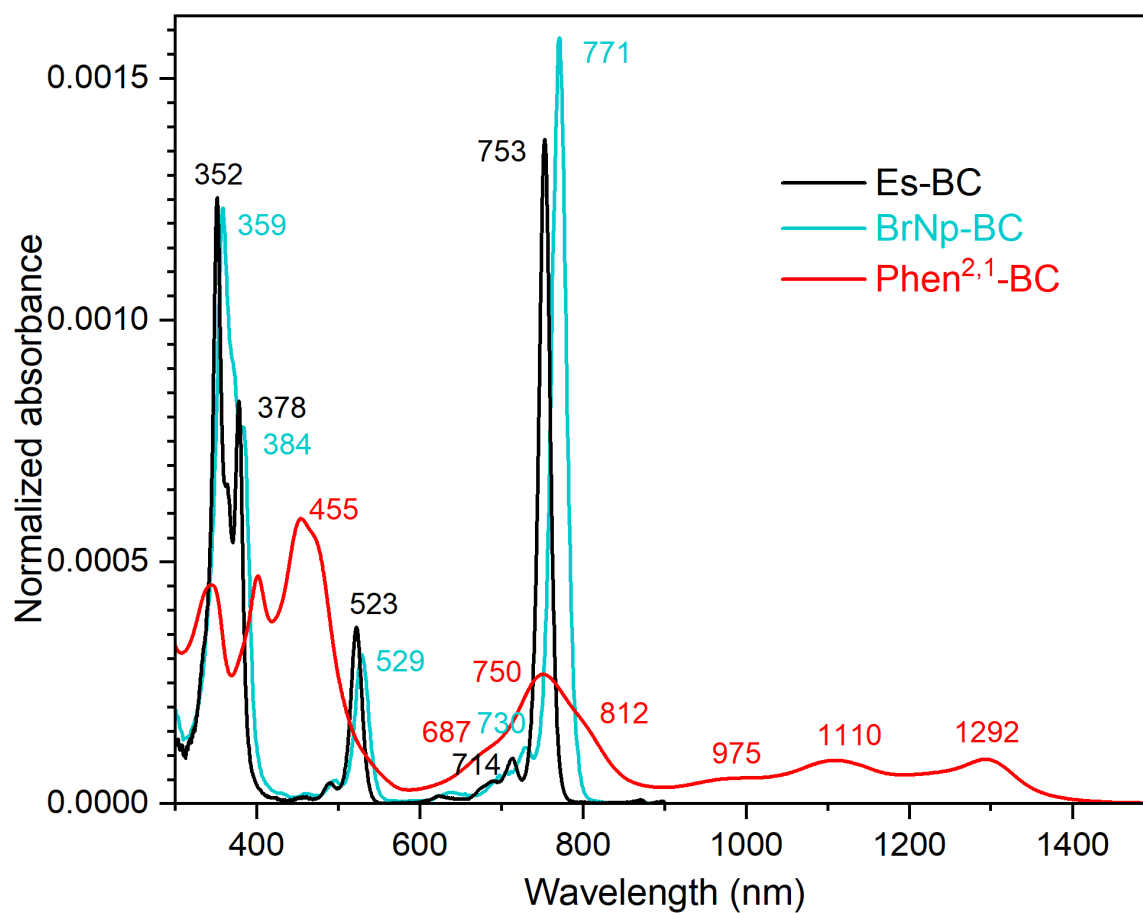
Figure S1. Absorption spectra of **Es-BC** (black), **BrNp-BC** (cyan), and **Phen^{2,1}-BC** (red) normalized to the oscillator strength of the $S_0 \rightarrow S_1$ manifold obtained from TDDFT calculations.
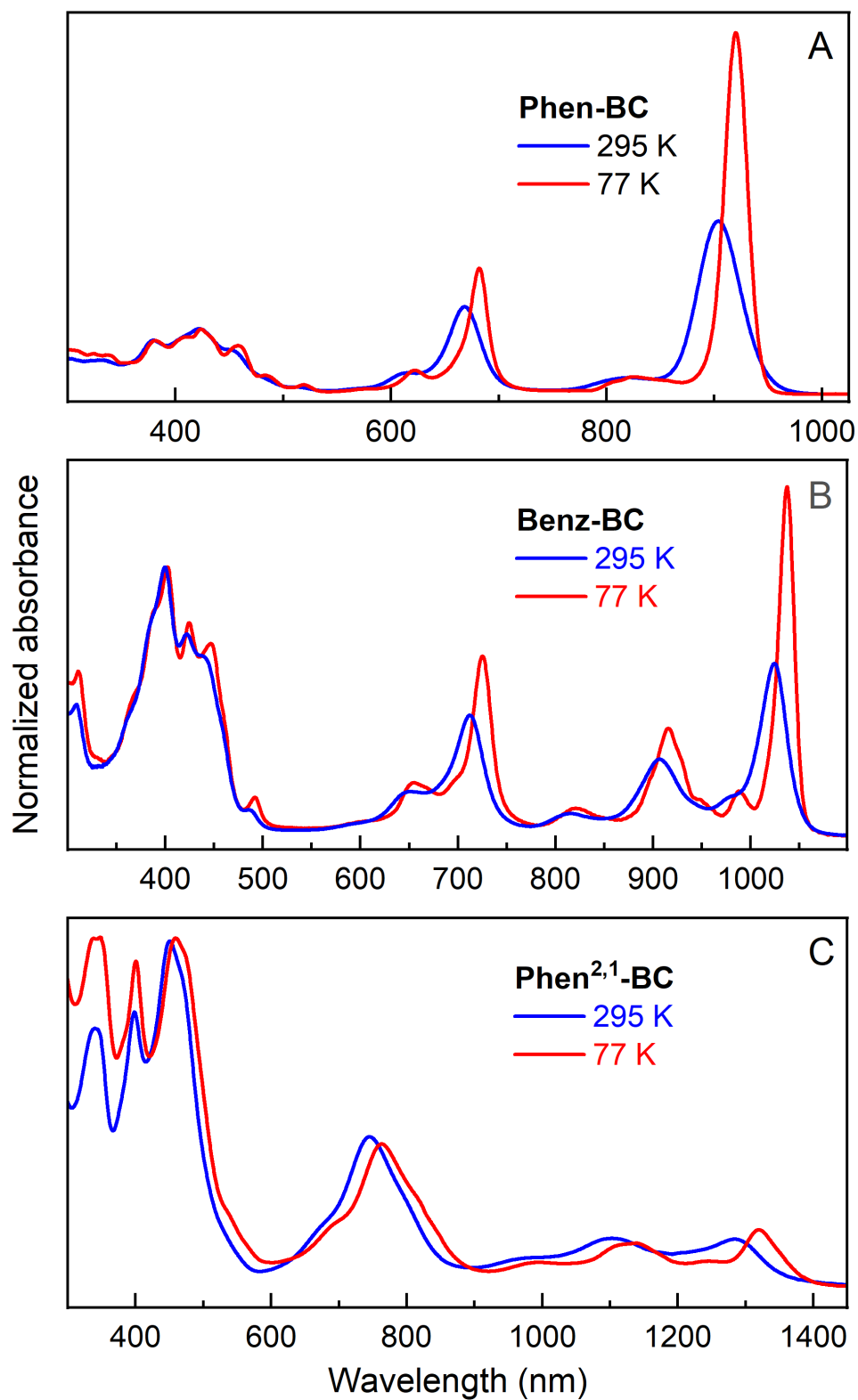
Figure S2. Absorption spectrum of (A) **Phen-BC**, (B) **Benz-BC** and (C) **Phen^{2,1}-BC** in 2-methyl tetrahydrofuran at 295 K (blue) and 77 K (red) normalized at the blue-region maximum.

Table S6. Spectral Properties of annulated bacteriochlorins in 2-MeTHF at 77 K.

Compound	Progression	Band	λ (nm)	shift (cm^{-1})
Phen-BC	A	$S_1(0,0)$	920	
		$S_1(1A,0)$	824	1258
Benz-BC	A	$S_1(0,0)$	1037	
		$S_1(1A,0)$	990	458
		$S_1(2A,0)$	945	481
	B	$S_1(0,0)$	1037	
		$S_1(1B,0)$	915	1286
		$S_1(2B,0)$	819	1281
Phen^{2,1}BC	A	$S_1(0,0)$	1321	
		$S_1(1A,0)$	1245	462
		$S_1(2A,0)$	1171	508
		$S_1(3A,0)$	1105	510
	B	$S_1(0,0)$	1321	
		$S_1(1B,0)$	1145	1163
		$S_1(2B,0)$	991	1357

Section S4

Determination of Fluorescence Yields

Topic S1. Fluorescence yields.

The data in Figure S3 were used to calculate fluorescence quantum yields of **Benz-BC** and **Phen^{2,1}-BC**. In panel A, the instrument parameters (slit widths, integration time) were set to obtain a non-saturated spectrum for **Phen-BC** and the same parameters used for **Benz-BC** and **Phen^{2,1}-BC**. The area under the emission profile (800–1400 nm) for each spectrum was then used to calculate Φ_f for **Benz-BC** and **Phen^{2,1}-BC** using the previously determined value of 0.004 for **Phen-BC**. The Φ_f values for **Benz-BC** and **Phen^{2,1}-BC** are estimated to be 2.5×10^{-4} and $<2\times10^{-5}$, respectively. In panel B, the slits were opened such that **Phen-BC** emission was saturated near the peak (~910–990 nm) and the spectrum for **Benz-BC** was somewhat improved. The integrated area (990–1450 nm) was used to calculate Φ_f for **Benz-BC** to be 2.1×10^{-4} and that for and **Phen^{2,1}-BC** to be $<3\times10^{-5}$. Collectively, these measurements provide Φ_f values of 2.3×10^{-4} and $<3\times10^{-5}$ for **Benz-BC** and **Phen^{2,1}-BC**, respectively.

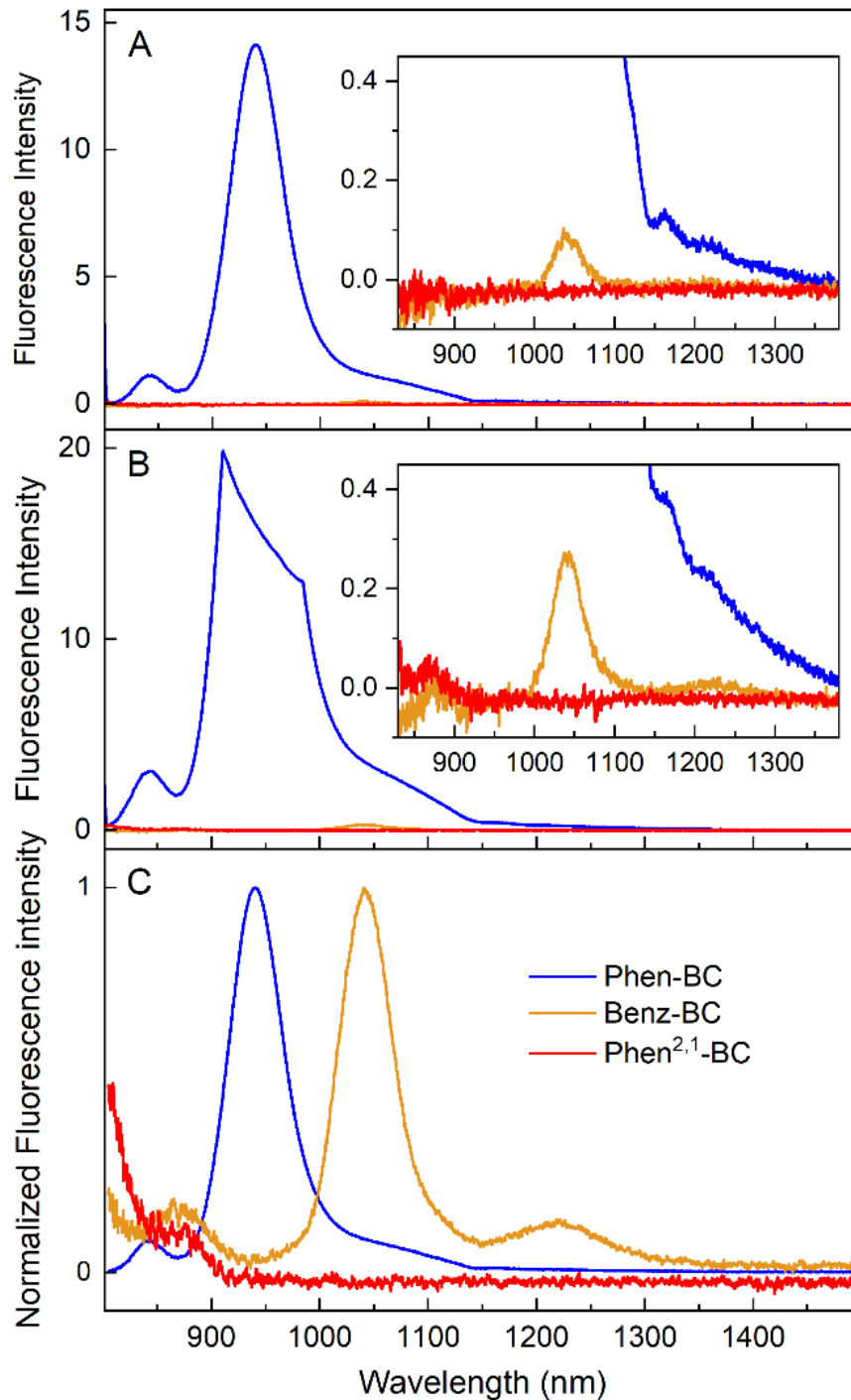Figure S4 extends the measurements to 1650 nm, again showing no emission from **Phen^{2,1}-BC**.

Figure S3. Fluorescence spectra of **Phen-BC** (blue), **Benz-BC** (gold) and **Phen^{2,1}-BC** (red). No emission attributable to **Phen^{2,1}-BC** was recorded in the spectral range shown. (A) Spectra recorded with settings for which emission of **Phen-BC** is on scale. (B) Spectra recorded with settings for which peak emission from **Phen-BC** is saturated. (C) Emission spectra for **Phen-BC** and **Benz-BC** recorded at different settings and then normalized at the peak intensity; the data for **Phen^{2,1}-BC** were recorded using the same settings as used for **Benz-BC**. The small emission peak in the 800–900 nm range for each sample is the (0,1) fluorescence band of trace non-annulated bacteriochlorin precursor that has a significantly higher fluorescence quantum yield.
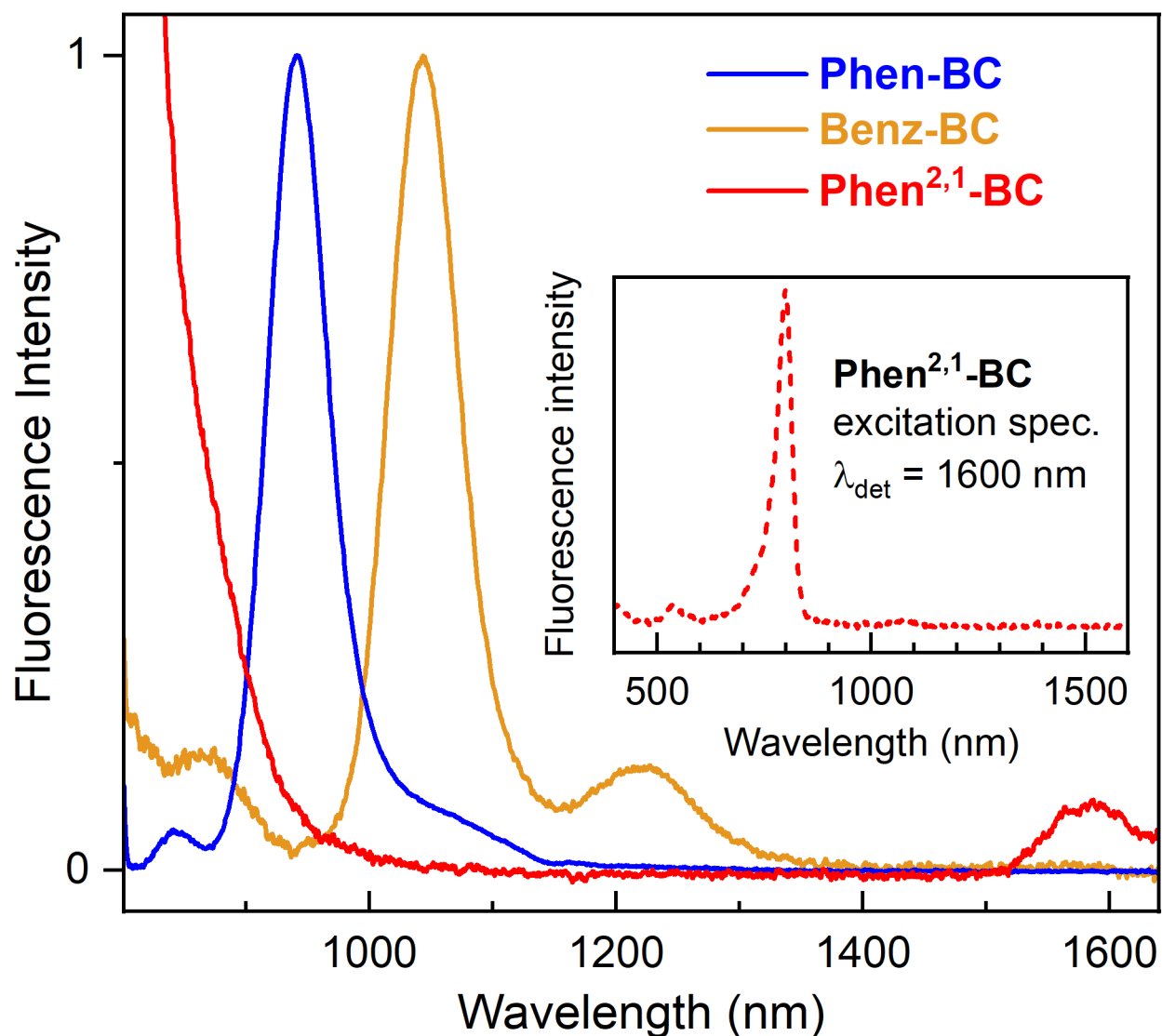
Figure S4. Fluorescence spectra for annulated bacteriochlorins as in the prior figure but extended to 1650 nm. The inset shows the excitation spectrum of the weak feature observed at ~1600 nm from the **Phen²,¹-BC** sample. This feature reflects 2nd order diffraction of emission at ~800 nm from trace non-annulated bacteriochlorin such as synthetic precursor **BrNp-BC** in the **Phen²,¹-BC** sample. Thus, no emission verifiable by excitation spectra is observed for **Phen²,¹-BC** itself.

Section S5

Analysis of Transient Absorption Data for Phen^{2,1}-BC

Topic S2. Transient-absorption difference spectra and kinetics.

Figure S5A shows transient absorption (TA) difference spectra for **Phen^{2,1}-BC** in toluene at several times after excitation with an ~100 fs flash at 500 nm. The dashed vertical line at ~815 nm indicates that the data in nominal "visible" region (~400–815 nm) and the NIR region (~815–1450 nm) were acquired (and analyzed) separately and spectra in the two regions joined. Figure S5B gives the ground-state absorption spectrum as a reference for features in the TA spectra. The TA difference spectrum at 0.3 ps (Figure S5A, blue trace) has features corresponding to bleaching of the ground-state absorption at ~450, 750, 1110, and 1295 nm, as well as excited-state absorption bands at ~530 and 875 nm. Excited-state stimulated emission (gain in the probe pulse) may contribute along with ground-state bleaching to the negative-going feature at ~1295 nm. By 10 ps (red trace), the bleaching features at ~1110 and 1295 nm have decayed to ~25% of the initial amplitude and the excited-state absorption bands at ~530 and 875 nm have decayed to 10%. All features are basically gone by 50 ps and the difference spectrum is back at the $\Delta A = 0$ line (gold trace).

Figure S5 panels C–H give kinetic traces at various wavelengths and single-wavelength (not global) fits to function consisting of two exponentials plus a constant convolved with the instrument response. These fits and those at other wavelengths across the visible and NIR reveal that one component has a subpicosecond time constant (~0.3–0.8 ps) and the other a value of ~10 ps (7–15 ps). Consistent with the time evolution of the TA difference spectra (Figure S5A), the decay profile at most wavelengths is dominated by the subpicosecond component.

Topic S3. Decay associated difference spectra (DADS).

The TA difference spectra in Figure S5A and ground-state absorption spectra in Figure S5B are reproduced in Figures S6A and S6E, respectively. The data set in the visible region (~400–815 nm) and the NIR region (~815–1450 nm) were independently subjected to global analysis. The results are shown in Figures S6 panels B–D and the inset to Figure S6E. Figure 6B shows the decay associated difference spectra (DADS) obtained from global fitting in which each component is given an initial unity concentration and they decay in parallel (*i.e.*, independent of one another). In short, DADS are the spectra of the pre-exponential factors of the exponential fitting functions. A positive DADS feature reflects decay of excited-state absorption or growth of ground-state bleaching (and/or stimulated emission) and a negative feature reflects growth of excited-state absorption or decay of ground-state bleaching (and/or stimulated emission). The time constants associated with the DADS components are listed on Figure S6B.

The subpicosecond component from the visible-region data (0.3 ps) has about one-half the time constant than that from the NIR data (0.6 ps). The short-lived DADS component is characterized by bleaching-decay features at ~455, 770, 1130, and 1315 nm and excited-state absorption decay features at ~550 and 870 nm. The longer-lived DADS with a 11 ps (visible) and 13 ps (NIR) time constant have negative-going features that are hypsochromically shifted by ~5 nm from (1) the ground-state bleaching features of the shorter-lived component (Figure S6B), and (2) the positions of the ground-state absorption peaks (Figure S6E). The implication of these shifts are discussed below.

Topic S4. Evolution associated difference spectra (EADS).

Figure S6C shows the evolution-associated difference spectra (EADS) that result from global analysis of the TA data sets with a serial kinetic model (Figure S7B). The EADS are linear combination of DADS. Differing from DADS, EADS negative features are associated with either formation or decay of a ground-state bleaching, and positive features are associated with either formation or decay of an excited-state feature. For **Phen[2,1]-BC** in toluene, the most notable difference between the EADS (Figure S6C) and DADS (Figure S6B) is that the EADS for the short-lived (~0.3–0.6 ps) component has narrower negative-going features at ~1115 nm and ~1295 nm. This difference suggests that spectral evolution involves more than decay of ground-state bleachings. The evolution additionally involves formation of transient absorption features (albeit weak) at ~1190 nm and ~1390 nm that are bathochromically shifted from the original ground-state positions. As discussed below (see Figure S7D), such characteristics are consistent rapid excited-state decay producing a vibrationally "hot" ground state (giving the shifted transient absorption), which then relaxes to the original ground state (giving the bleachings).

Topic S5. Species associated difference spectra (SADS).

The serial decay model for EADS in Figure S7B is one limiting case of the more general branched-decay model shown in Figure S7A that produces species associated difference spectra (SADS). Here State0 is produced by excitation (unity concentration) and then decays by two pathways: (i) to the original (relaxed) ground state with rate constant k_{0G} and (ii) to State1 with rate constant k_{01}. The values are such that $k_{0G} + k_{01} = (0.4 \text{ ps})^{-1}$ (the inverse of the average time constant of the short-lived component from the visible and NIR DADS). The input values of k_{0G} and k_{01} define the yield of State1 from State0 to be $\Phi_{01} = k_{01}/(k_{0G} + k_{01})$ and a yield of the original (relaxed) ground state from State0 to be $\Phi_{0G} = k_{0G}/(k_{0G} + k_{01})$. State1 then decays to the original ground state with rate constant $k_{1G} = (12 \text{ ps})^{-1}$, chosen from the NIR DADS where decay of this state makes the largest contribution.

Figures S8 and S9 gives SADS runs in which Φ_{01} varies from 0.1 to 0.9 (and Φ_{0G} from 0.9 to 0.1). In the limit that $k_{0G} = 0$, $k_{01} = (0.4 \text{ ps})^{-1}$, $\Phi_{0G} = 0$ and $\Phi_{01} = 1$, the SADS model (Figure S7A) defaults to the EADS model (Figure S7B). For $k_{0G} = 0$ and $k_{01} = (0.4 \text{ ps})^{-1}$ ($\Phi_{0G} = 0$ and $\Phi_{01} = 1$), (EADS in Figure S6C), the $S_1(1,0)$ bleaching (~1115 nm) and $S_1(1,0)$ bleaching (~1295 nm) have much smaller amplitude for the long-lived (~10–13 ps) component (red) compared to those for the short-lived (0.3–0.6 ps) component (blue). The SADS run shown in Figure S6D (and the inset to Figure S6E) uses "median" input values of $k_{0G} = (0.8 \text{ ps})^{-1}$ and $k_{01} = (0.8 \text{ ps})^{-1}$ ($\Phi_{0G} = 0.5$ and $\Phi_{01} = 0.5$). In this case, the $S_1(1,0)$ and $S_1(0,0)$ bleaching amplitudes for the long-lived component (red) approach being comparable in amplitude to those for the short-lived component (blue). Continuing the trend, SADS runs in which $k_{0G} > k_{01}$ ($\Phi_{0G} > \Phi_{01}$), the $S_1(1,0)$ and $S_1(1,0)$ bleaching amplitudes for the long-lived component are larger in amplitude to those for the short-lived component.

The above-noted trend occurs because the intensity axis for the DADS, EADS, and SADS is $\Delta\varepsilon$ (difference in extinction coefficient for the transient state versus the ground state), with units such that the initial concentration (C) is 1 for the relevant initial components. At each time and wavelength, the global fitting finds the best values of $\Delta\varepsilon$ and C for each component/species to fit

the measured $\Delta A = \Delta\varepsilon \bullet C$ for a unity pathlength. For the SADS run in Figure S6D, the amount of State1 ($\tau \sim 12$ ps) produced from State0 ($\tau \sim 0.4$ ps) is $\Phi_{01} = 0.5$ whereas for the EADS run in Figure S6C the yield of State1 is $\Phi_{01} = 1$. Thus, the lower C of State1 for that SADS versus the EADS means that the computed $\Delta\varepsilon$ must be larger for the SADS versus EADS to fit the same measured ΔA spectra.

The question is what spectra are physically reasonable for the SADS, which must be viewed as simulations and not fits. If for the sake of argument neither State0 nor State1 in the SADS analysis has any transient absorption across the 900–1450 nm region of the $S_0 \rightarrow S_1$ ground-state absorption manifold, then the SADS for both State1 (12 ps) and State0 (4 ps) in Figure S6D would both simply be bleaching of the ground-state absorption profile in Figure S6E and with identical amplitude. That is roughly the case in Figure S6D, wherein $k_{0,G} = k_{0,1} = (0.8\text{ ps})^{-1}$ and $\Phi_{0,G} = \Phi_{0,1} = 0.5$, given the differences in spectral shapes of the NIR bleaching manifolds of the 12-ps and 4-ps SADS. SADS runs that have larger-amplitude NIR bleach manifold for State1 than State0 ($k_{0,G} > k_{0,1}$ and $\Phi_{0,G} > \Phi_{0,1}$) are physically unreasonable. The reverse situation including the EADS limit ($k_{0,G} = 0$, $k_{0,1} = (0.4\text{ ps})^{-1}$, $\Phi_{0,G} = 0$ and $\Phi_{0,1} = 1$) gives a smaller-amplitude NIR bleach manifold for State1 (12 ps) than State0 (0.4 ps), as in Figure S6C. This is reasonable because, as noted above, these spectra show transient absorption features (albeit weak) at ~1190 nm and ~1390 nm, namely to longer wavelength than the $S_1(0,0)$ bleaching at ~1115 nm and $S_1(1,0)$ bleaching at ~1195 nm, respectively. Simulations discussed below show that transient absorption bands that are bathochromically shifted and broader than the corresponding bleached ground-state absorption bands afford spectral destructive interference in the difference spectra and can give rise to the EADS (or SADS) for the 12-ps component shown in Figure S6C (red).

Topic S6. Analysis of the kinetic models.

The model shown in Figure S7C is one specific case of the general model shown in Figure S7A in which State0 is an unrelaxed (vibrationally, conformationally, solvation) form of the lowest excited singlet state (S_1) of **Phen^{2,1}-BC**. Decay to the relaxed S_1 requires ~0.4 ps, followed by internal conversion of S_1 to the ground state S_0. One of the problems with this model is that it is difficult to explain the substantial decay of ground-state bleachings, particularly in the NIR (~900–1500 nm) S_1 manifold between 0.3 and 10 ps (Figure S6A).

The model shown in Figure S7D is a specific case of the general model shown in Figure S7A in which State0 is the lowest excited singlet state (S_1) of **Phen^{2,1}-BC**. State1 is the vibrationally "hot" ground state in which ~1 eV of electronic energy is deposited in ~0.4 ps and converted into vibrational degrees of freedom. The ~12-ps decay time reflects "cooling" of the vibrationally "hot" ground state as thermal equilibrium is attained by flow of the excess energy into the solvent.

A time scale of ~10 ps or longer has been observed for vibrational cooling of large aromatic systems[46-53] including tetrapyrroles[54,55] It is likely that the S_1 excited state (nominal ~0.4 ps lifetime) has not vibrationally relaxed prior to internal conversion because internal vibration redistribution of such large aromatic systems often takes >1 ps.[46,47,50-52] The vibrationally unrelaxed status of S_1 is mapped onto S_0 and thus internal vibrational relaxation within S_0 likely contributes at early times in the ~12 ps "cooling" process. The dynamics are rigorously more

complex than can be captured with a single SADS and mono-exponential decay.[54,55]

Such a situation is complex and captured in simplified form here in the global analysis as a SADS (or EADS) with a single spectral shape that decays uniformly away. However, in reality IVR and vibrational cooling reflect the evolution of a distribution of sub-states characterized by an asymmetric spectral profile that is broadened to longer wavelengths (*i.e.*, as in hot-band absorption). This asymmetric transient profile compresses to shorter wavelength and shrinks in amplitude during vibrational equilibration because the hottest (longest-wavelength absorbing) components decay more rapidly.

In spite of the complexity, we have attempted to capture the main elements of the EADS (or SADS) from global analysis by simulating the spectrum of the vibrationally hot ground state of **Phen^{2,1}-BC**. First, the ground-state absorption spectrum of **Phen^{2,1}-BC** in toluene (Figure S10A) was fit to the sum of seven Gaussians. Five of the Gaussians are employed in the 420–1500 nm region shown in Figure S10B, which is the wavelength span of the TA data. Each Gaussian peak in the ground-state absorption spectrum was shifted by ~100 cm^{-1} to lower energy, which is 1.6 nm at 400 nm, 5.7 nm at 750 nm, and 17 nm at 1300 nm (Figure S10C, blue). The multi-Gaussian fit profile for the ground-state spectrum (Figure S10B) was subtracted from the shifted spectrum (Figure S10C, blue) to give the difference spectrum shown in Figure S10D. As expected, the difference spectrum shows a series of derivative-like features, with each zero-crossing ($\Delta A = 0$) point in the vicinity of the corresponding ground-state absorption maximum. This exercise is a proof of concept, given that the features in the spectrum of a vibrationally-hot ground state are expected to not only be bathochromically shifted, but also broadened and with correspondingly diminished amplitude in order to maintain comparable integrated intensities (Figure S10C, magenta). Subtracting the multi-Gaussian fit profile for the ground-state spectrum (Figure S10B) from that for the shifted and broadened spectrum (Figure S10C, red) gives the difference spectrum shown in Figure S10E. The simulated spectrum in Figure S10E reproduces the main characteristics of the 12-ps EADS for **Phen^{2,1}-BC** shown in Figure S10F (reproduced from Figure S6C, red).
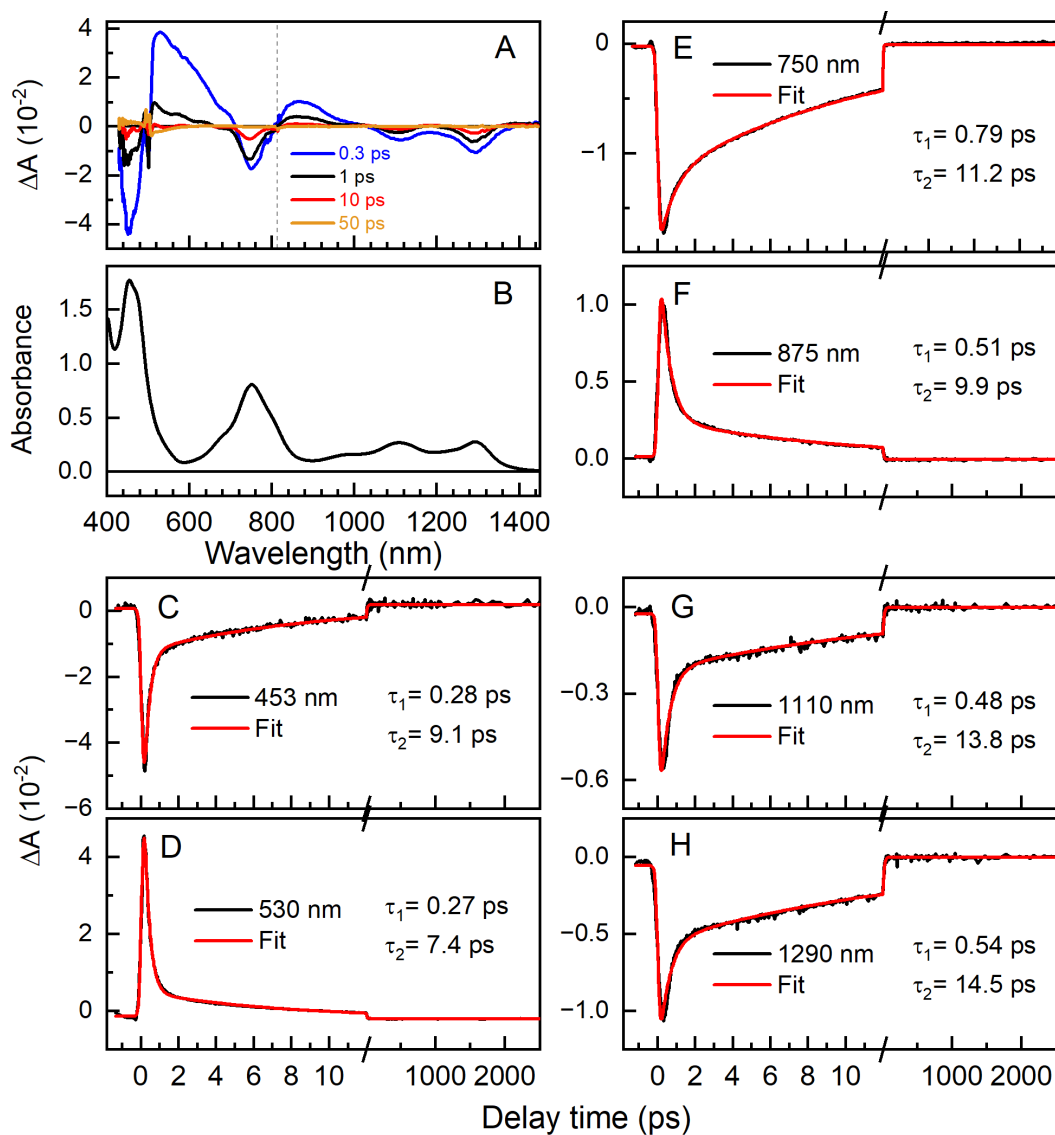
Figure S5. (A) Representative TA spectra for **Phen^{2,1}-BC** in Ar-purged toluene at select delay times after excitation at 500 nm. (B) Ground state absorption spectrum. (C–H) Kinetic traces (black) at the indicated wavelengths and fits (red) and derived time constants from single-wavelength fits of the TA data. The vertical dashed line at 815 nm in panel A marks the cutoff between the visible and visible and NIR data sets.
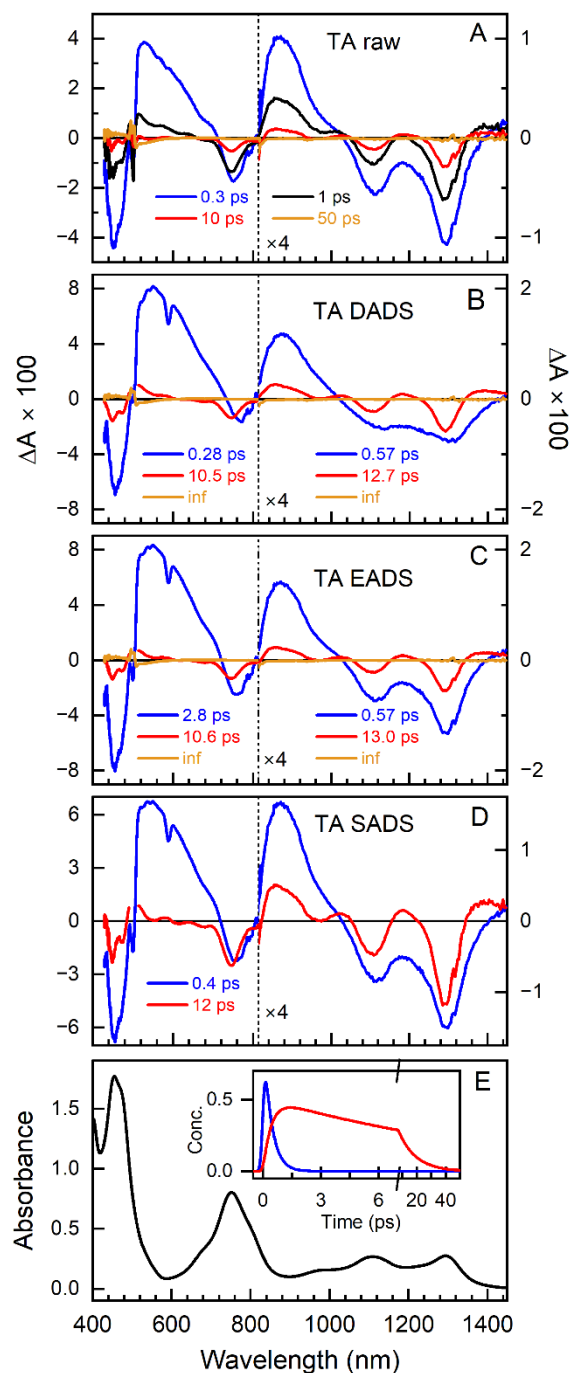
Figure S6. (A) Representative TA spectra at select delay times after excitation at 500 nm; (B) Decay-associated difference spectra (DADS); (C) Evolution-associated difference spectra (EADS); (D) Species-associated difference spectra (SADS); (E) Ground state absorption spectrum. The inset to panel E is for the SADS model and shows the time evolution of the concentrations for State0 (initial value of 1 upon excitation), which then decays to (i) to the original (relaxed) ground state with rate constant $(0.8 \text{ ps})^{-1}$ and (ii) State1 with rate constant $(0.8 \text{ ps})^{-1}$. These values give a lifetime of 0.4 ps for State0 and a yield of 50% for State1 (red), which decays to the original ground state with a rate constant of $(12 \text{ ps})^{-1}$. The vertical dashed line in A–D marks the cutoff between the visible and NIR data. The spectra in the NIR use a ΔA scale 4× smaller than used for the visible region (see left and right vertical axes). The DADS and EADS analyses include an "infinity" component that decays little or not at all on the time scale of the measurements, provides an asymptote for the decays and shows the expected $\Delta A \sim 0$ across the spectrum.
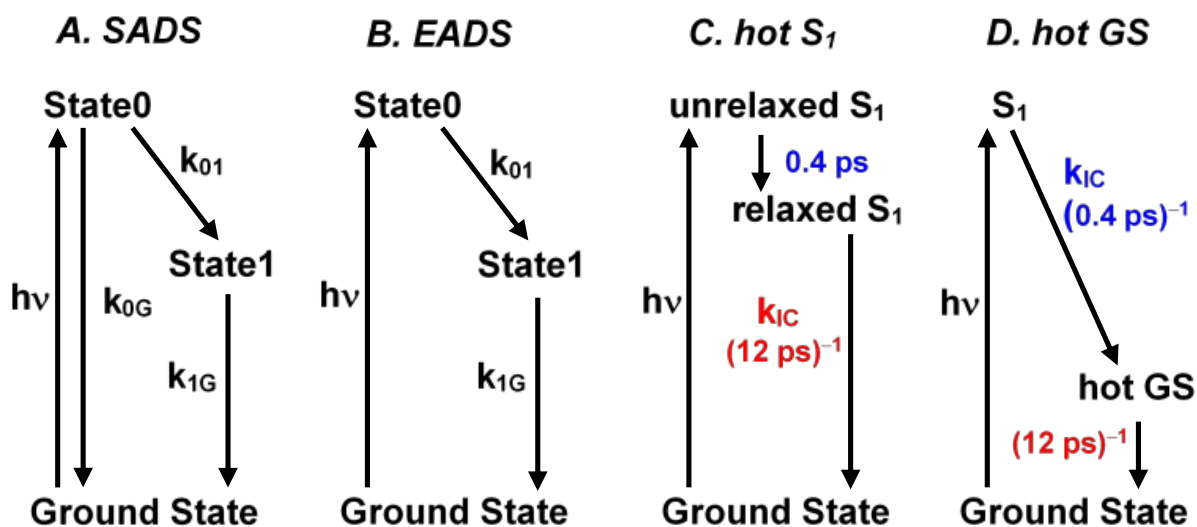
Figure S7. Kinetic Models. (A) General branched model for species-associated difference spectra (SADS) in which input values for k_{0G} and k_{01} define the lifetime of State0 and the yield of State1. (B) Serial decay model for evolution-associated difference spectra (DADS) in which k_{0G} from the model in panel A is eliminated. (C) Limiting model in which State0 is the vibrationally unrelaxed S1 excited state that decays to the relaxed State1 with a rate constant of $(4\ ps)^{-1}$. Internal conversion of the relaxed S1 to the ground state occurs with a rate constant of $(12\ ps)^{-1}$. (D) Limiting model in which State0 is the S1 excited state, which internally converts to the ground state with a rate constant of $(4\ ps)^{-1}$. The resultant "hot" ground state vibrationally "cools" with a rate constant of $(12\ ps)^{-1}$ to give the original (pre-flash) ground state.
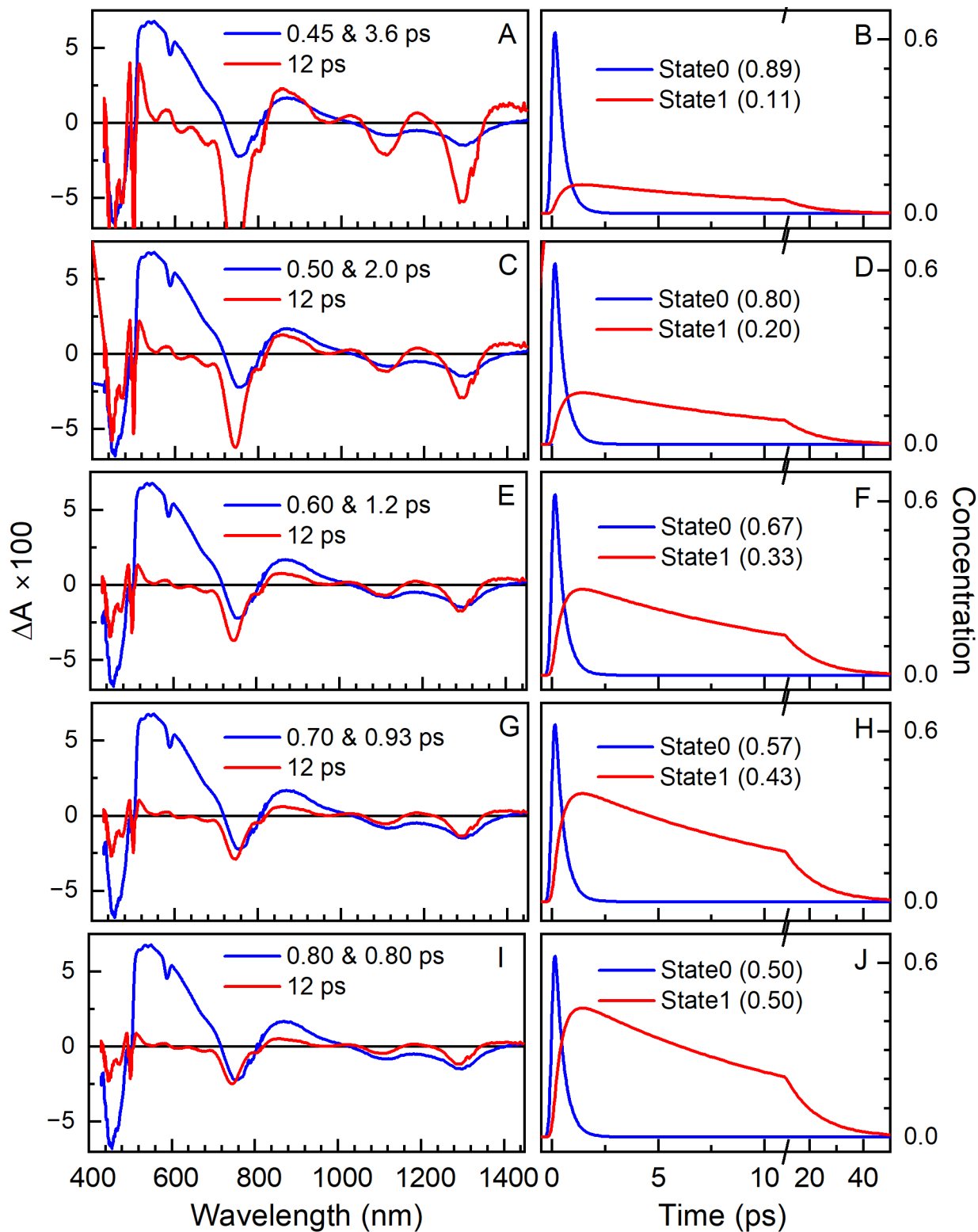
Figure S8. SADS analysis using the kinetic model in Figure S7A in which time constants $(k_{0G})^{-1}$ and $(k_{01})^{-1}$ (blue values at top of left panels) are such that Φ_{0G} varies from 0.89 to 0.50 and Φ_{01} varies from 0.50 to 0.11 89 (values after State0 and State1, respectively, in the right panels).
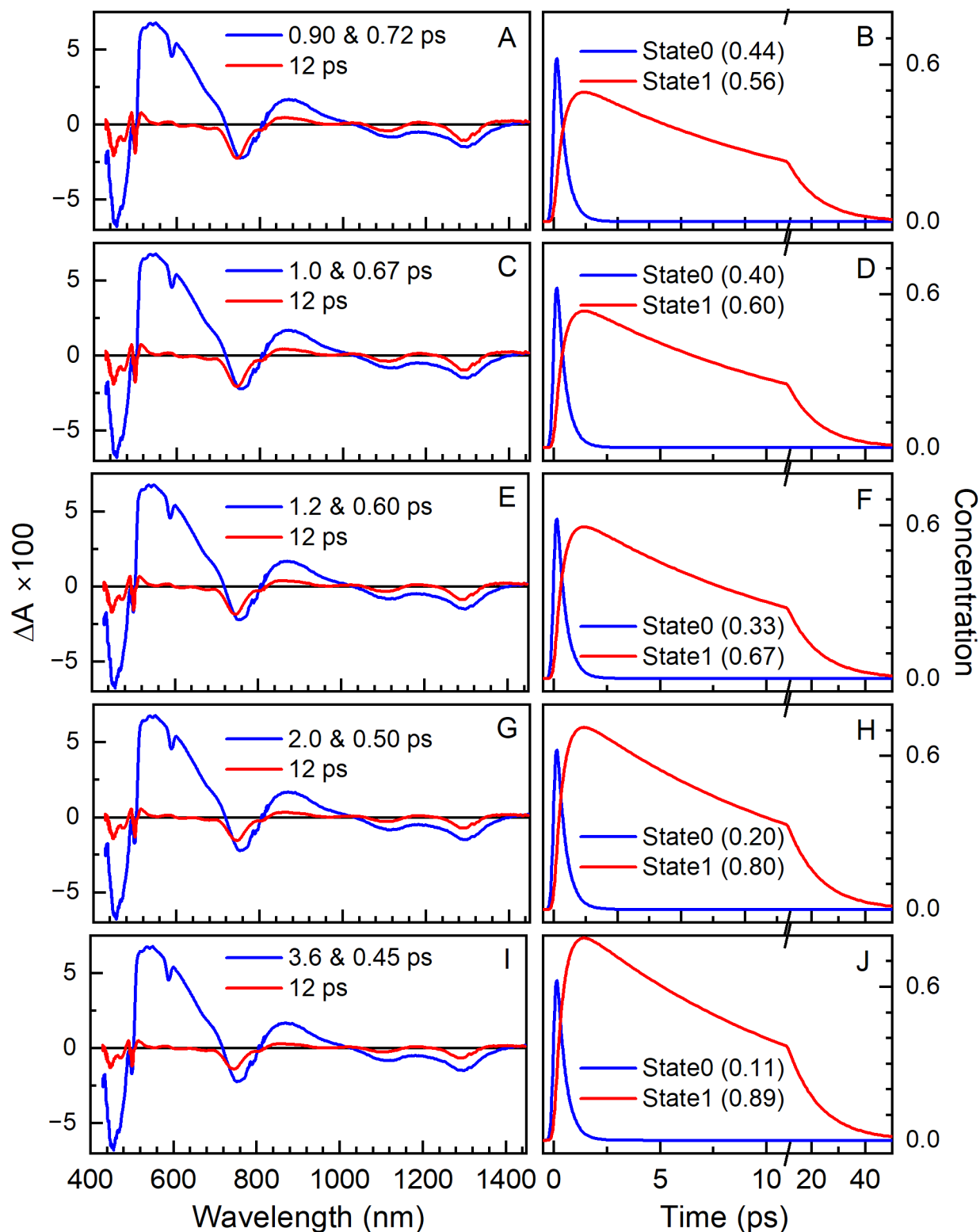
Figure S9. SADS analysis using the kinetic model in Figure S7A in which time constants $(k_{0G})^{-1}$ and $(k_{01})^{-1}$ (blue values at top of left panels) are such that Φ_{0G} varies from 0.44 to 0.11 and Φ_{01} varies from 0.56 to 0.89 (values after State0 and State1, respectively, in the right panels).
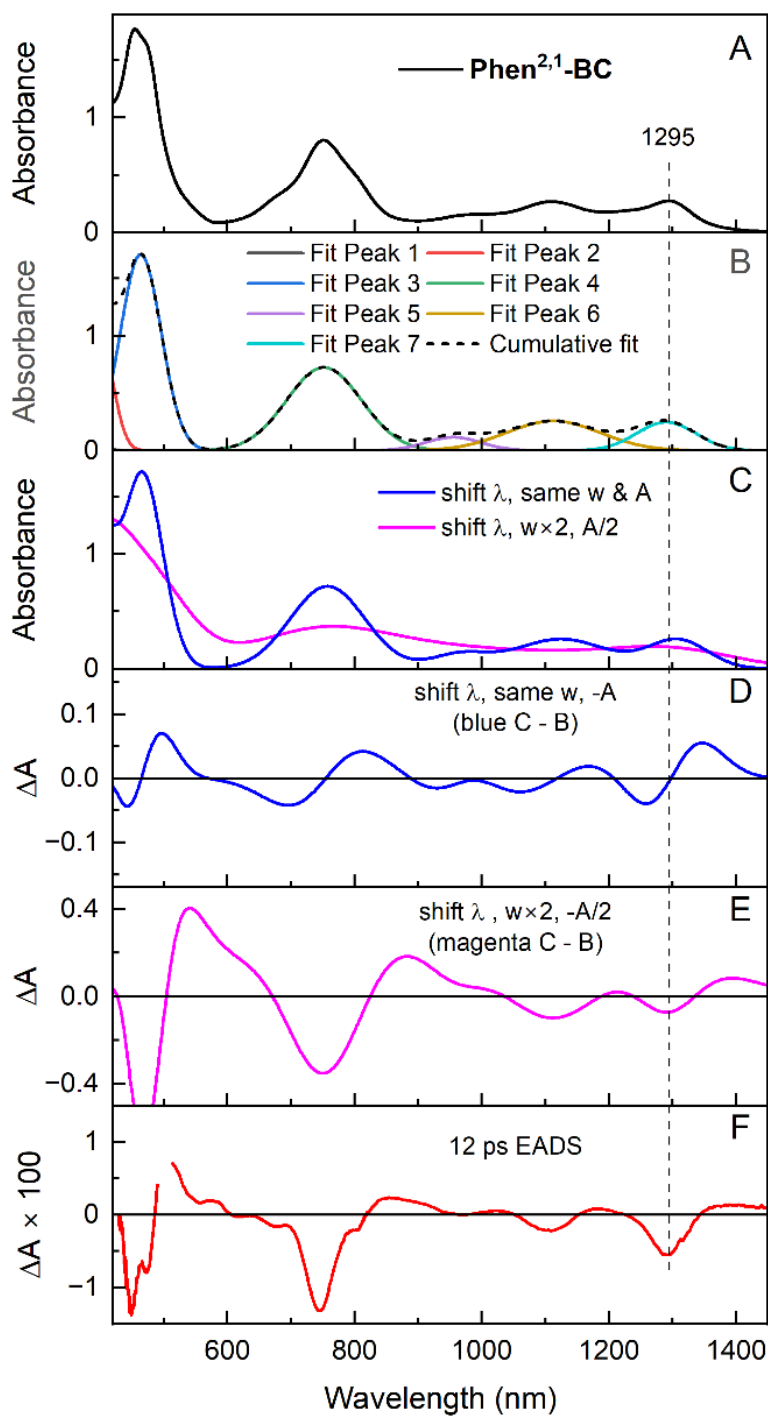
Figure S10. (A) Ground-state absorption spectrum of **Phen^{2,1}-BC** in toluene. (B) Multi-Gaussian fit, with two of the seven Gaussians being for features at shorter wavelengths (401 and 330 nm) that are not shown. (C) Simulated spectrum in which the Gaussians for the ground-state spectrum are shifted to lower energy by 100 cm^{-1} with widths (w) and amplitudes (A) unchanged (blue) or shifted to lower energy by 100 cm^{-1} with the widths doubled and amplitudes reduced two-fold (magenta). (D) Difference spectrum obtained by subtracting the ground-state spectrum in panel B from the blue (shifted) spectrum in panel C. (E) Difference spectrum obtained by subtracting the ground-state spectrum in panel B from the magenta (shifted and broadened) spectrum in panel C. (F) The 12-ps EADS from global analysis reproduced from Figure S10C for comparison with the simulated spectrum in panel E.

Chart S1. Bacteriochlorins for which data are given in Figure 4 of the main paper (reproduced below).

Energy-gap law plot showing the natural logarithm of the rate constant for $S_1 \rightarrow S_0$ internal conversion versus the S_1 energy for various bacteriochlorins (Figure 4 of the paper).

Section S6

Transient Absorption
Data for BrNp-BC

Topic S7. Analysis of TA data for **BrNp-BC.**

TA data were acquired for bacteriochlorin **BrNp-BC**, the synthetic precursor (containing two bromonaphtho groups) for **Phen^{2,1}-BC** (Scheme 2). Data were acquired using excitation in the Q_x ($S_0 \rightarrow S_2$) band at 529 nm and in the Q_y ($S_0 \rightarrow S_1$) band at 760 nm. Representative TA data and the results of global analysis are given in Fig. S11 and S12. Analysis affords a time constant of ~10 ps for relaxation (vibrational, conformational, solvent) in the S_1 excited state and S_1 excited-state lifetime of 500 ps (average from all the measurements). Comparison of the extent of bleaching in the Q_y and Q_y ground-state absorption bands at 10 ps for the lowest singlet excited state S_1 and 7 ns for the triplet excited state T_1 gives a yield of 0.85 for the yield of $S_1 \rightarrow T_1$ intersystem crossing. Together with the $S_1 \rightarrow S_0$ fluorescence yield of 0.029 (Table 2), a yield of $S_1 \rightarrow S_0$ internal conversion of $1 - 0.85 - 0.029 = 0.12$ is obtained. These results afford a rate constant of $(4.2 \text{ ns})^{-1}$ for $S_1 \rightarrow S_0$ internal conversion.
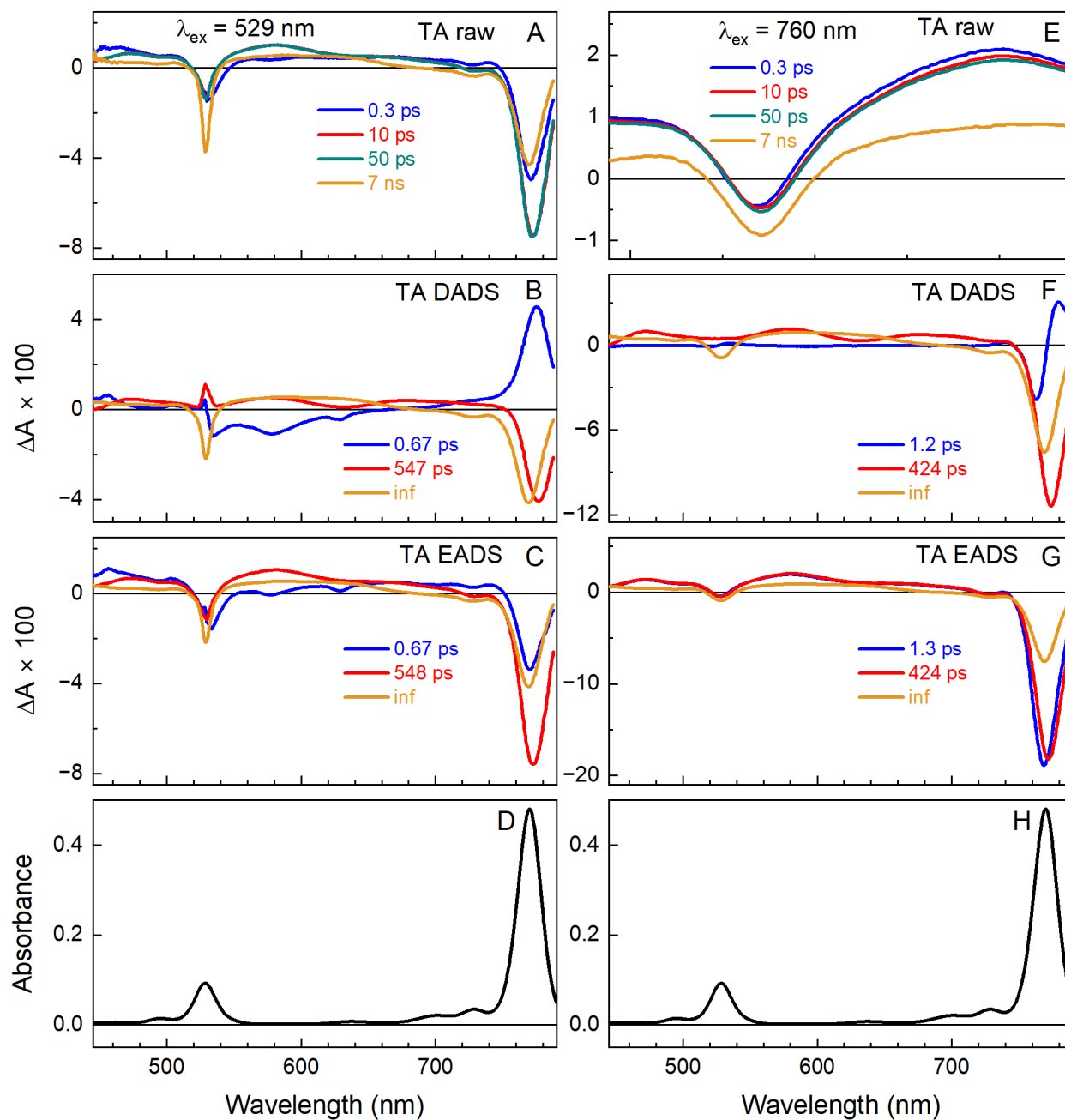
Figure S11. Representative TA spectra for **BrNp-BC** in toluene using excitation at 529 nm (a) or 760 nm (E). Decay associated difference spectra from global fitting of the TA data using excitation at 529 nm (B) or 760 nm (F). Evolution associated difference spectra from global fitting of the TA data using excitation at 529 nm (C) or 760 nm (G). Panels D and H give the ground-state absorption spectrum. The sharp features at 529 nm in A–C result from scattered excitation light.
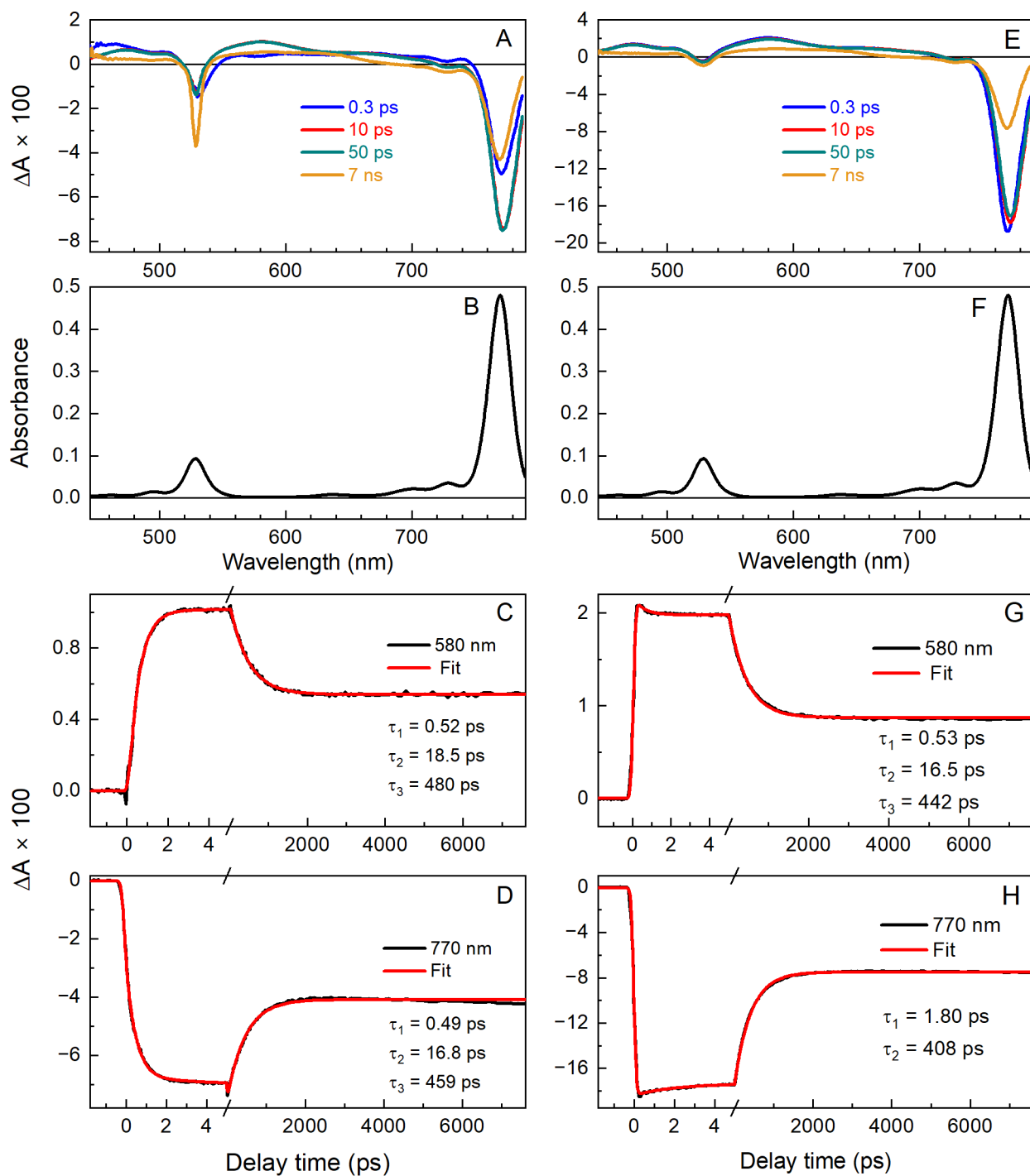
Figure S12. Representative TA data for for **BrNp-BC** in toluene using excitation at 529 nm (left) or 760 nm (right). Panels A and E show TA spectra at specific times. Panels B and F give the ground state absorption spectrum. Panels C, D, G, and H give kinetic profiles and fits at specific wavelengths.

Section S7

Molecular Orbital Characteristics
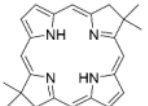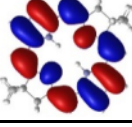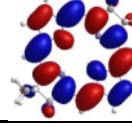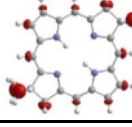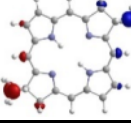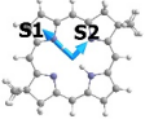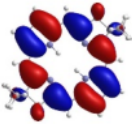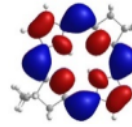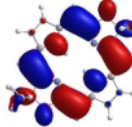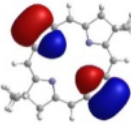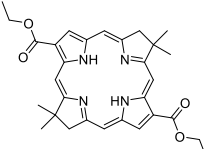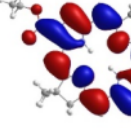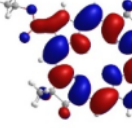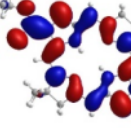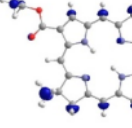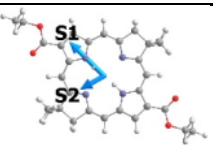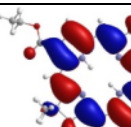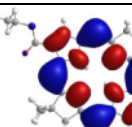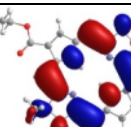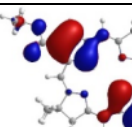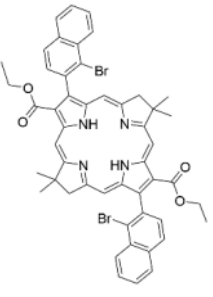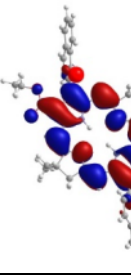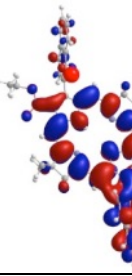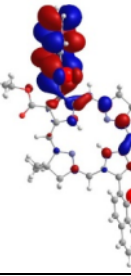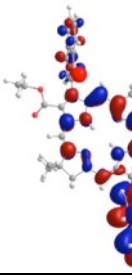
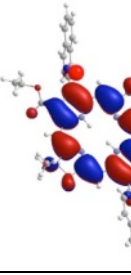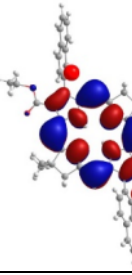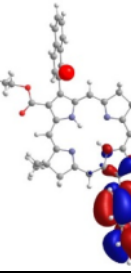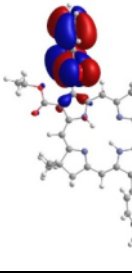| A. H-BC	MOs			
	LUMO, −1.38 eV	LUMO+1, +0.19 eV	LUMO+2, +1.08 eV	LUMO+3, +1.19 eV
$\theta_{12} = 90°$	HOMO, −6.11 eV	HOMO-1, −6.89 eV	HOMO-2, −9.05 eV	HOMO-3, −9.35 eV
B. Es-BC	MOs			
	LUMO, −1.87 eV	LUMO+1, −0.06 eV	LUMO+2, +0.75 eV	LUMO+3, +1.08 eV
$\theta_{12} = 73°$	HOMO, −6.39 eV	HOMO-1, −7.07 eV	HOMO-2, −9.19 eV	HOMO-3, −9.61 eV
C. BrNp-BC	MOs			
	LUMO, −1.91 eV	LUMO+1, −0.12 eV	LUMO+2, +0.09 eV	LUMO+3, +0.09 eV
$\theta_{12} = 89°$	HOMO, −6.39 eV	HOMO-1, −7.06 eV	HOMO-2, −8.09 eV	HOMO-3, −8.13 eV

Figure S13. Comparison of MO characteristics of **H-BC**, **Es-BC**, **BrNp-BC**, **Phen-BC**, **Benz-BC**, and **Phen^{2,1}-BC**. At lower left are the TDM vectors for the $S_0 \rightarrow S_1$ and $S_0 \rightarrow S_2$ transitions and the angle between them obtained from TDDFT calculations.

(Continued on next page)

D. Phen-BC	MOs			
	LUMO, −2.23 eV	LUMO+1, −0.27 eV	LUMO+2, −0.25 eV	LUMO+3, +0.69 eV
θ₁₂ = 55°	HOMO, −5.99 eV	HOMO-1, −6.81 eV	HOMO-2, −7.78 eV	HOMO-3, −8.45 eV

E. Benz-BC	MOs			
	LUMO, −2.35 eV	LUMO+1, −0.32 eV	LUMO+2, +0.02 eV	LUMO+3, +1.02 eV
θ₁₂ = 46°	HOMO, −6.36 eV	HOMO-1, −6.96 eV	HOMO-2, −7.97 eV	HOMO-3, −8.44 eV

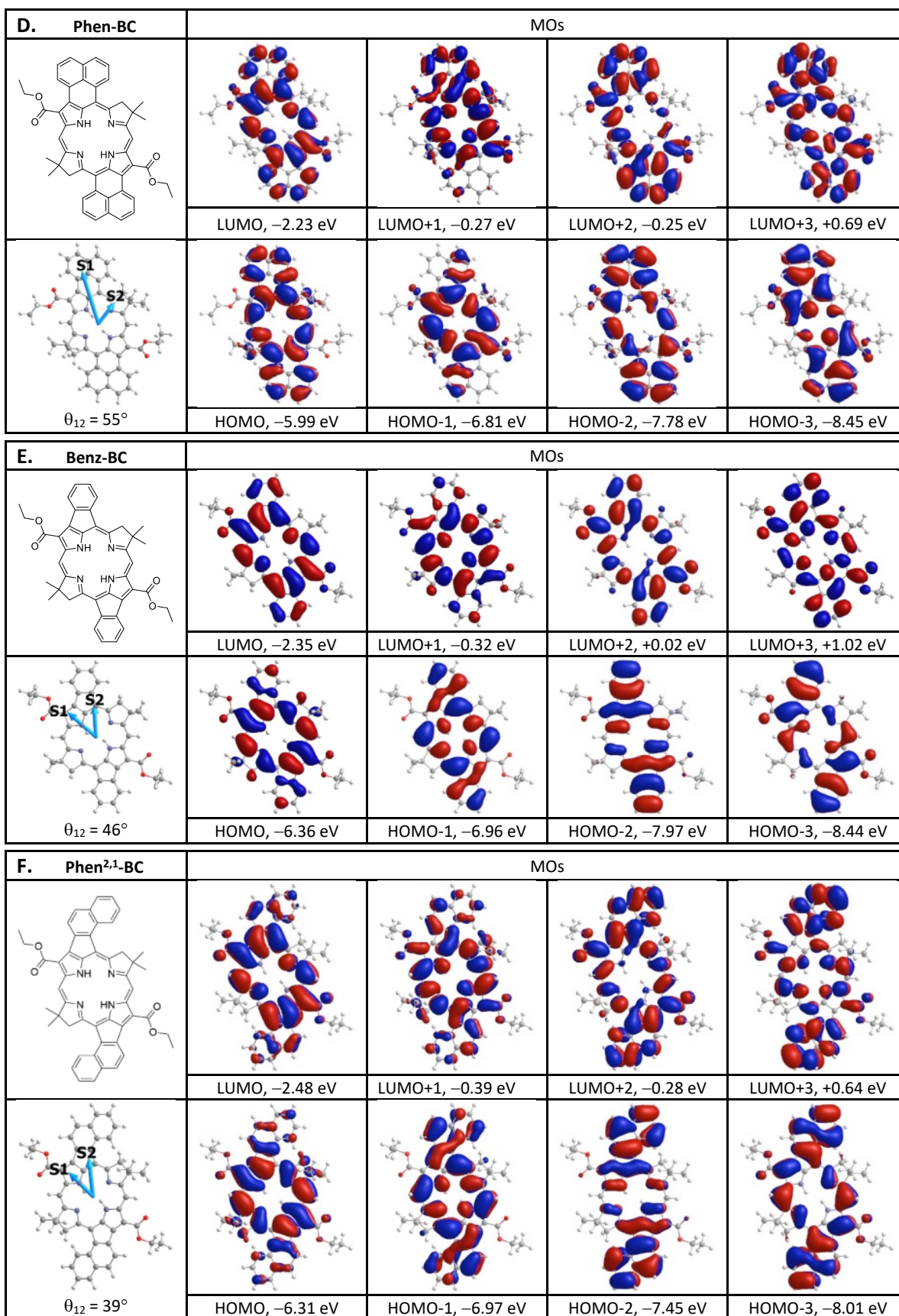| F. Phen²,¹-BC	MOs			
	LUMO, −2.48 eV	LUMO+1, −0.39 eV	LUMO+2, −0.28 eV	LUMO+3, +0.64 eV
θ₁₂ = 39°	HOMO, −6.31 eV	HOMO-1, −6.97 eV	HOMO-2, −7.45 eV	HOMO-3, −8.01 eV

Figure S13. (Continued from previous page)

Section S8

Composition of Excited States from TDDFT Calculations

Table S7. TDDFT results for **H-BC** in toluene.[a]

State	λ (nm)	f	filled MO	empty MO	Coefficient[b]	%[c]
S_1	710	0.37	H	L	0.678	92
			H-1	L+1	0.219	6[d]
					-0.127e	
S_2	514	0.11	H-1	L	0.615	76
			H	L+1	-0.348	24
S_3	344	1.58	H	L+1	0.619	77
			H-1	L	0.355	22[d]
					-0.119e	
S_4	312	1.32	H-1	L+1	0.674	91
			H-1	L	-0.293	7[d]
					0.132e	

[a]H = HOMO and L = LUMO. Only states in the S_0–S_{10} range and absorption >320 nm and with oscillator strength (f) > 0.01 are listed. [b]Coefficient for the configuration. [c]The percent contribution to the state is obtained by squaring the coefficient. [d]A small contribution from an 'emissive' contribution ("e" after the coefficient) involving the same orbitals was subtracted to obtain the percentage shown.

Table S8. TDDFT results for **Es-BC** in toluene.[a]

State	λ (nm)	f	filled MO	empty MO	Coefficient[b]	%[c]
S_1	764	0.52	H	L	0.964	93
			H-1	L+1	0.283	5[d]
					-0.174e	
S_2	551	0.19	H-1	L	0.918	84
			H	L+1	0.392	15
S_3	351	1.13	H	L+1	0.921	85
			H-1	L	0.402	13[d]
					0.164e	
S_4	322	1.56	H-1	L+1	0.946	90
			H-1	L	0.293	6[d]
					-0.174e	
S_9	278	0.12	H-4	L	0.689	93
			H-3	L+2	0.107	2

[a]H = HOMO and L = LUMO. Only states in the S_0–S_{10} range and absorption >320 nm and with oscillator strength (f) > 0.01 are listed. [b]Coefficient for the configuration. [c]The percent contribution to the state is obtained by squaring the coefficient. [d]A small contribution from an 'emissive' contribution ("e" after the coefficient) involving the same orbitals was subtracted to obtain the percentage shown.

Table S9. TDDFT results for **BrNp-BC** in toluene.[a]

State	λ (nm)	f	filled MO	empty MO	Coefficient[b]	%[c]
S_1	795	0.75	H	L	0.684	93
			H-1	L+1	-0.164	3[d]
					-0.105e	
S_2	559	0.18	H-1	L	0.651	85
			H	L+1	0.235	11
			H	L+3	0.109	2
S_3	355	0.96	H	L+1	0.591	70
			H-1	L	-0.276	13[d]
					0.115e	
			H	L+3	0.238	11
			H	L+2	-0.138	4
S_4	330	1.37	H-1	L+1	0.4722	40
			H-1	L	0.293	30
			H-1	L+3	0.180	6
			H-4	L	0.129	3
			H-1	L+2	-0.110	2
			H	L+3	0.109	2
S_5	325	0.74	H-1	L+1	0.460	42
			H-3	L	0.369	27
			H-1	L+3	0.156	5
			H-4	L	-0.134	4
			H-7	L	-0.120	3
			H-3	L	-0.118	3
			H	L	0.116	3
			H-6	L	-0.224	3

[a]H = HOMO and L = LUMO. Only states in the S_0–S_{10} range and absorption >320 nm and with oscillator strength (f) > 0.01 are listed. [b]Coefficient for the configuration. [c]The percent contribution to the state is obtained by squaring the coefficient. [d]A small contribution from an 'emissive' contribution ("e" after the coefficient) involving the same orbitals was subtracted to obtain the percentage shown.

Table S10. TDDFT results for **Phen-BC** in toluene.[a]

State	λ (nm)	f	filled MO	empty MO	Coefficient[b]	%[c]
S_1	979	1.1	H	L	0.956	91
			H-1	L	0.203	4
			H-1	L+1	-0.158	3
S_2	683	0.31	H-1	L	0.911	83
			H	L+1	0.304	10
			H	L	-0.213	5
S_3	417	0.07	H-2	L	0.900	80
			H	L+2	0.342	12
S_4	407	0.53	H	L+1	0.891	81
			H-1	L	-0.327	11
			H	L+2	-0.192	2
S_6	376	0.90	H-3	L	0.717	51
			H-1	L+1	0.537	29
			H	L+3	0.229	5
			H-2	L+2	0.183	3
			H	L+1	0.151	2
S_8	352	0.78	H-1	L+2	0.697	49
			H-8	L	-0.546	30
			H-4	L	-0.261	7
			H-6	L	-0.160	3
			H-1	L+1	0.154	2

[a]H = HOMO and L = LUMO. Only states in the S_0–S_{10} range and absorption >320 nm and with oscillator strength (f) > 0.01 are listed. [b]Coefficient for the configuration. [c]The percent contribution to the state is obtained by squaring the coefficient.

Table S11. TDDFT results for **Benz-BC** in toluene.[a]

State	λ (nm)	f	filled MO	empty MO	Coefficient[b]	%[c]
S_1	1056	0.39	H	L	0.962	93
			H-1	L	0.148	2
			H-1	L+1	0.218	2[d]
					0.162e	
S_2	703	0.41	H-1	L	0.948	90
			H	L+1	-0.247	6
			H	L	-0.142	2
S_4	416	0.23	H	L+1	0.767	58
			H-3	L	0.580	34
			H-2	L+2	-0.155	2
S_5	371	1.4	H-3	L	0.659	43
			H	L+1	-0.524	27
			H-1	L+1	-0.434	19
			H-1	L	-0.233	5
S_7	339	1.4	H-1	L+1	0.843	71
			H-3	L	0.372	14
			H	L+1	-0.230	5
			H	L	-0.223	3[d]
					-0.148e	

[a]H = HOMO and L = LUMO. Only states in the S_0–S_{10} range and absorption >320 nm and with oscillator strength (f) > 0.01 are listed. [b]Coefficient for the configuration. [c]The percent contribution to the state is obtained by squaring the coefficient. [d]A small contribution from an 'emissive' contribution ("e" after the coefficient) involving the same orbitals was subtracted to obtain the percentage shown.

Table S12. TDDFT results for **Phen^{2,1}-BC** in toluene.[a]

State	λ (nm)	f	filled MO	empty MO	Coefficient[b]	%[c]
S$_1$	1277	0.23	H	L	0.971	94
			H-1	L+1	0.170	1[d]
					0.143e	
S$_2$	745	0.53	H-1	L	0.953	91
			H	L+1	-0.218	5
S$_4$	455	0.26	H-3	L	0.704	50
			L	L+1	-0.620	38
			H-2	L+2	-0.186	3
S$_5$	394	1.72	H	L+1	-0.698	49
			H-3	L	0.573	33
			H-1	L+1	-0.267	7
			H-1	L	0.196	4
			H-5	L	0.173	3
S$_8$	351	0.17	H-5	L	0.741	55
			H-1	L+1	-0.392	15
			H-3	L	-0.286	8
			H-4	L+2	0.250	6
			H	L+1	-0.179	3
S$_9$	342	0.77	H-1	L+1	0.778	60
			H-5	L	0.424	18
			H	L	-0.182	3
			H	L+5	0.163	3
			H-3	L	0.148	2

[a]H = HOMO and L = LUMO. Only states in the S$_0$–S$_{10}$ range and absorption >320 nm and with oscillator strength (f) > 0.01 are listed. [b]Coefficient for the configuration. [c]The percent contribution to the state is obtained by squaring the coefficient. [d]A small contribution from an 'emissive' contribution ("e" after the coefficient) involving the same orbitals was subtracted to obtain the percentage shown.

Section S9
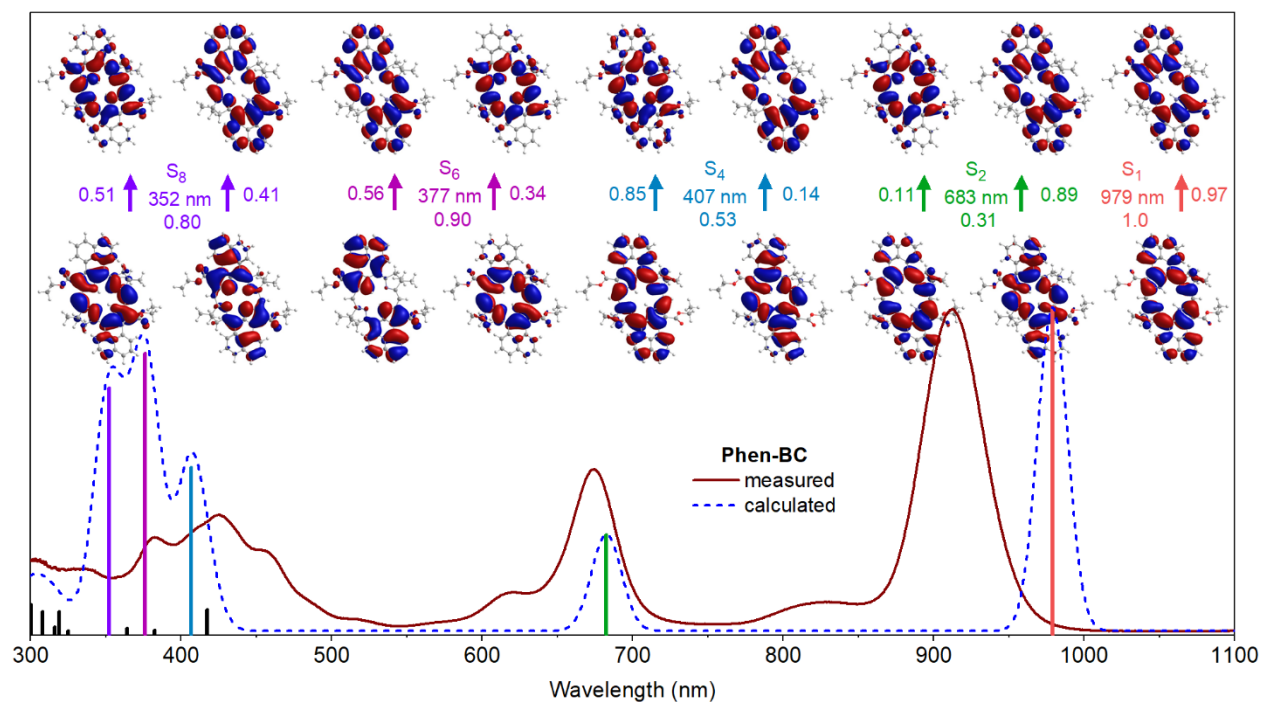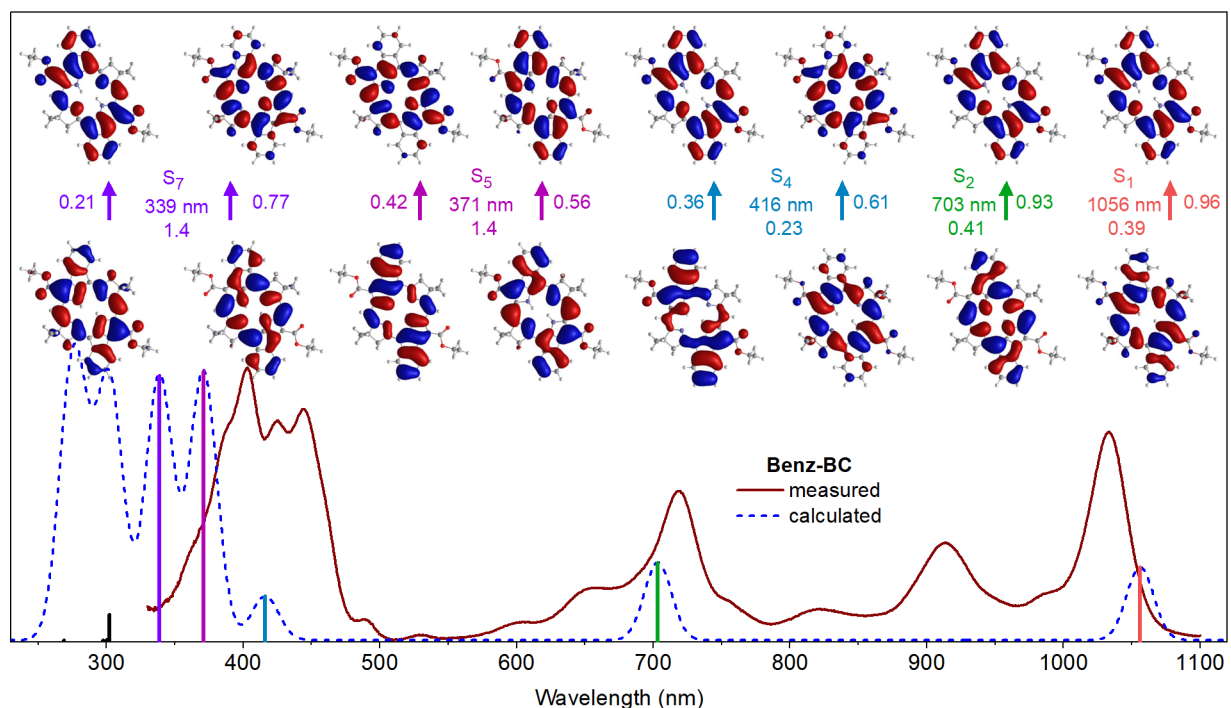
NTOs and
Calculated vs Measured
Absorption Spectra
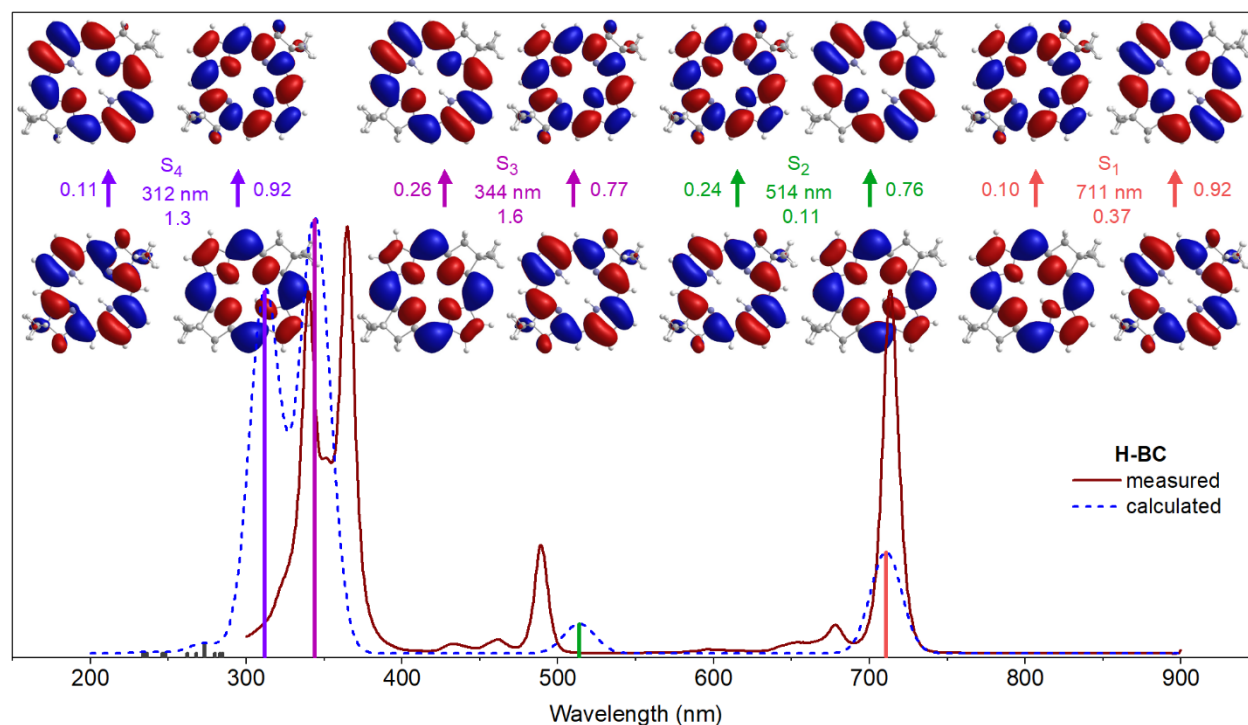
Figure S14. Comparison for **H-BC** of the absorption spectra in toluene that are measured (brown line) or calculated via TDDFT (dashed blue lines and colored sticks) normalized at the highest peak. Calculated spectral features were given 10-nm Gaussian skirts. Shown for the lowest four transitions (S_0 to $S_1 - S_4$) are the natural transition occupied and virtual orbitals (NTOs) along with the wavelength and oscillator strength of the transition obtained from TDDFT. Two NTO promotions contribute to each transition, with weights (eigenvalues) indicated by the values that flank the arrows.
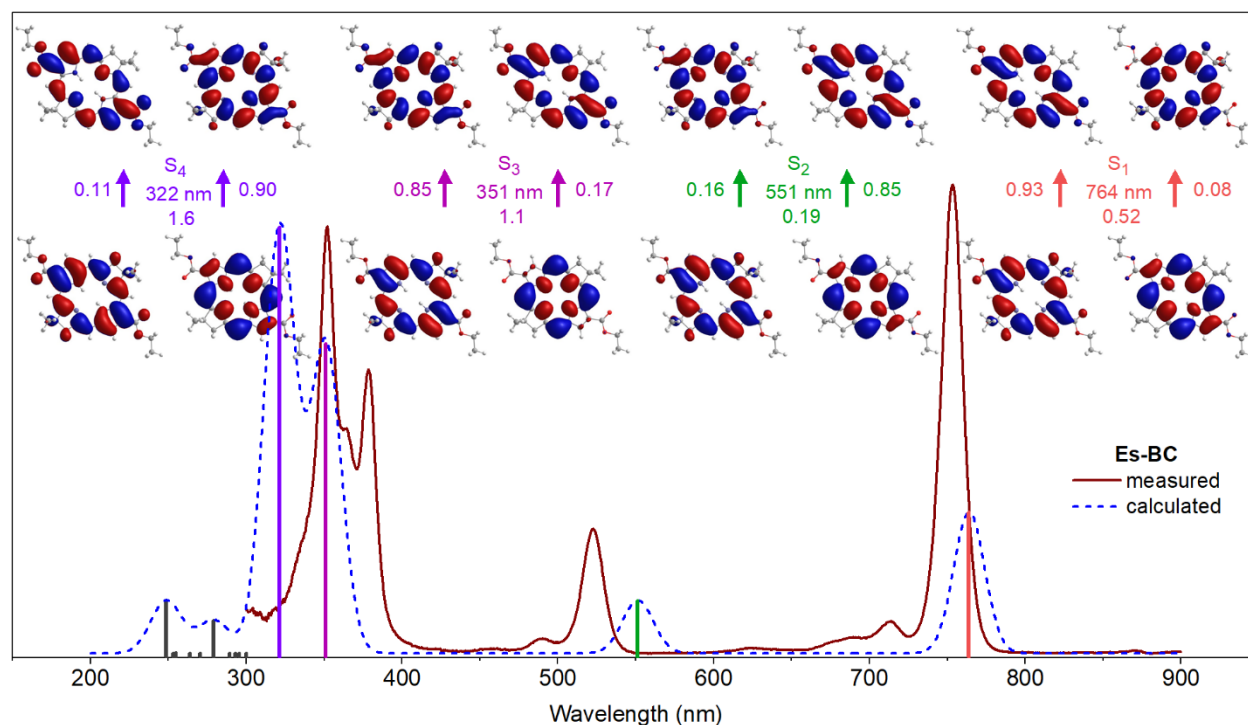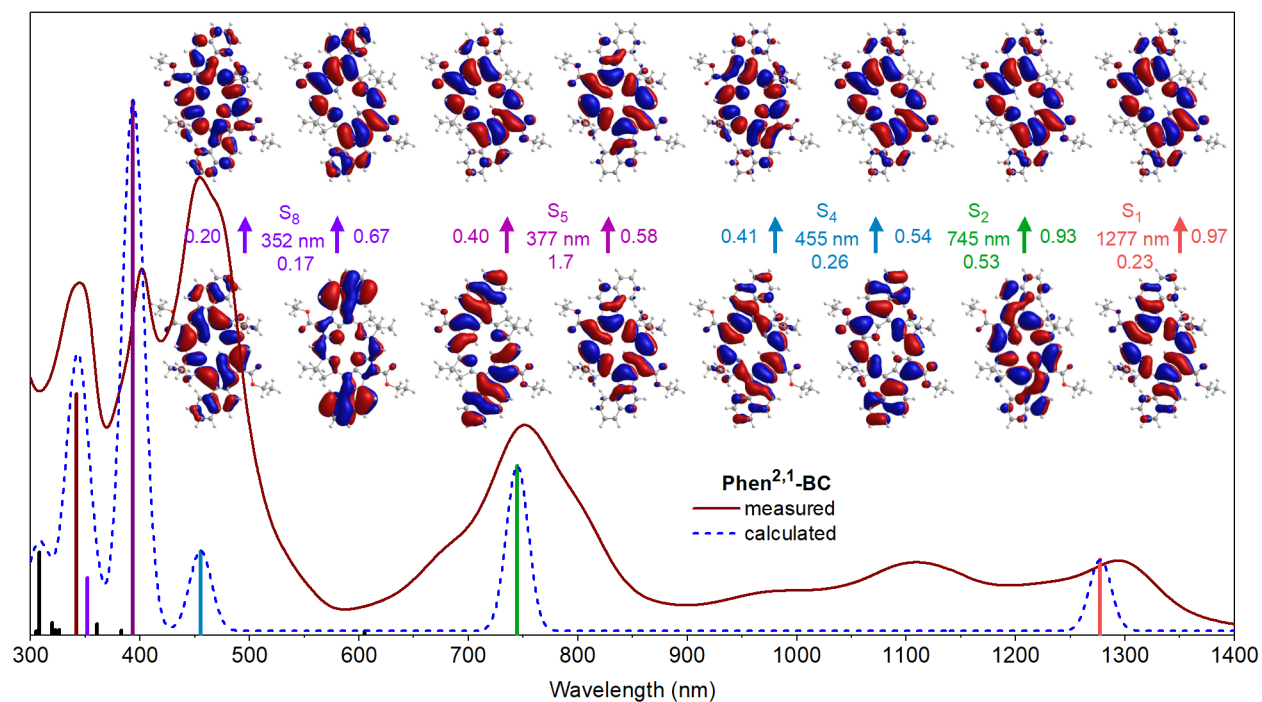
Figure S15. Comparison for **Es-BC** of the absorption spectra in toluene that are measured (brown line) or calculated via TDDFT (dashed blue lines and colored sticks) normalized at the highest peak. Calculated spectral features were given 10-nm Gaussian skirts. Shown for the lowest four transitions (S_0 to $S_1 - S_4$) are the natural transition occupied and virtual orbitals (NTOs) along with the wavelength and oscillator strength of the transition obtained from TDDFT. Two NTO promotions contribute to each transition, with weights (eigenvalues) indicated by the values that flank the arrows.
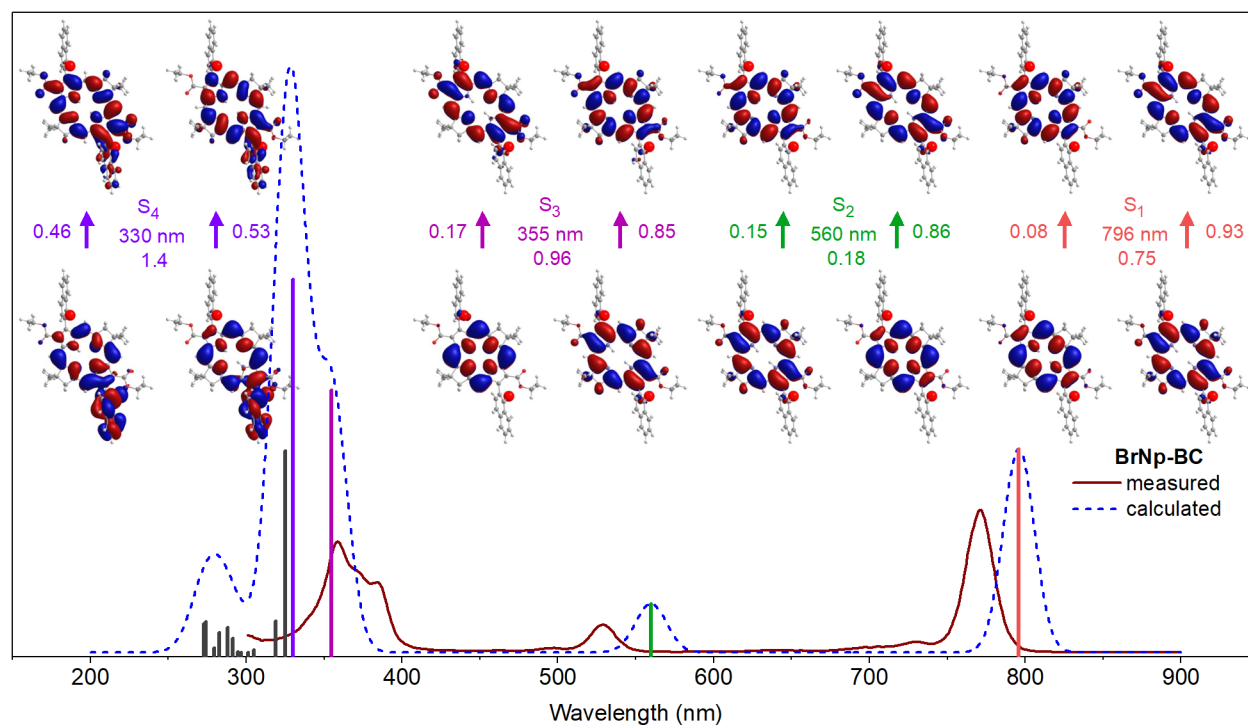
Figure S16. Comparison for **BrNp-BC** of the absorption spectra in toluene that are measured (brown line) or calculated via TDDFT (dashed blue lines and colored sticks) normalized at the highest peak. Calculated spectral features were given 10-nm Gaussian skirts, except for $S_0 \rightarrow S_1$ and $S_0 \rightarrow S_2$, which were set at 20 nm. Shown for the lowest four transitions (S_0 to $S_1 - S_4$) are the natural transition occupied and virtual orbitals (NTOs) along with the wavelength and oscillator strength of the transition obtained from TDDFT. Two NTO promotions contribute to some transitions, with weights (eigenvalues) indicated by the values that flank the arrows.

Figure S17. Comparison for **Phen-BC** of the absorption spectra in toluene that are measured (brown line) or calculated via TDDFT (dashed blue lines and colored sticks) normalized at the highest peak. Calculated spectral features were given 10-nm Gaussian skirts, except for $S_0 \rightarrow S_1$ and $S_0 \rightarrow S_2$, which were set at 20 nm. Shown for the lowest five transitions) that carry significant oscillator strength (S_0 to S_1, S_2, S_4, S_6, and S_8) are the natural transition occupied and virtual orbitals (NTOs) along with the wavelength and oscillator strength of the transition obtained from TDDFT. Two NTO promotions contribute to some transitions, with weights (eigenvalues) indicated by the values that flank the arrows.

Figure S18. Comparison for **Benz-BC** of the absorption spectra in toluene that are measured (brown line) or calculated via TDDFT (dashed blue lines and colored sticks) normalized at the highest peak. Calculated spectral features were given 10-nm Gaussian skirts. Shown for the lowest five transitions that carry significant oscillator strength (S_0 to S_1, S_2, S_4, S_5, and S_7) are the natural transition occupied and virtual orbitals (NTOs) along with the wavelength and oscillator strength of the transition obtained from TDDFT. Two NTO promotions contribute to some transitions, with weights (eigenvalues) indicated by the values that flank the arrows.

Figure S19. Comparison for **Phen^{2,1}-BC** of the absorption spectra in toluene that are measured (brown line) or calculated via TDDFT (dashed blue lines and colored sticks) normalized at the highest peak. Calculated spectral features were given 10-nm Gaussian skirts. Shown for the lowest five transitions) that carry significant oscillator strength (S_0 to S_1, S_2, S_4, S_5, and S_8) are the natural transition occupied and virtual orbitals (NTOs) along with the wavelength and oscillator strength of the transition obtained from TDDFT. Two NTO promotions contribute to some transitions, with weights (eigenvalues) indicated by the values that flank the arrows.

Section S10

Absorption Spectra Simulated Using the Four-Orbital Model
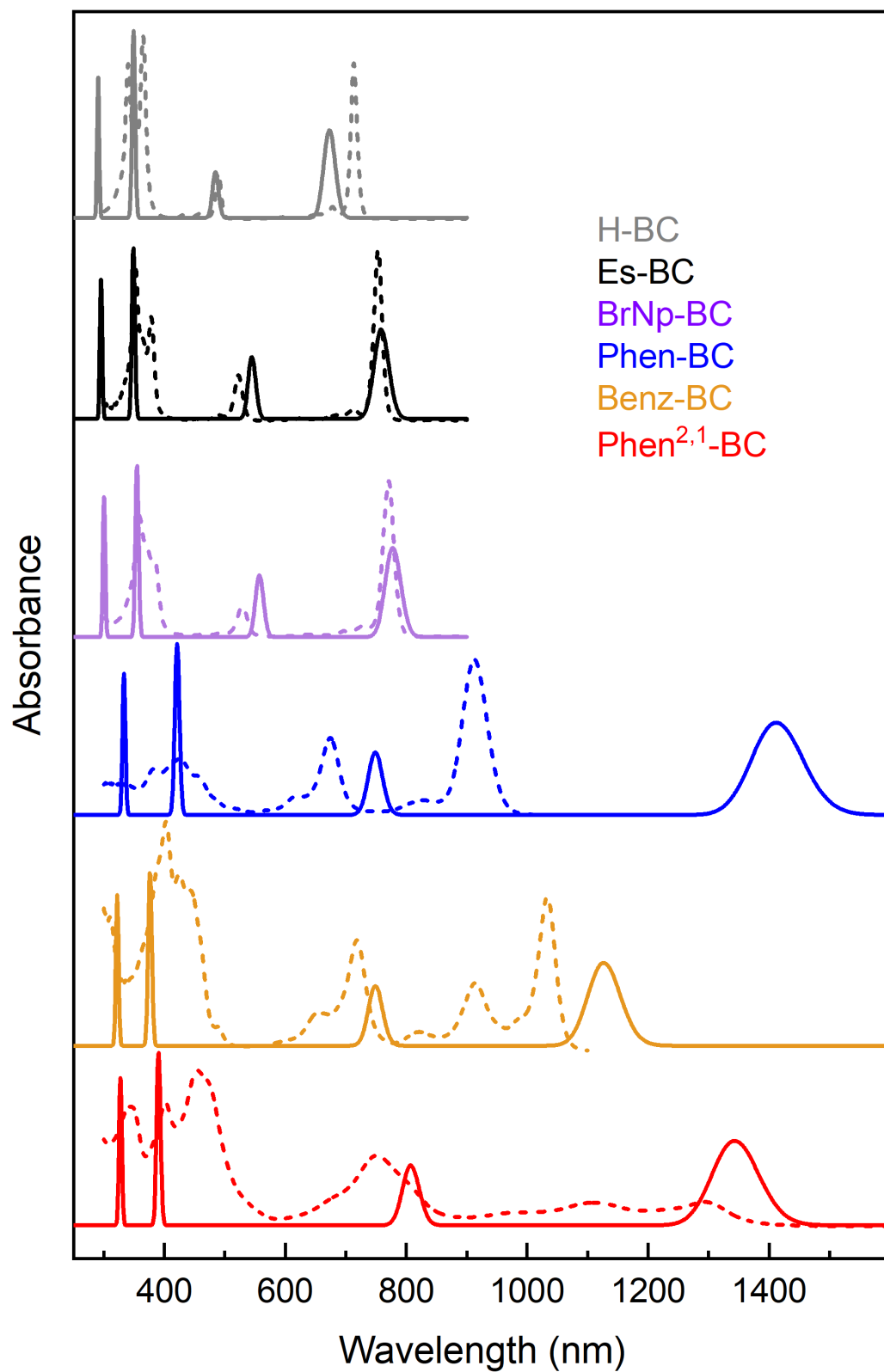
Figure S20. Simulated spectra using the four-orbital model (solid) and measured spectra (dashed) normalized at the largest peak. Each simulated features is represented by a Gaussian with a 500 cm^{-1} FWHM.
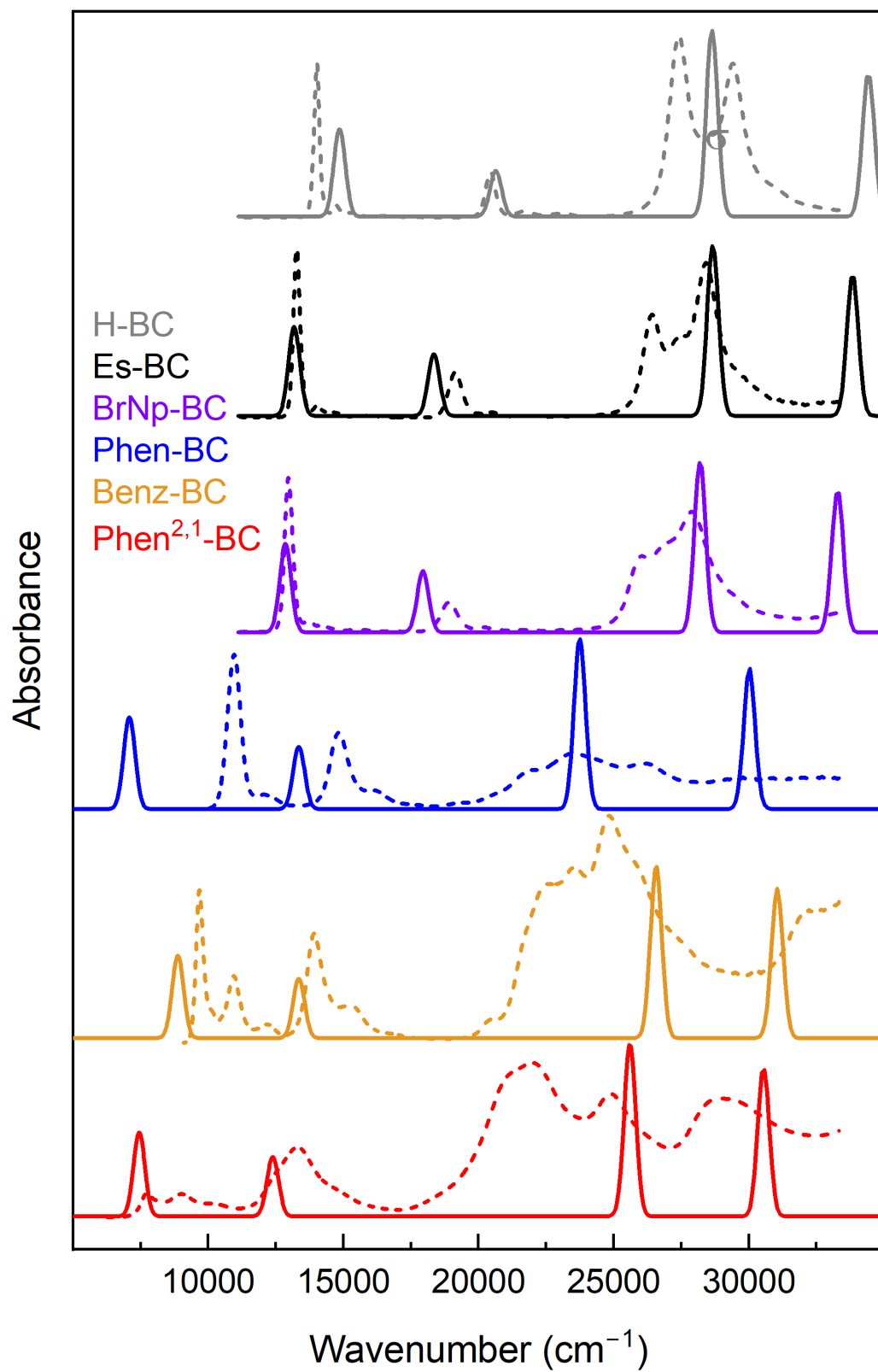
Figure S21. Same simulated (solid) and measured (dashed) spectra as in Figure S20 but plotted versus wavenumber instead of wavelength

Section S11

NMR Spectra
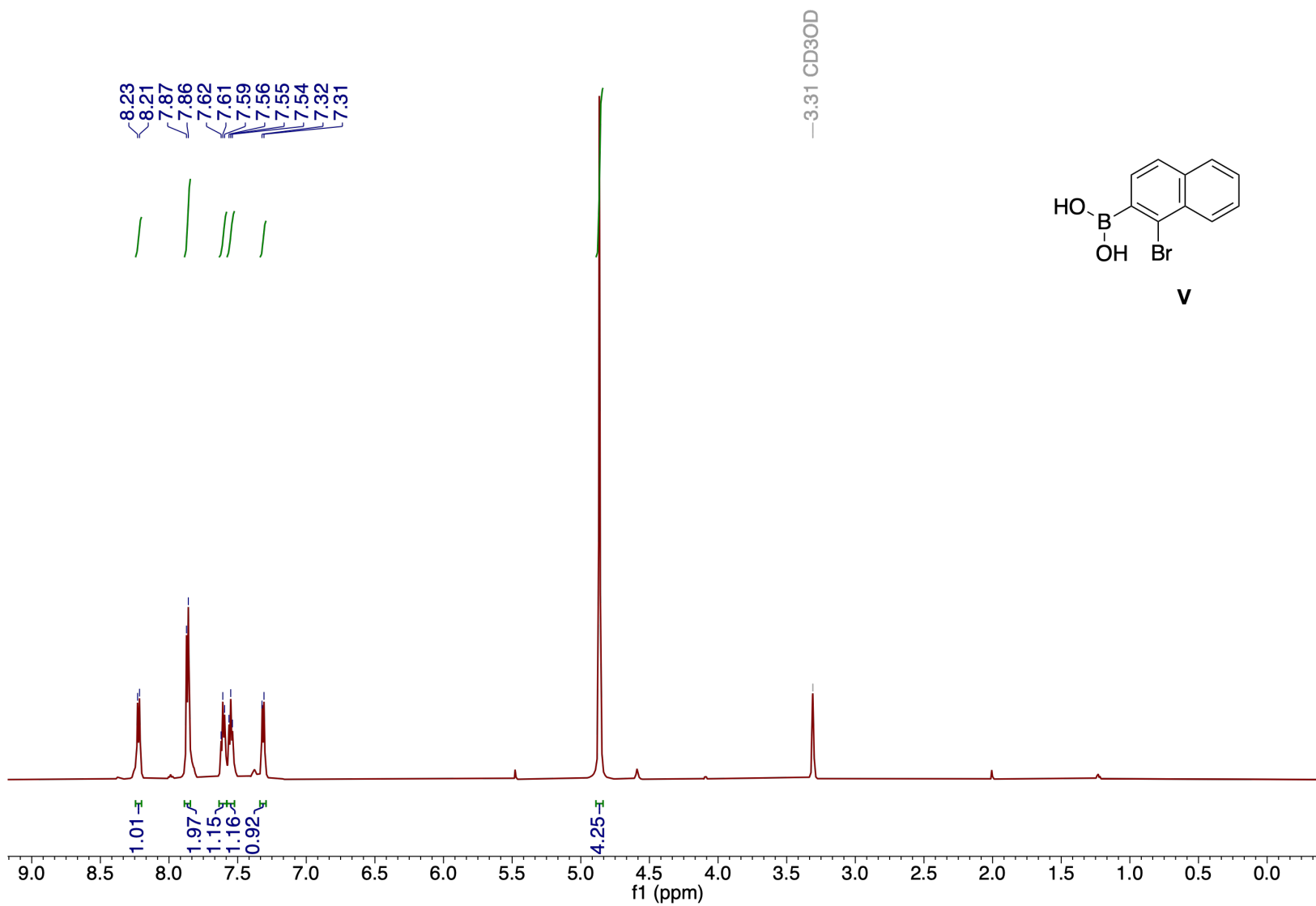
^{1}H NMR spectrum of compound V in CD$_3$OD
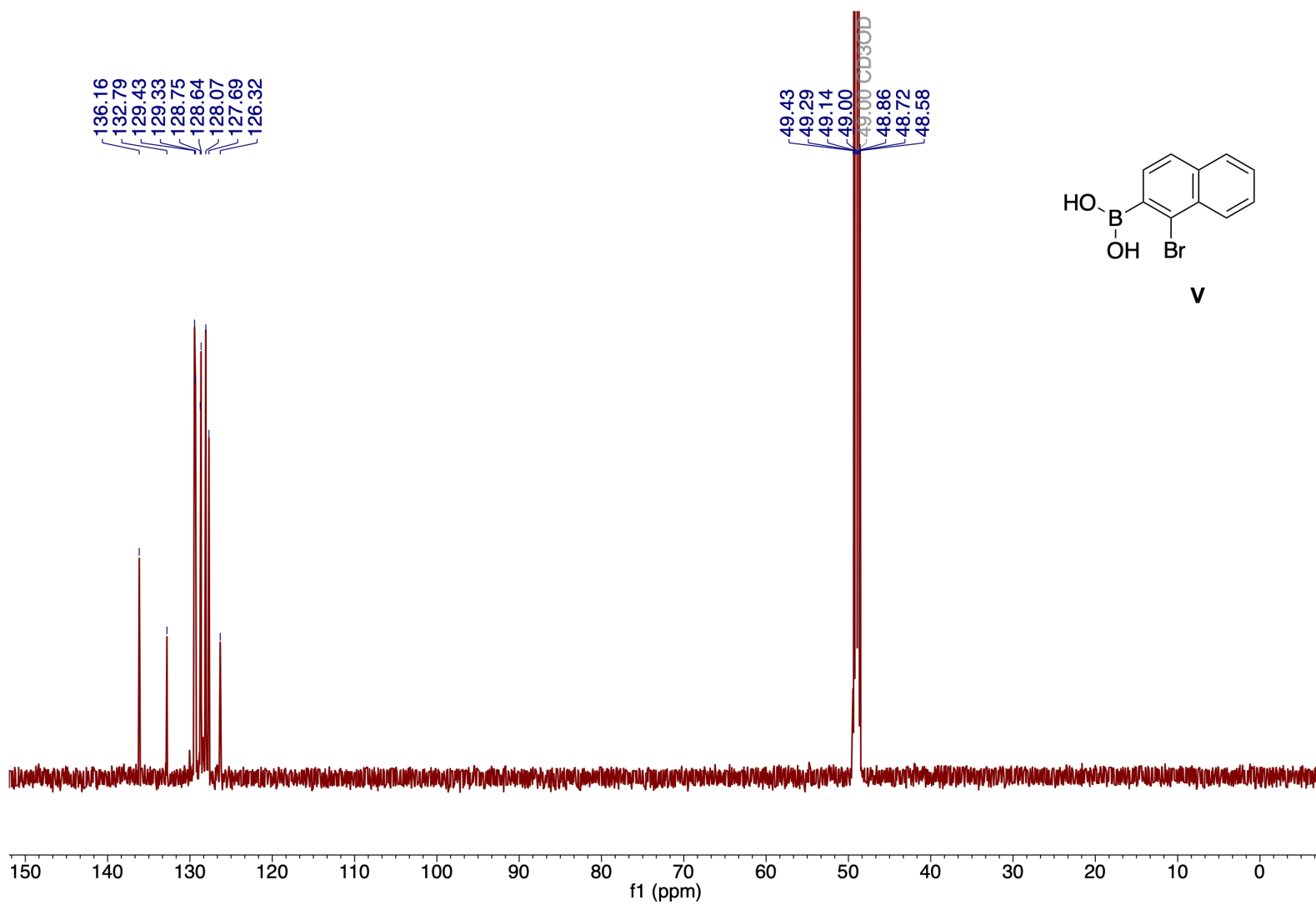
$^{13}C\{^1H\}$ NMR spectrum of compound V in CD$_3$OD
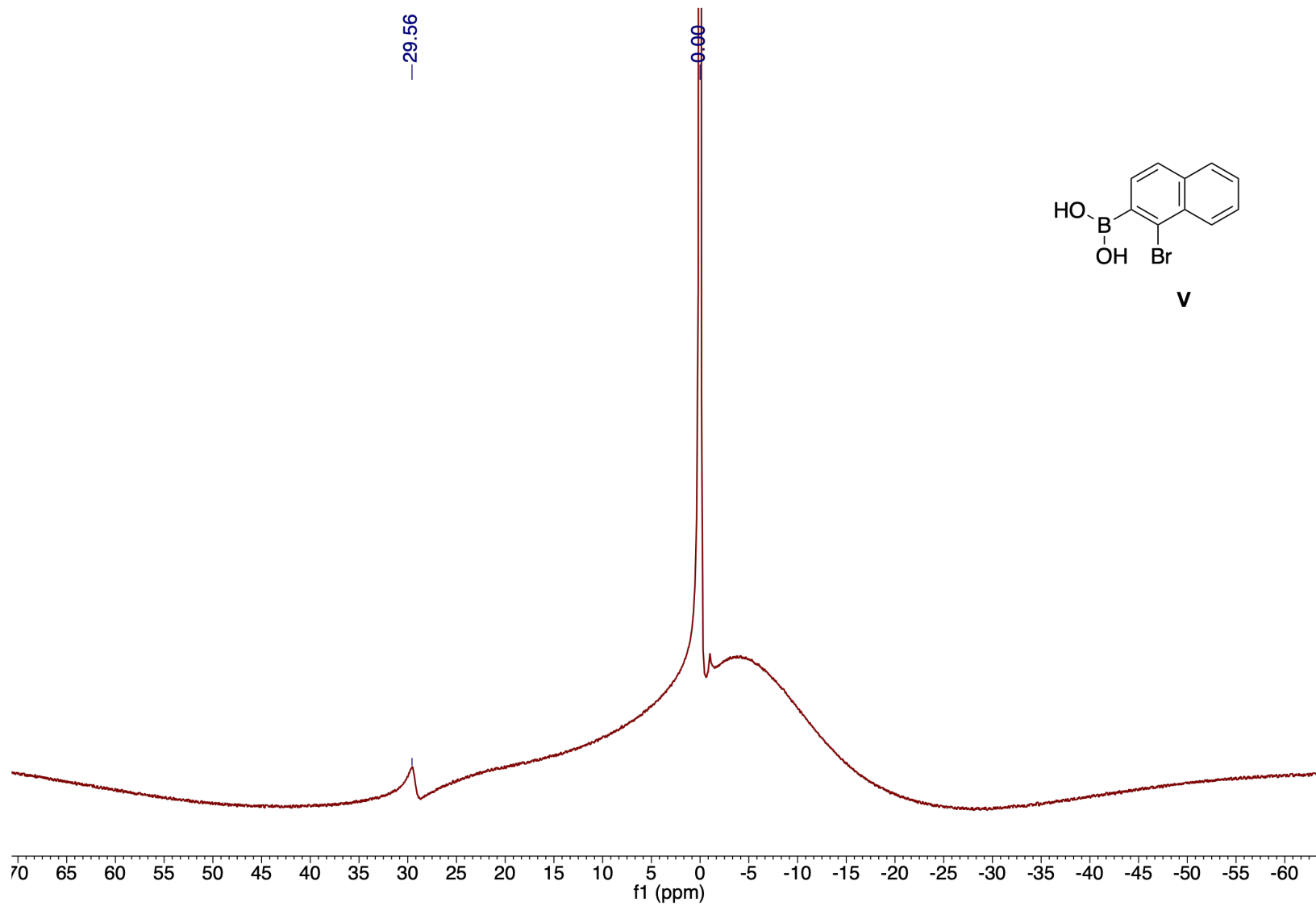
^{10}B NMR spectrum of compound V in CDCl$_3$
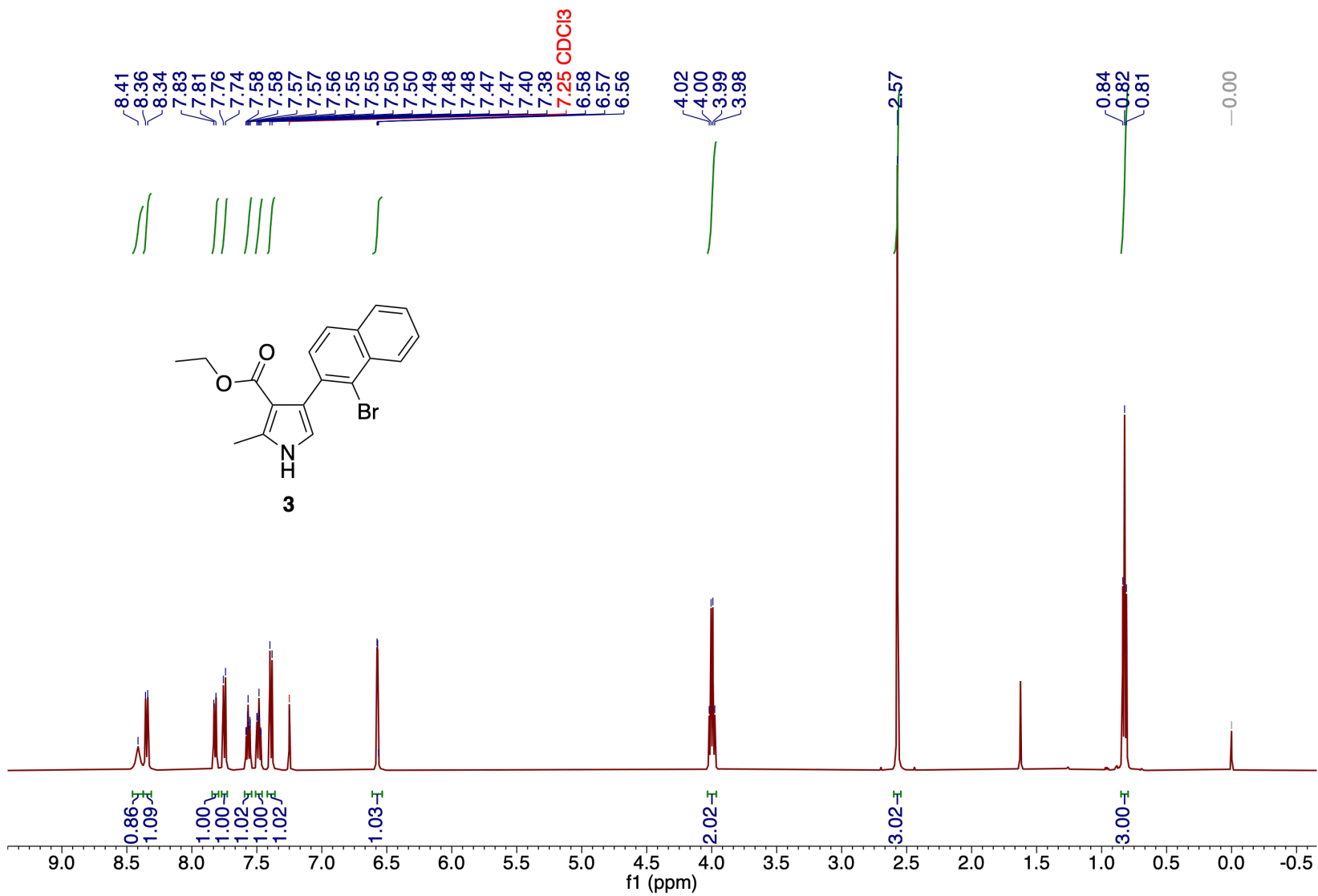
^{1}H NMR spectrum of compound 3
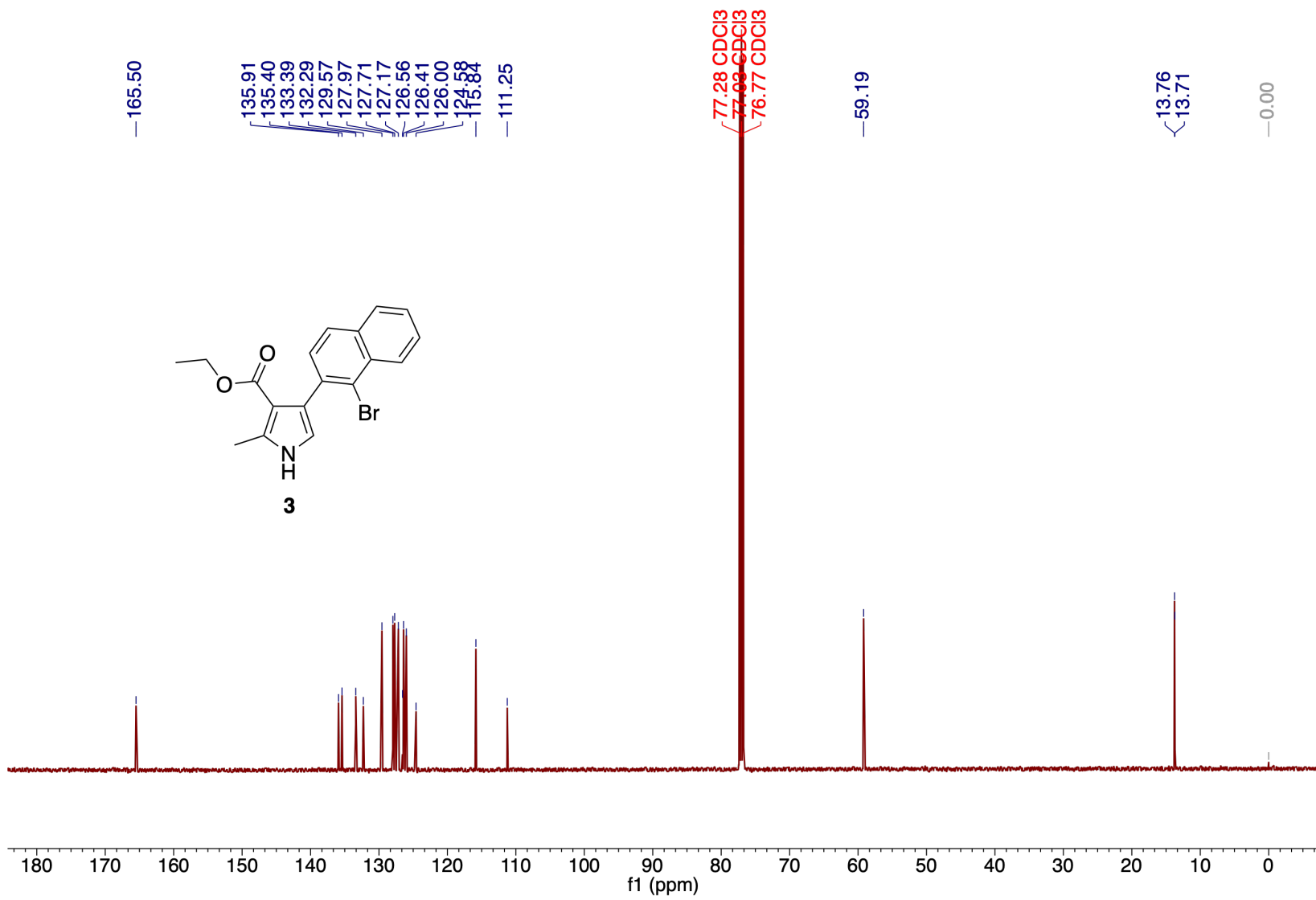
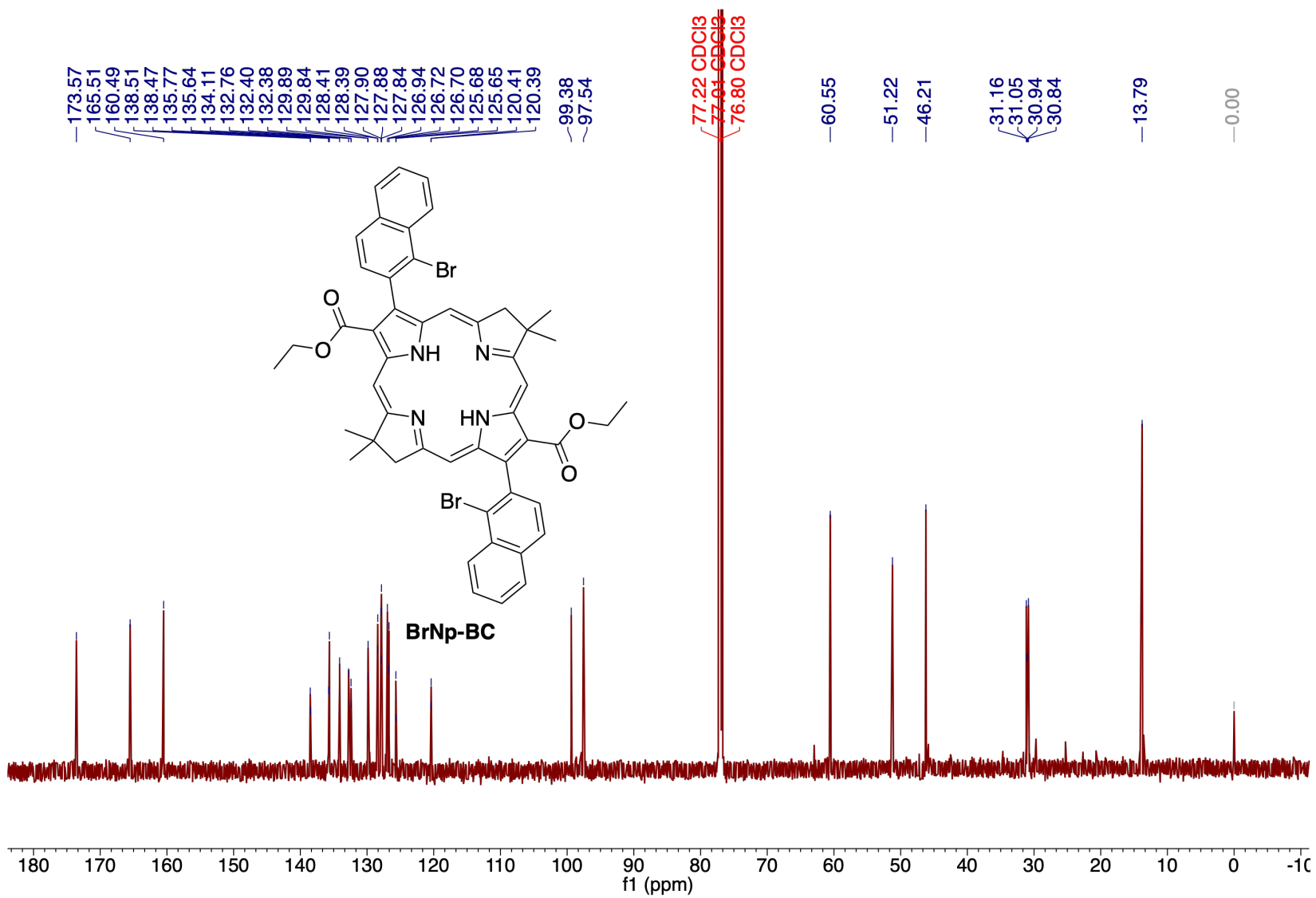$^{13}C\{^1H\}$ NMR spectrum of compound 3

^{1}H NMR spectrum of compound 4
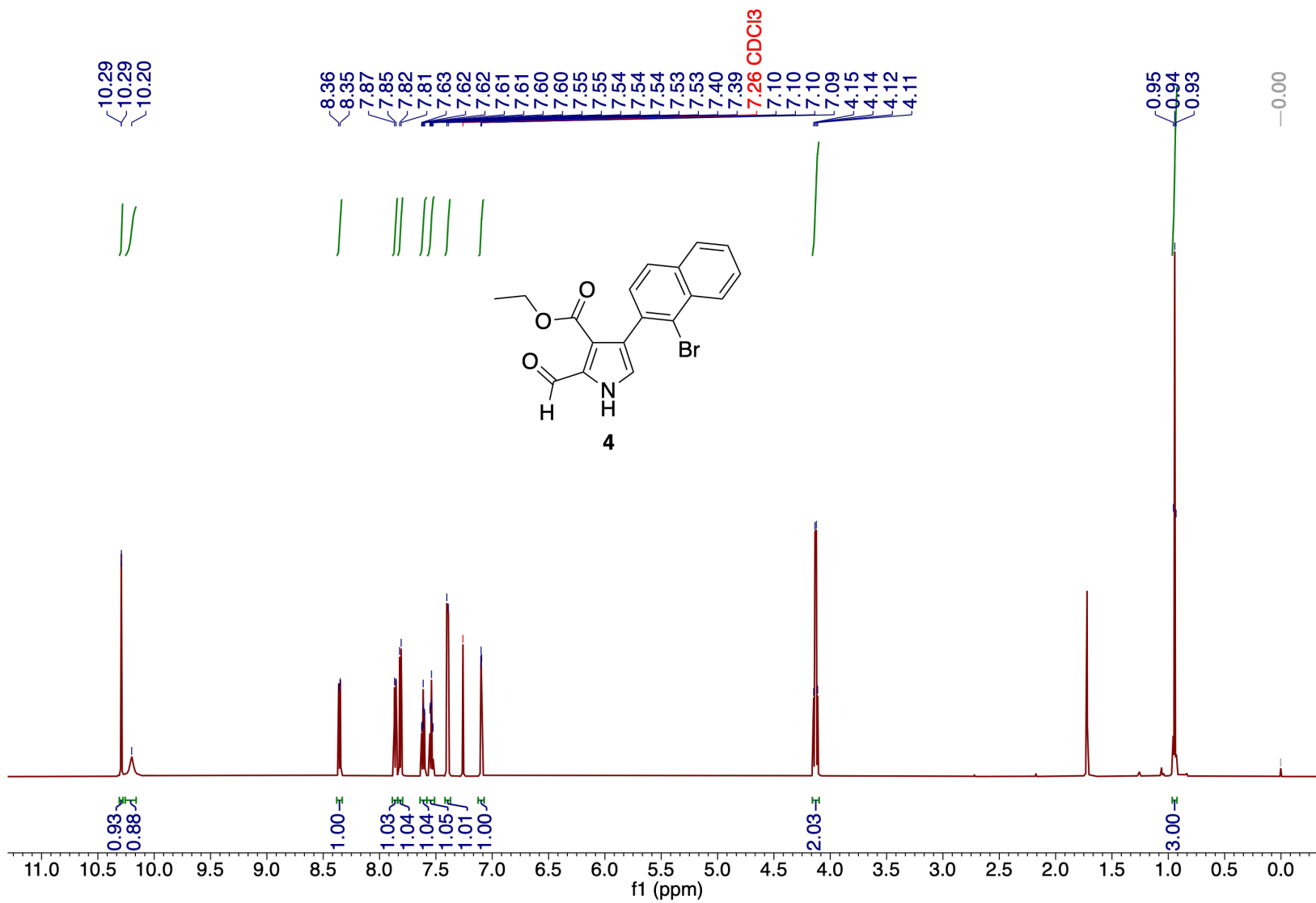
$^{13}C\{^1H\}$ NMR spectrum of compound 4

^{1}H NMR spectrum of compound 5
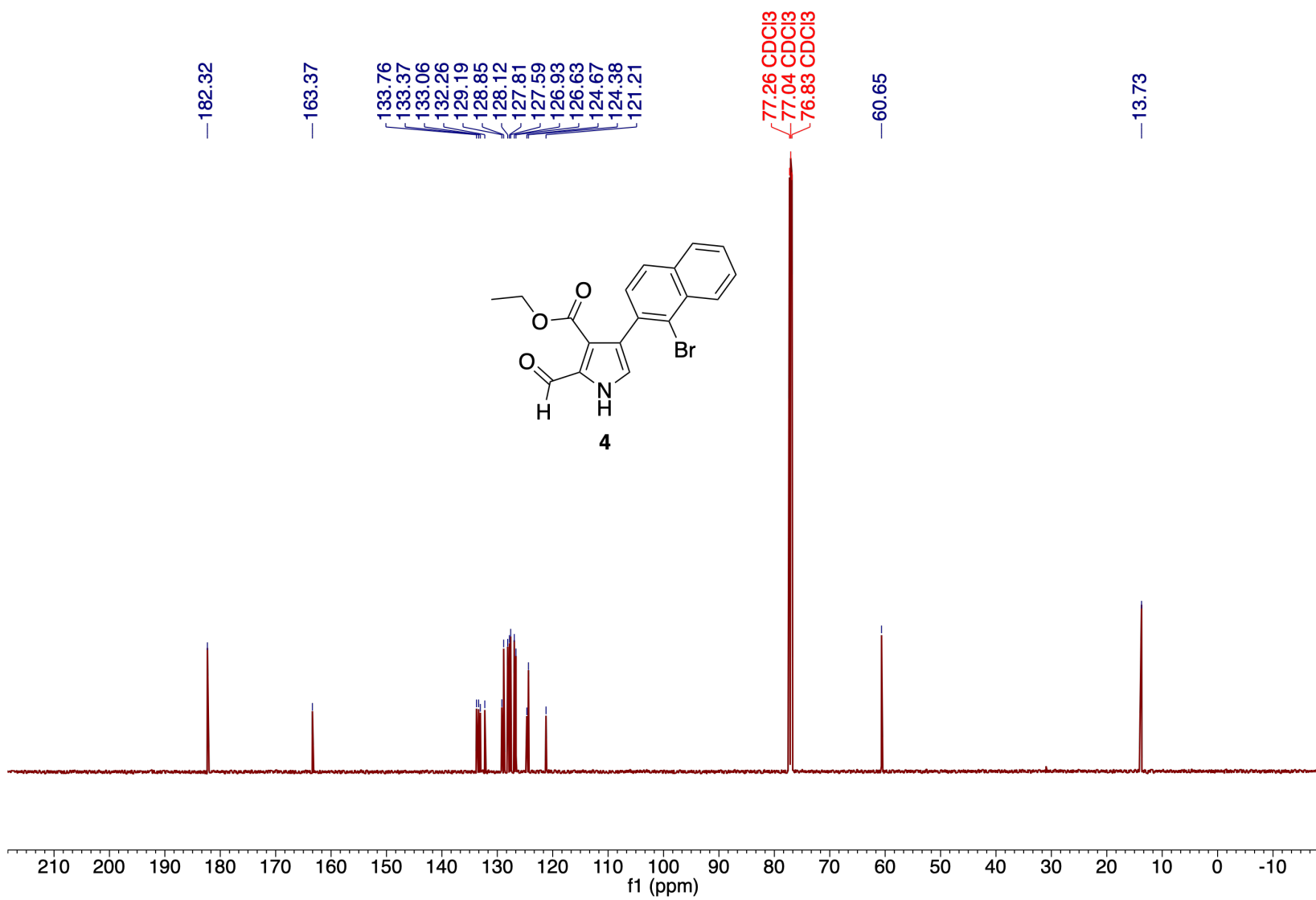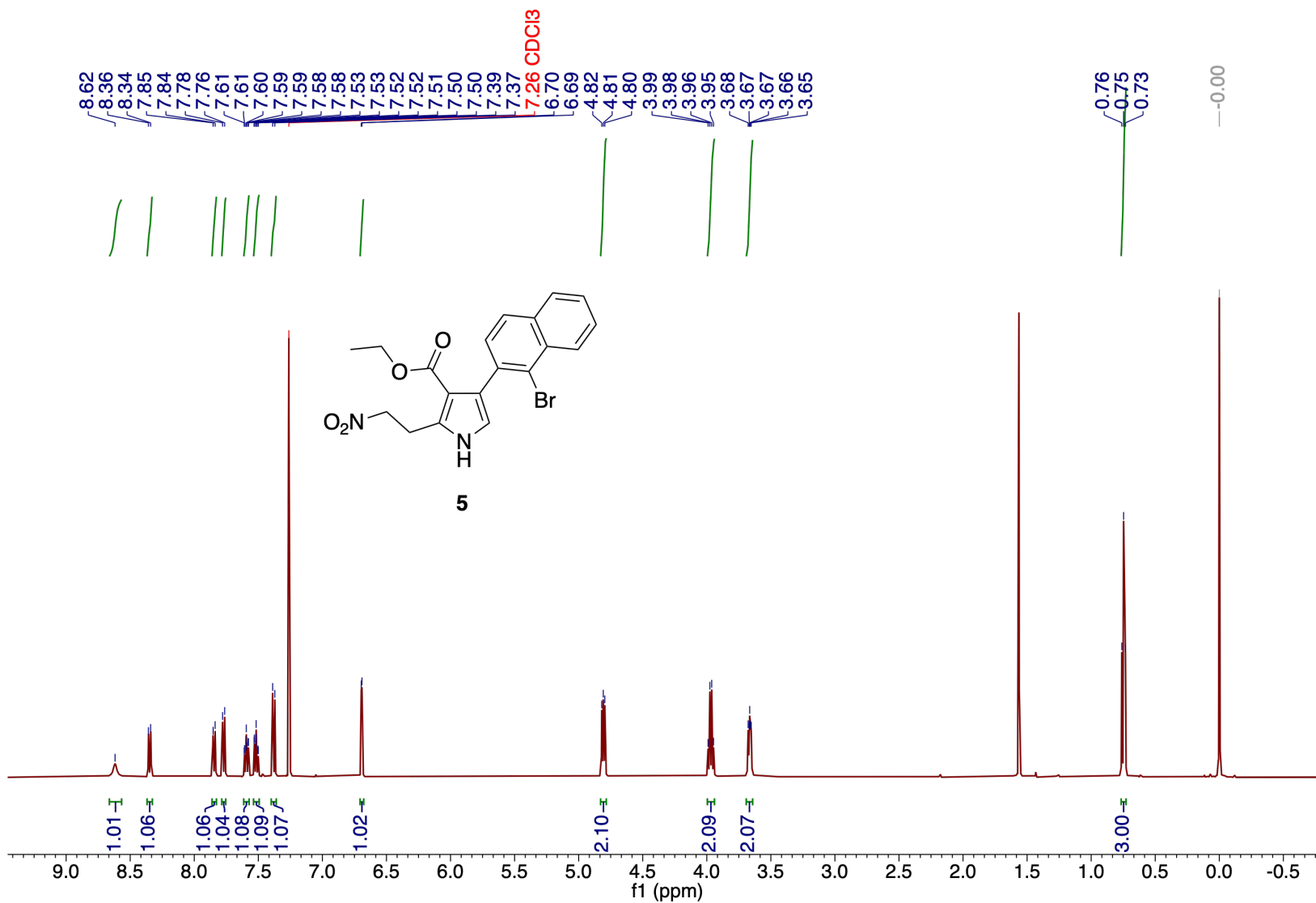
$^{13}C\{^1H\}$ NMR spectrum of compound 5

^{1}H NMR spectrum of compound **6**
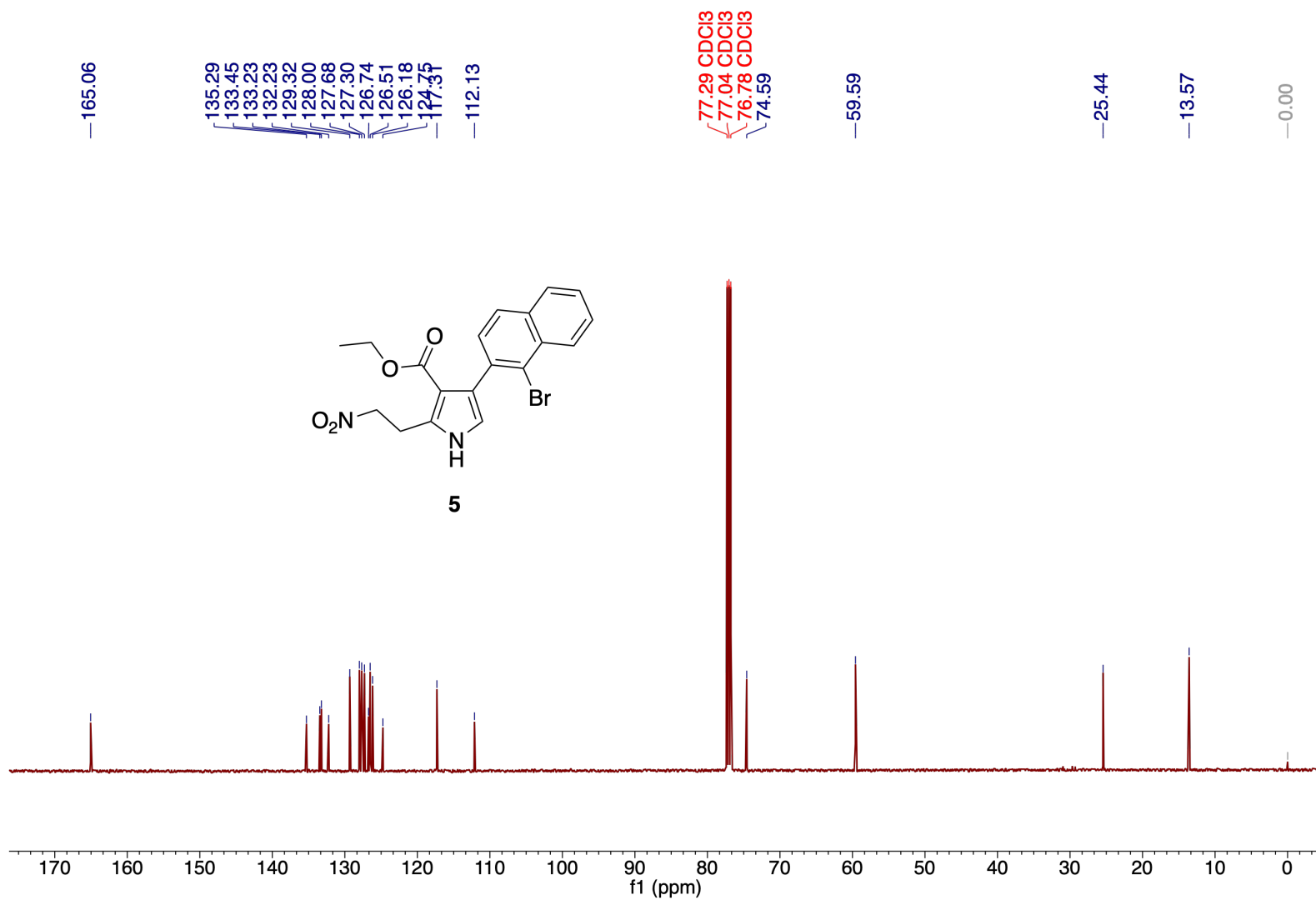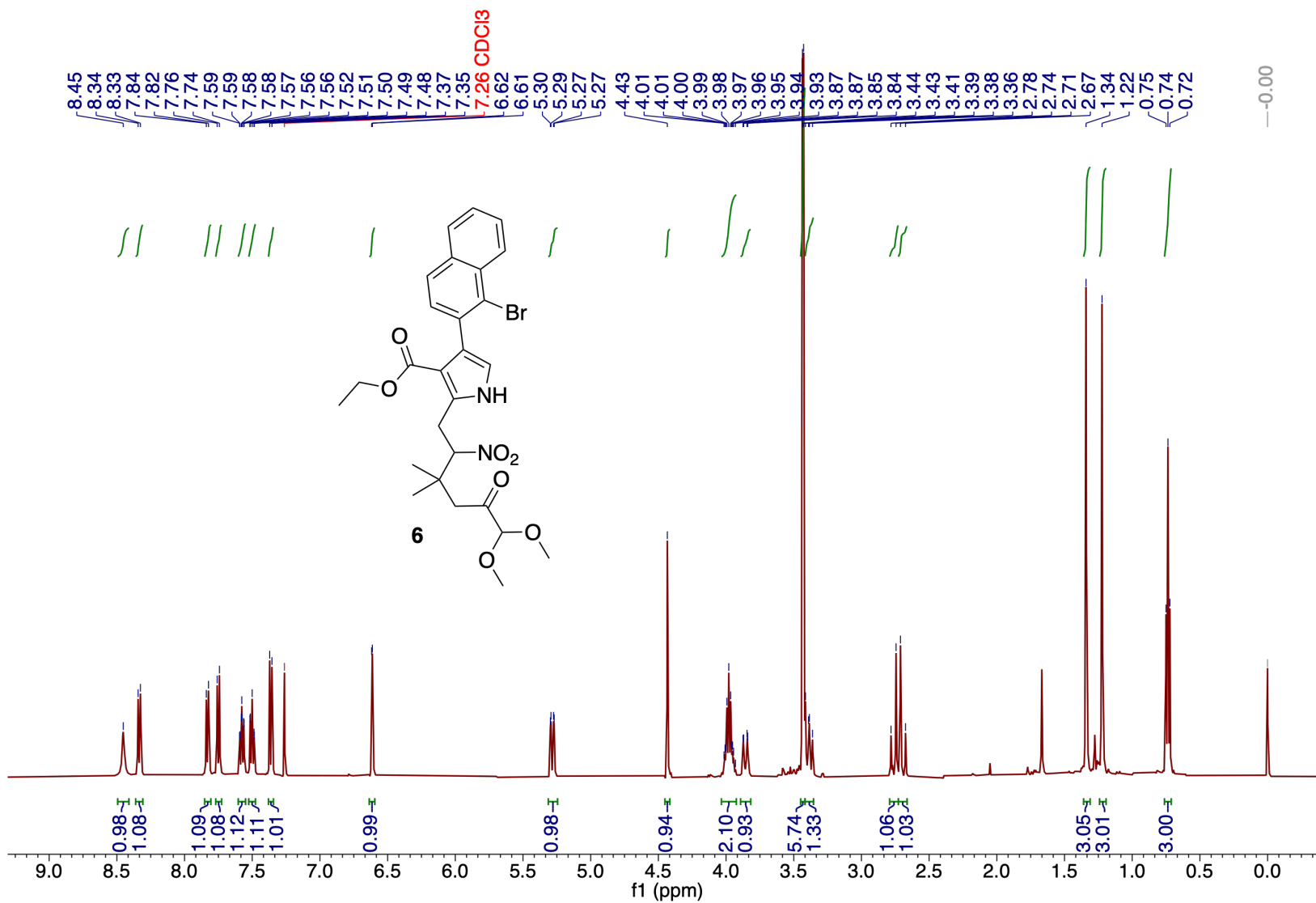
$^{13}C\{^1H\}$ NMR spectrum of compound 6
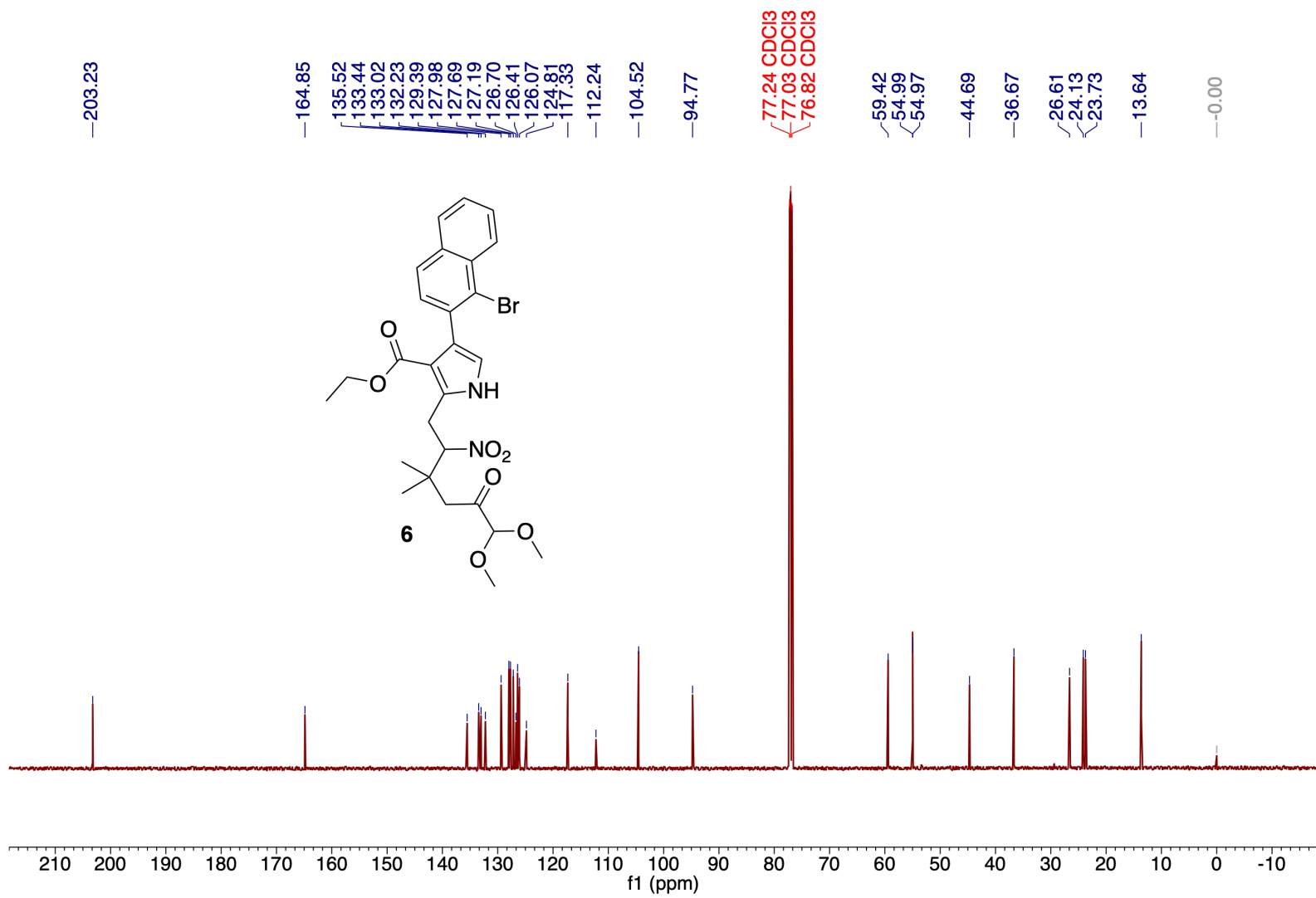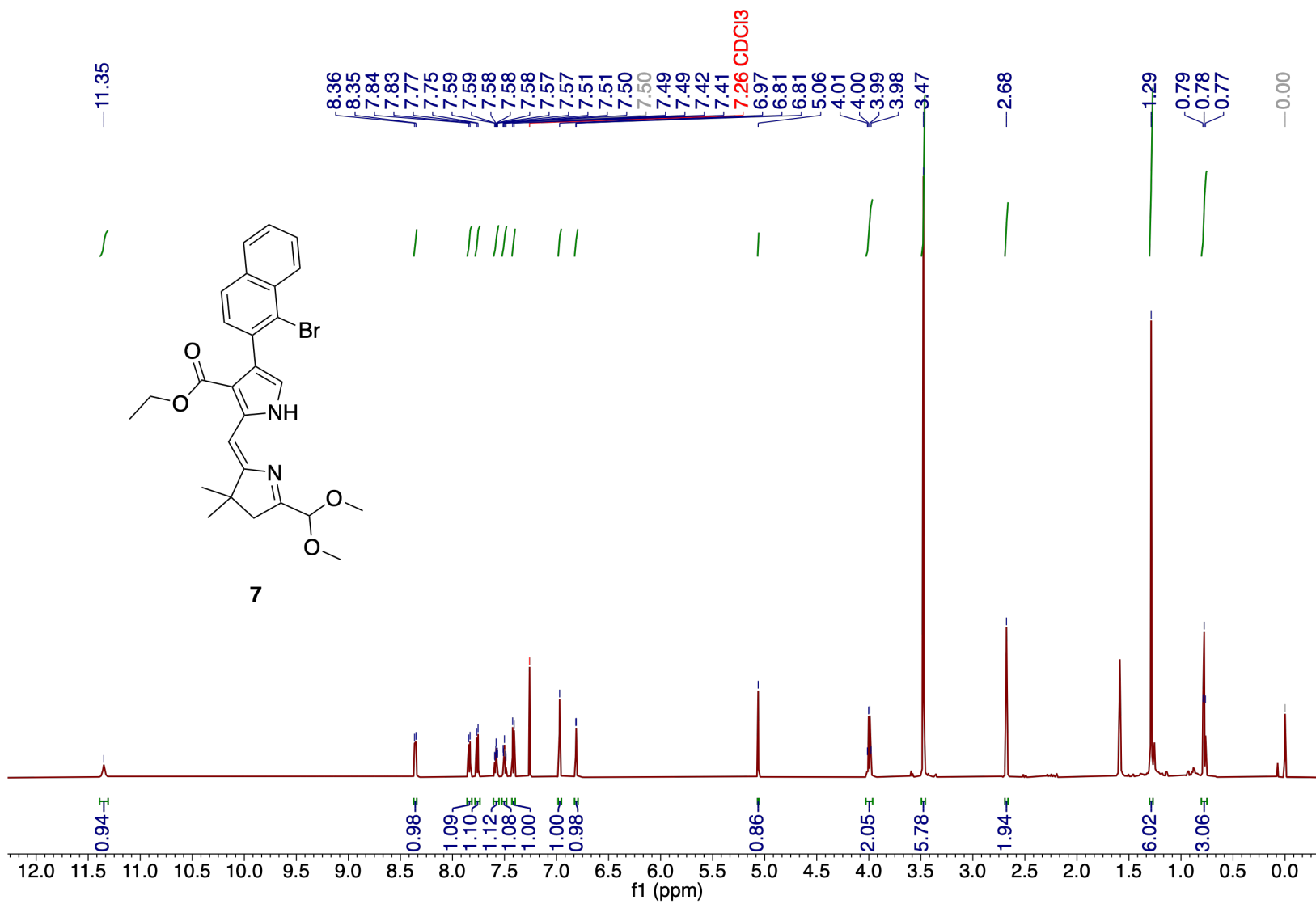
¹H NMR spectrum of compound 7
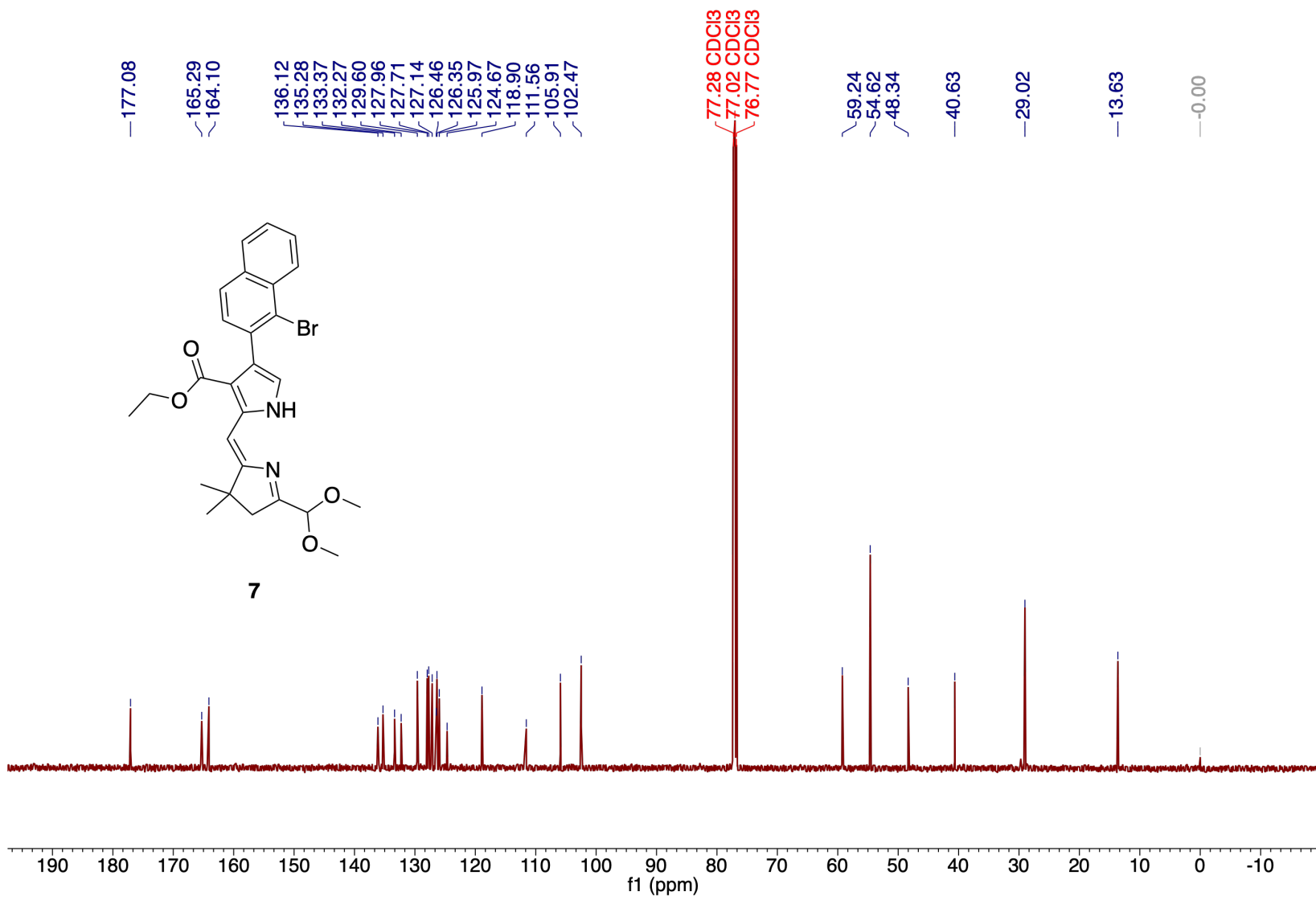
$^{13}C\{^1H\}$ NMR spectrum of compound 7
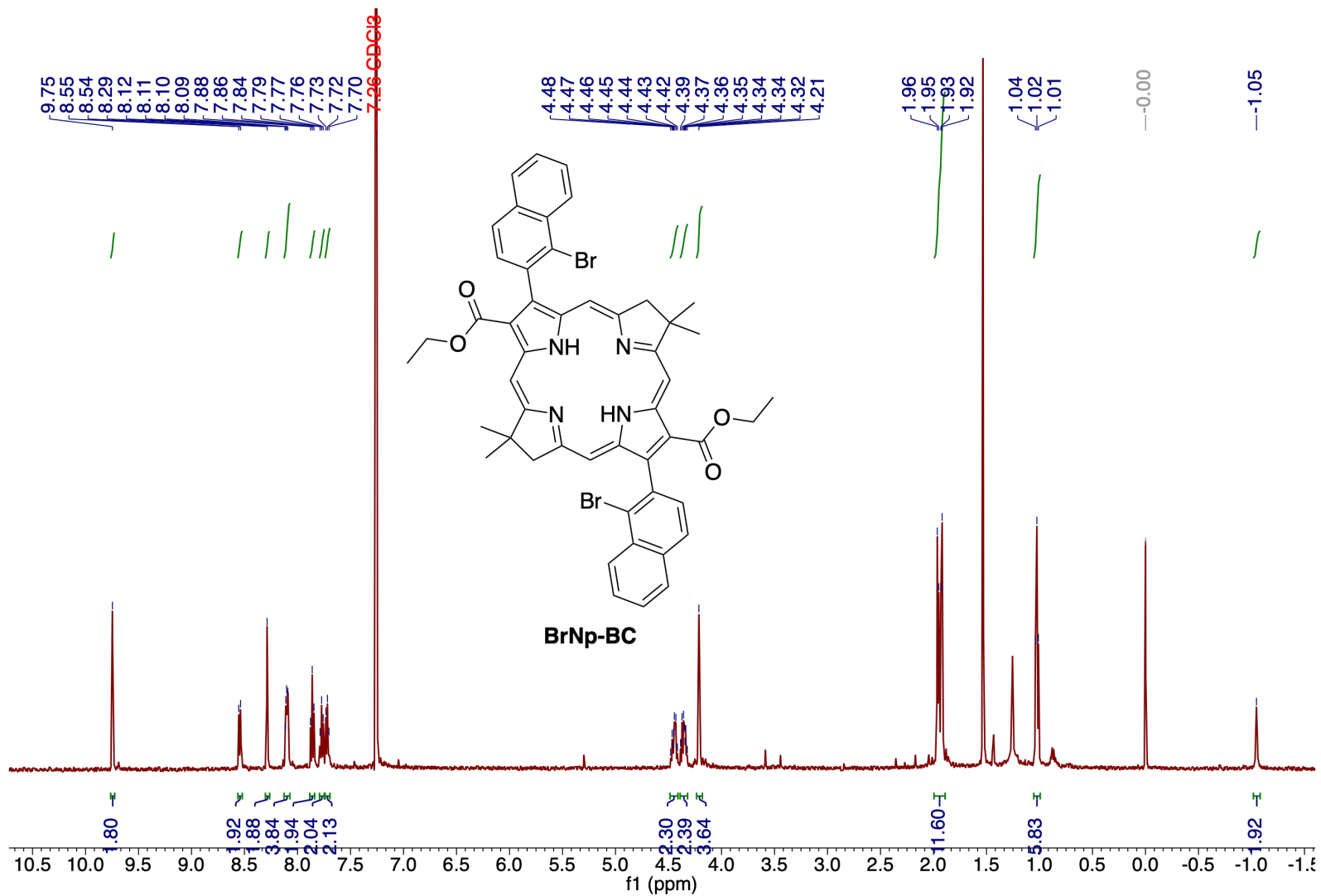
^{1}H NMR spectrum of BrNp-BC

^{13}C{^{1}H} NMR spectrum of compound BrNp-BC
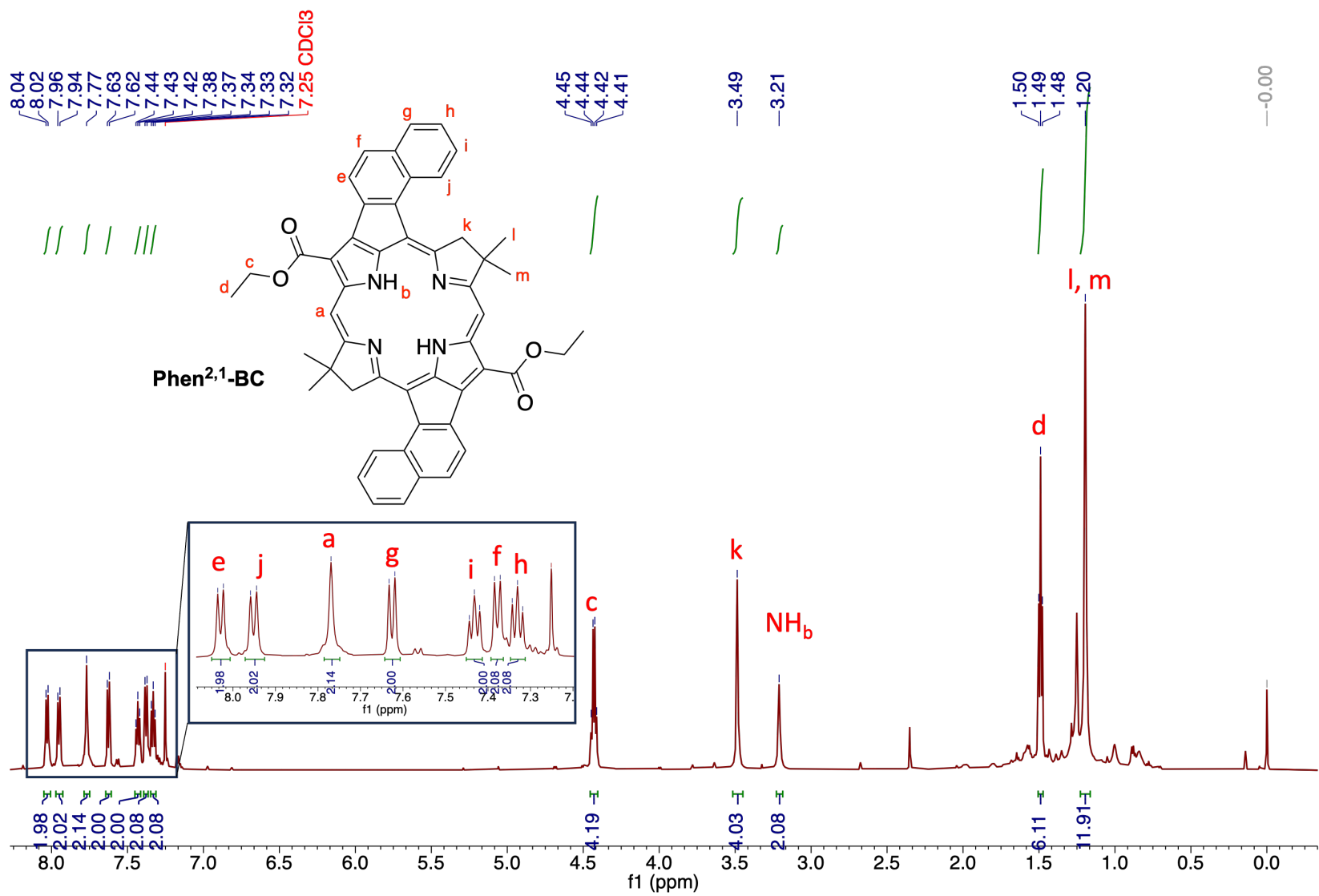
^{1}H NMR spectrum of Phen^{2,1}-BC
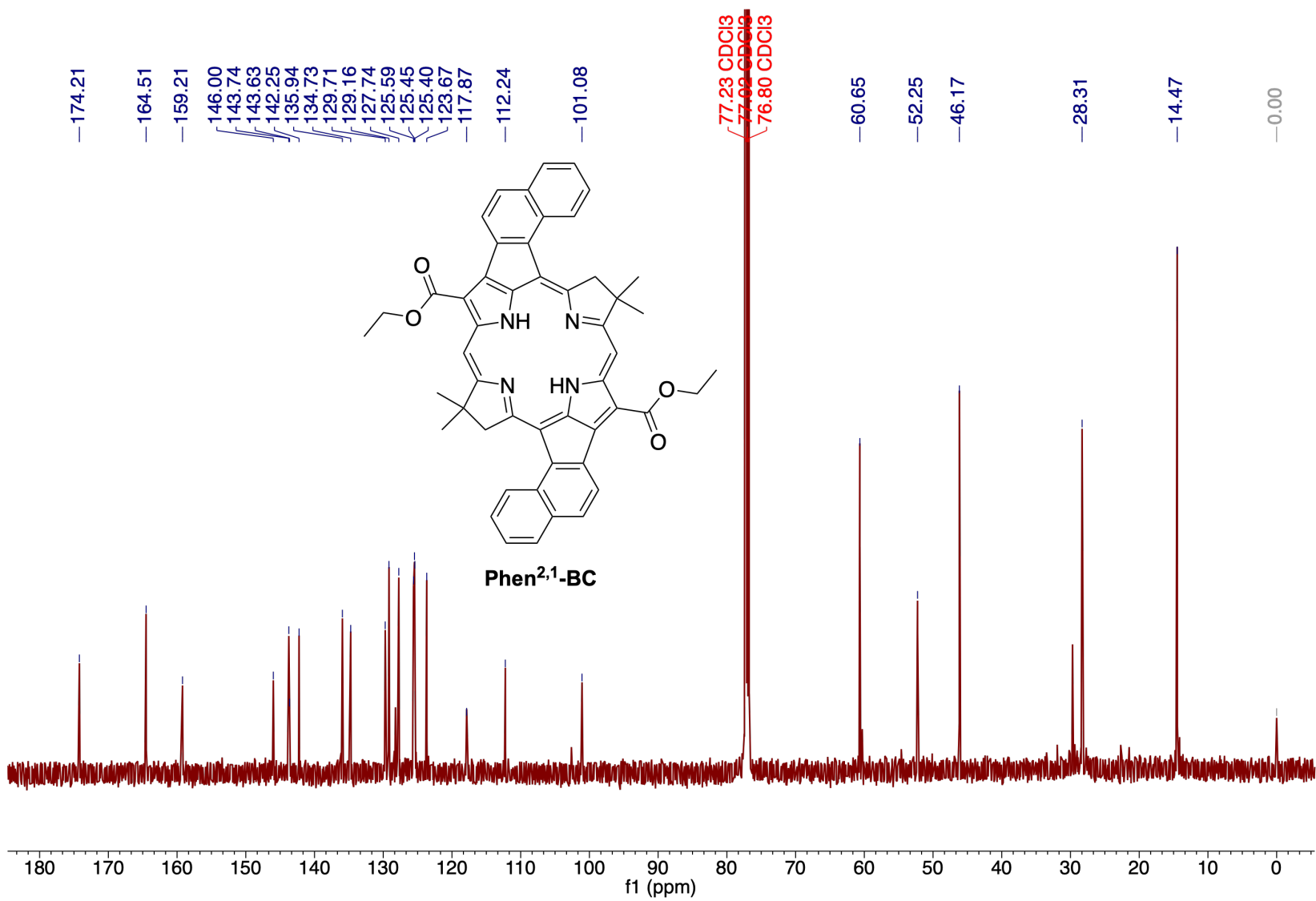
$^{13}C\{^{1}H\}$ NMR spectrum of Phen^{2,1}-BC

^{1}H NMR spectrum of compound S4

164.57
141.50
124.66
114.33
98.31
77.23 CDCl3
77.02 CDCl3
76.81 CDCl3
59.77
18.08
15.24
14.37
13.02
0.00

S4
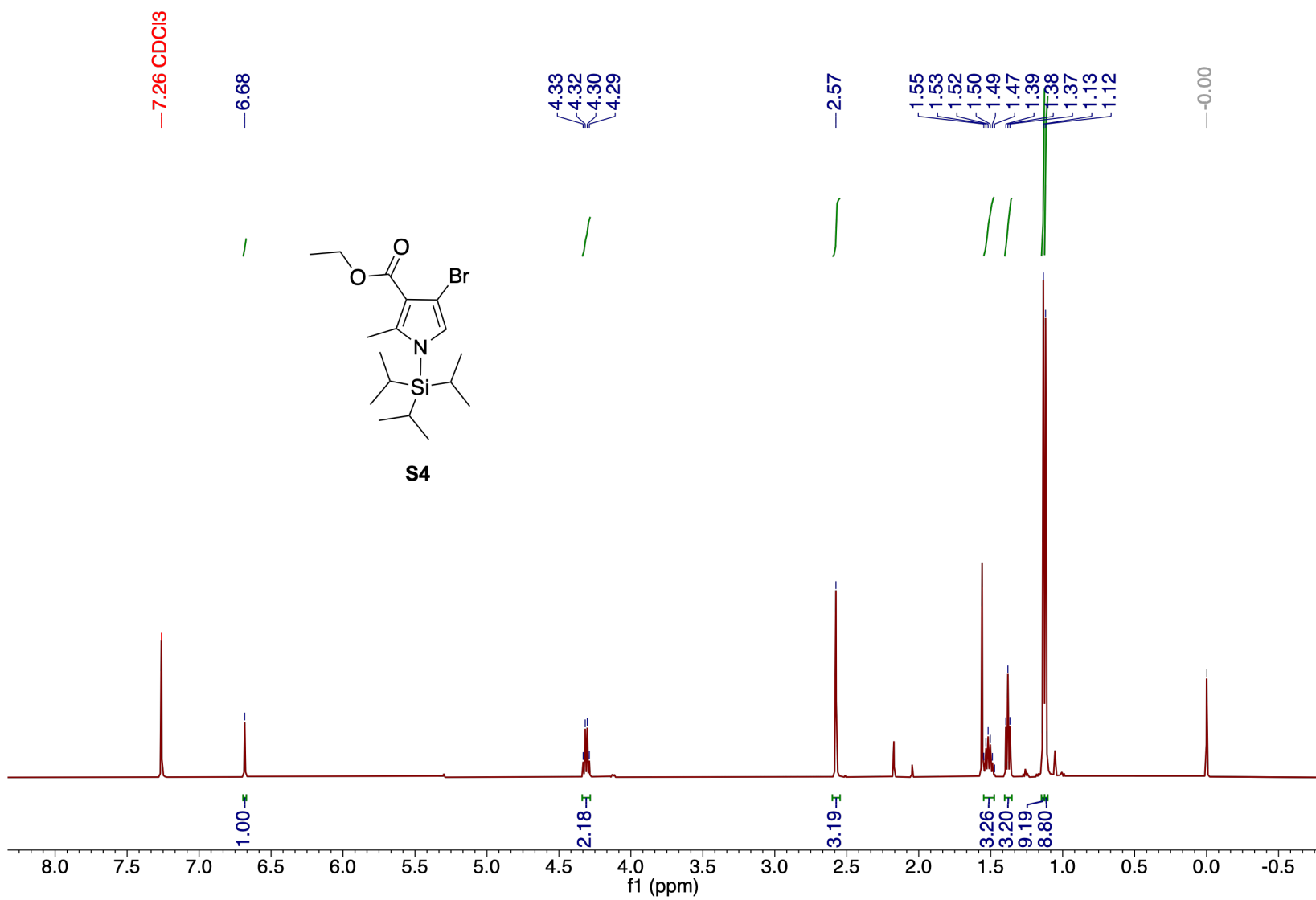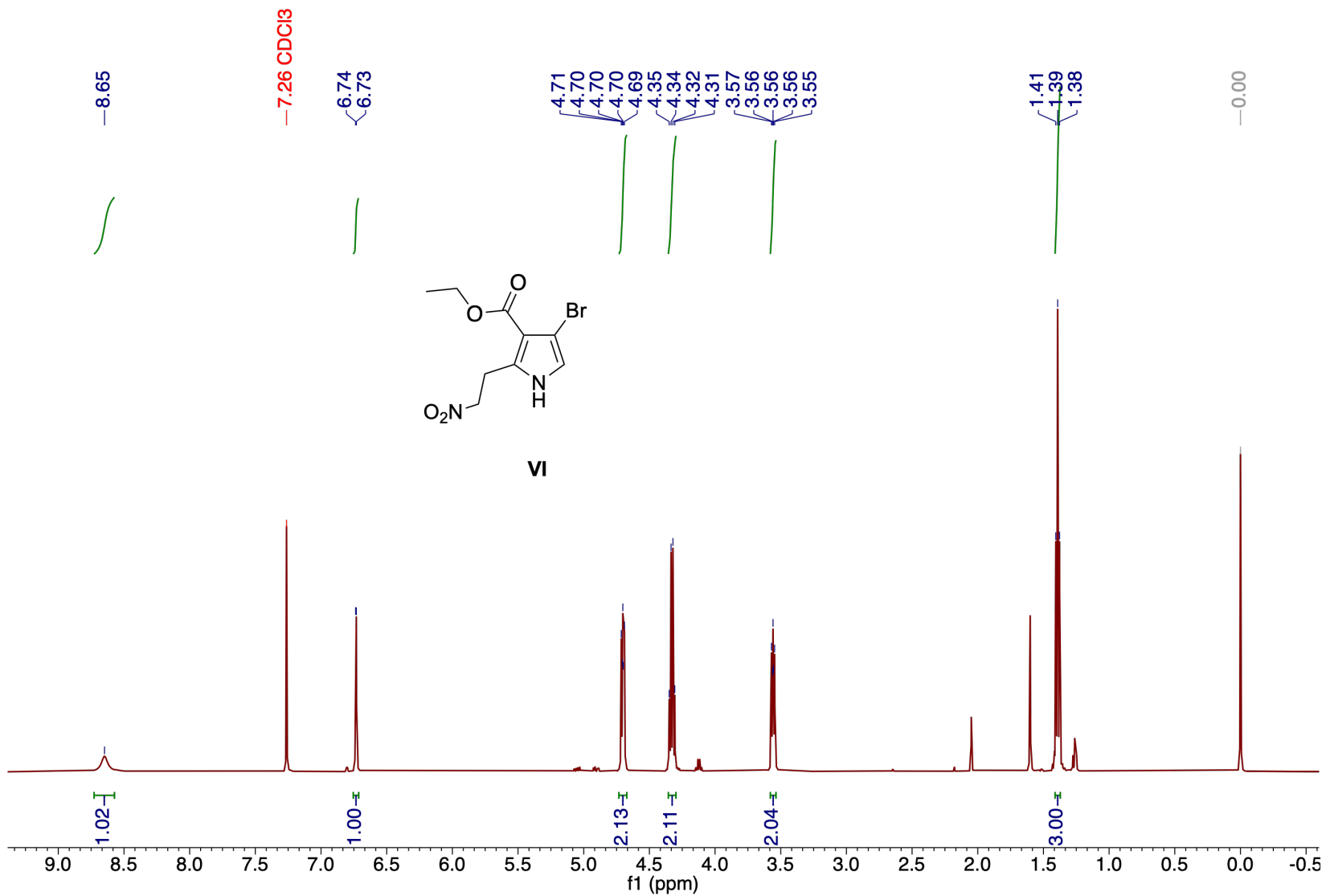
$^{13}C\{^{1}H\}$ NMR spectrum of compound S4

^{1}H NMR spectrum of compound S5
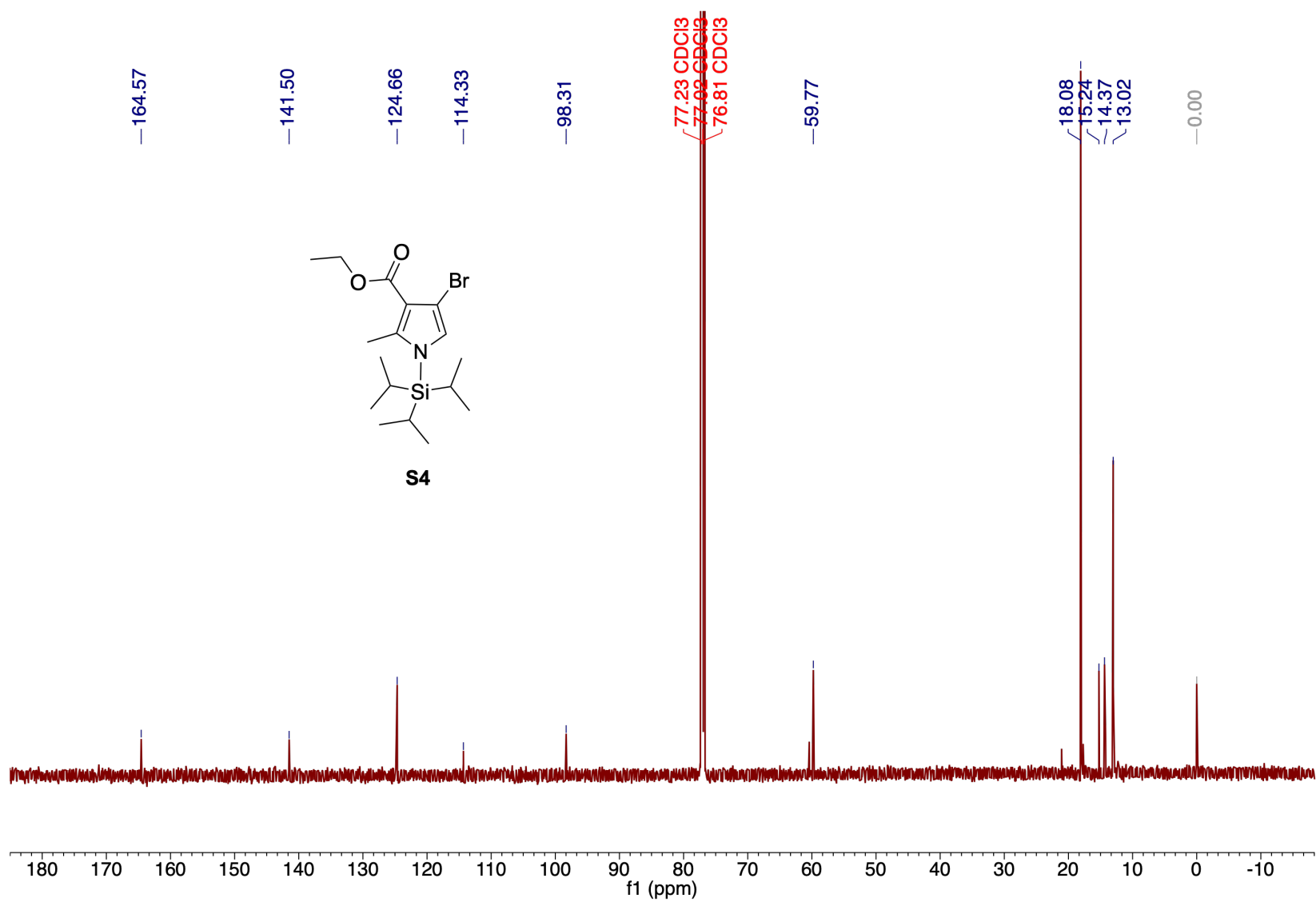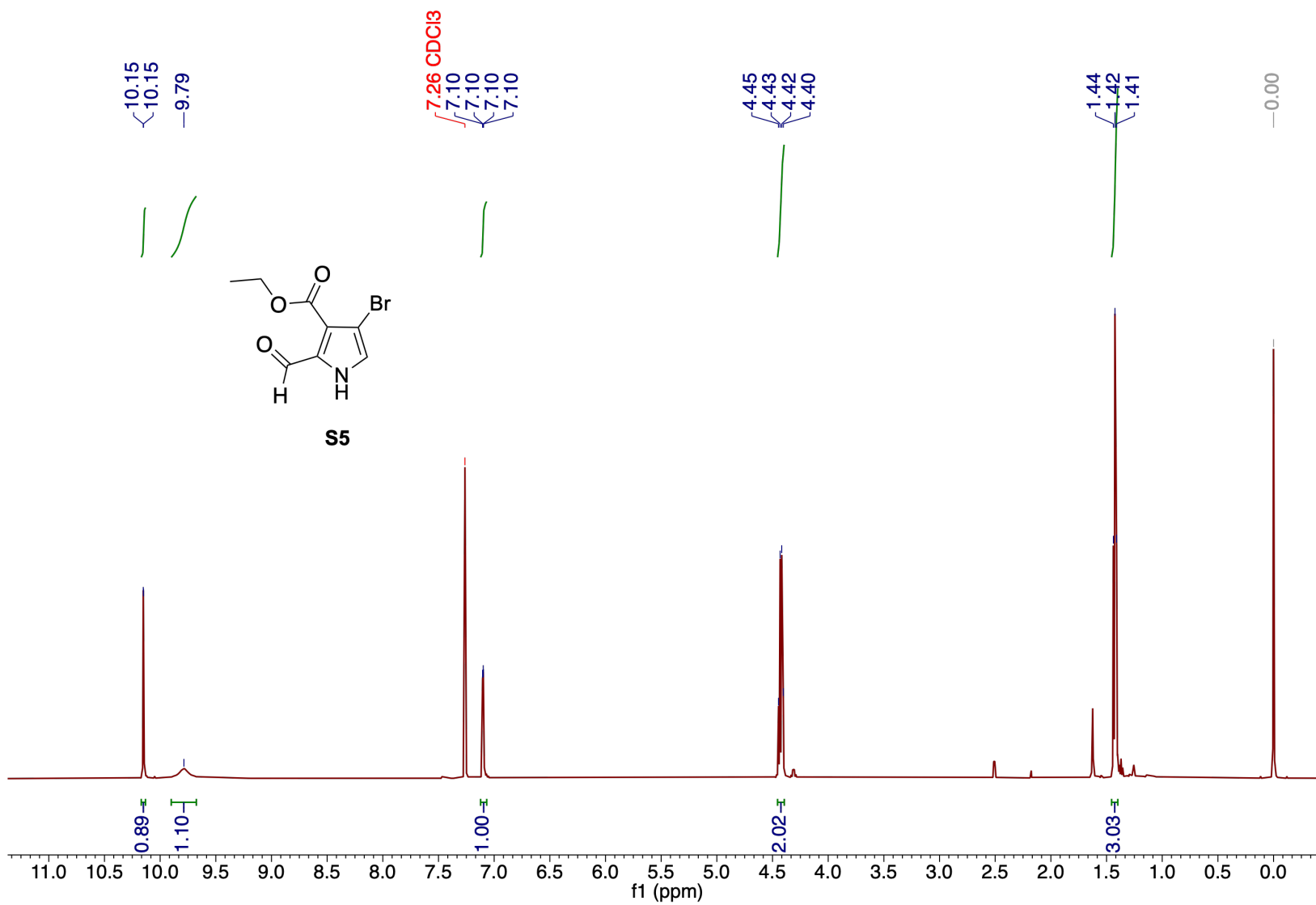
^{13}C{^{1}H} NMR spectrum of compound S5
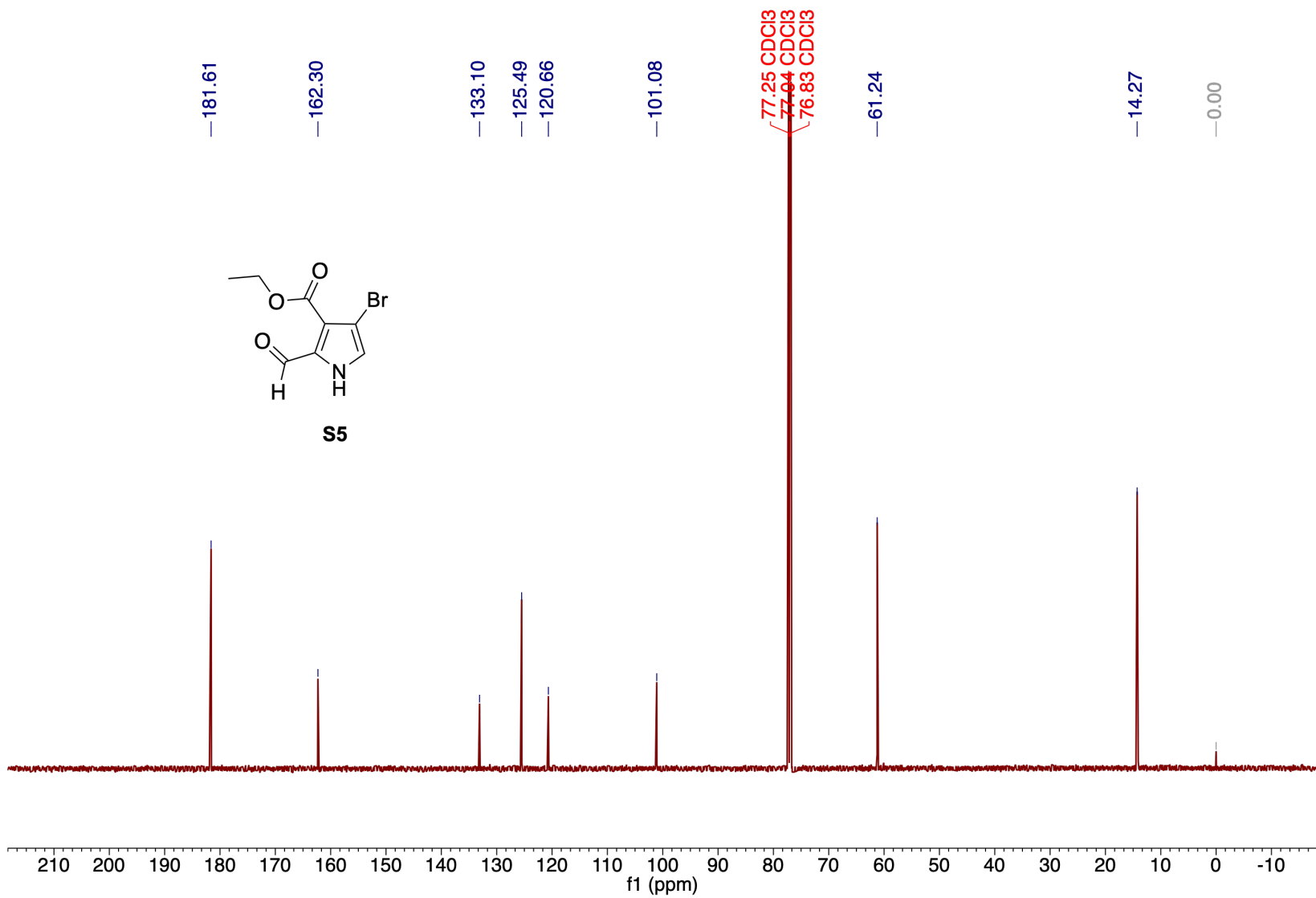
^{1}H NMR spectrum of compound VI

^{13}C{^{1}H} NMR spectrum of compound VI
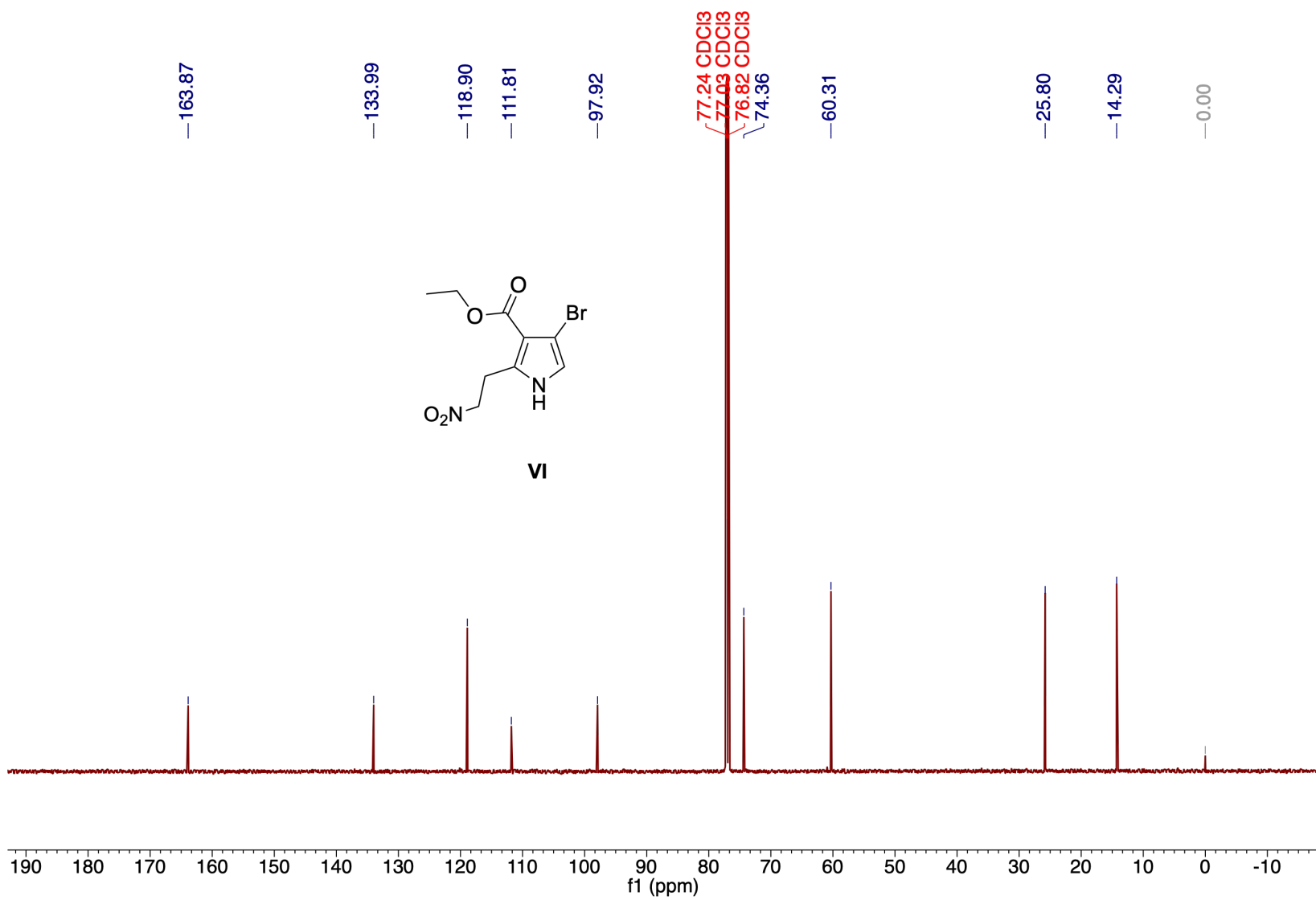
Dibrominated derivative of VI
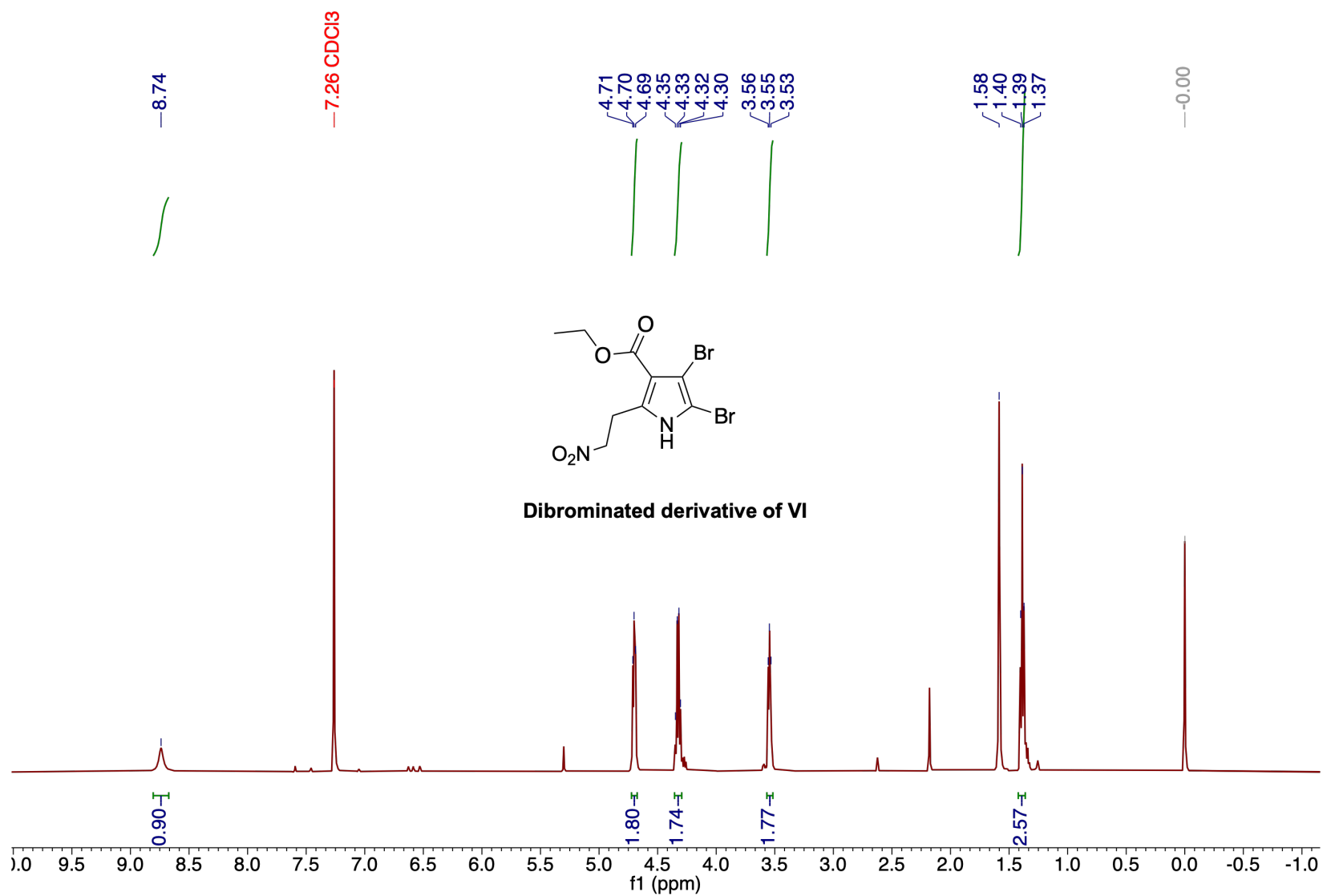
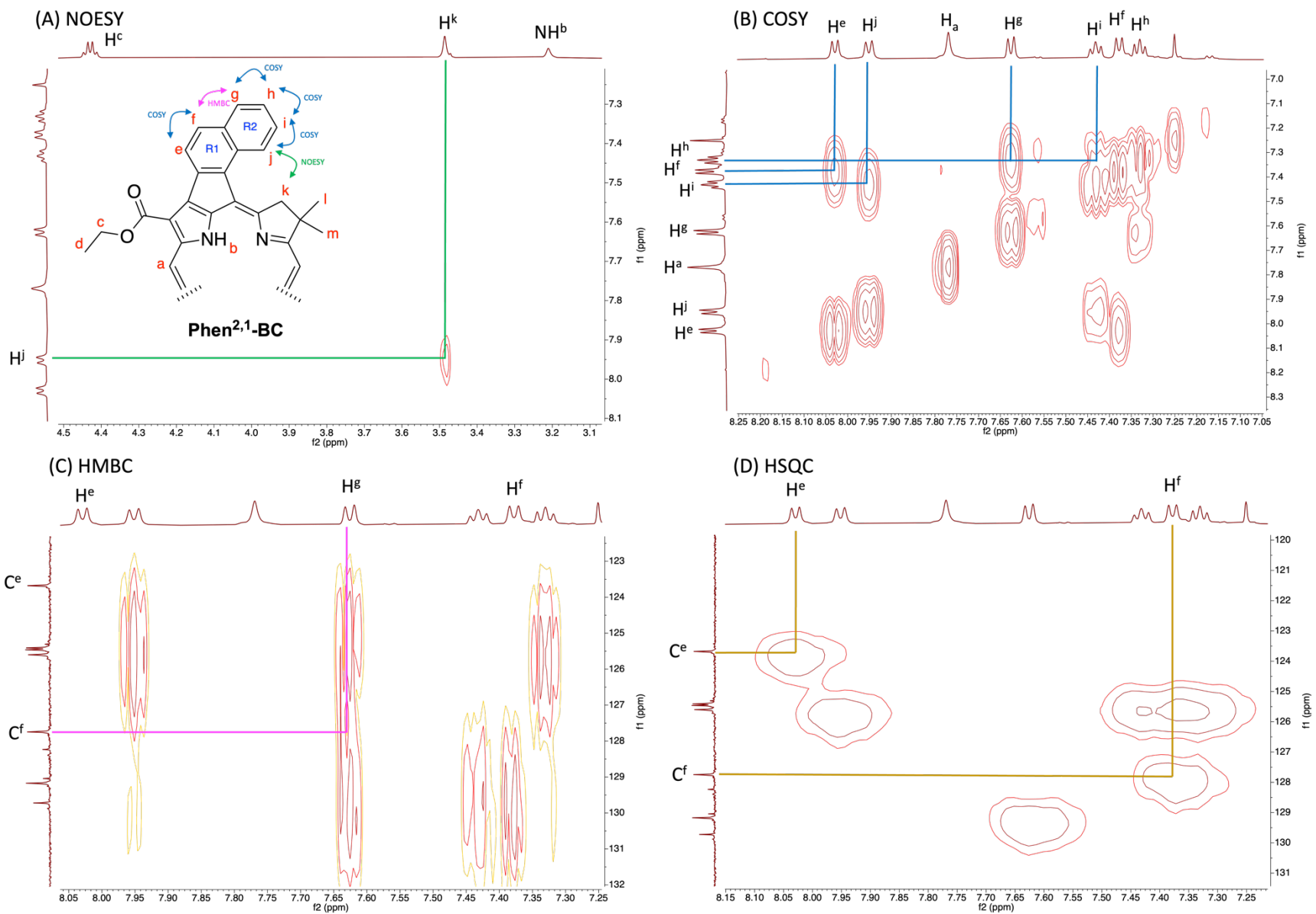^{1}H NMR spectrum of dibrominated derivative of VI

Figure S22. – see next page for figure legend and text.

Figure S22. See previous page for spectra. 2D NMR correlations of selected ^{1}H and ^{13}C signals supporting assignment of the aromatic proton resonances of annulated bacteriochlorin **Phen^{2,1}-BC**. (A) NOESY spectrum, (B) COSY spectrum, (C) HMBC spectrum, and (D) HSQC spectrum.

The structural integrity of **Phen^{2,1}-BC** was examined using two-dimensional NMR spectroscopy. The assignment of protons on the core bacteriochlorin and peripheral groups was straightforward based upon their splitting patterns and the number of protons, which are provided in Section 11. The following analyses provide the assignment of protons on the naphthalene moiety.

- The determination of H^j was probed by the only one weak correlation of the pyrroline protons against the protons in the aromatic region, in NOESY spectroscopy, suggesting the interaction through space between H^k and H^j (panel A).

- The assignment of H^i, H^h, and H^g atoms in ring R2 was subsequently achieved by the COSY resonances between H^j and H^i, H^i and H^h, and H^h and H^g (panel B).

- The assignment of H^e and H^f could not be easily achieved by using COSY spectroscopy, but their COSY interaction does ensure their presence in ring R1. To determine the chemical shifts of H^e and H^f, HSQC spectroscopy was used to preassign the corresponding carbons, C^e and C^f. Consequently, the C^f position was noted by HMBC correlation with the H^g atom. Moreover, the lack of correlation between C^e and H^g assures that C^f is the closest atom to H^g (panel C).

- Hence, the location of H^f was assigned by the correlation with the C^f atom using the HSQC spectrum (panel D). Subsequently, the H^e signal was assigned as the lone remaining signal in the aromatic region.